Two-Photon Quantum Interference using a Single Nitrogen-Vacancy Center

Annick Teepe

Responsible supervisor : Prof. dr. ir. Ronald Hanson
Daily supervisor : Ir. Kian van der Enden

A thesis presented for the degree of
Master of Science at the Delft University of Technology
Applied Physics
Hanson Lab, QuTech
June 18, 2021

Abstract

Generation of high fidelity entanglement between quantum nodes is a key component of a future quantum internet. Heralded entanglement generation of two spatially separated qubit nodes can be established by interference and measurement of two photons, each entangled with one qubit state. The two-node entanglement fidelity is limited by the degree of indistinguishability of the photons, which can be measured in a Two-Photon Quantum Interference (TPQI) experiment. In this thesis, a TPQI experiment has been performed with photons emitted by a single Nitrogen-Vacancy (NV) center. This self-interference experiment shows a visibility of $V = 0.91 \pm 0.02$ and a photon indistinguishability of $J = 0.945$ in the Monte-Carlo method obtained 1σ-confidence interval of [0.920, 0.966] after correction for system imperfections, demonstrating near-perfect indistinguishability of zero-phonon line photons emitted by a single NV center. Furthermore, an extensive TPQI model was developed that includes possible arrival time- and frequency differences of the photons. This model predicts a dark- and noise count limited $V = 0.79 \pm 0.06$ for a future two-node NV TPQI experiment with quantum frequency-converted photons, at a distinguishable photon coincidence rate of 1.2 mHz, allowing for an experimentally feasible double-click two-node entanglement fidelity of 0.89 ± 0.03.

Contents

1 Introduction **1**

2 Theory Nitrogen-Vacancy Centers **3**
2.1 Nitrogen-Vacancy Centers in Diamond . . . 3
2.1.1 Diamond Crystal Structure . . . 3
2.1.2 Electronic Level Structure . . . 4
2.1.3 Control . . . 5
2.2 Entanglement Generation . . . 6
2.2.1 Spin-Photon Entanglement . . . 6
2.2.2 Spin-Spin Entanglement . . . 7
2.3 Frequency Conversion . . . 10

3 Theory Two-Photon Quantum Interference **11**
3.1 Derivation Coincidence Probability . . . 11
3.1.1 Beamsplitters . . . 11
3.1.2 Joint Detection Probability . . . 13
3.1.3 Photon Wave Function . . . 13
3.1.4 Coincidence Probability . . . 14
3.2 Single NV TPQI . . . 18
3.2.1 Photon Indistinguishability . . . 18
3.2.2 Photon Counting Argument . . . 18
3.2.3 Dark- or Noise Counts . . . 19
3.2.4 Introducing Imperfections . . . 20
3.2.5 Error Calculation . . . 23

4 Experimental Set-Up **24**
4.1 Sample Fabrication . . . 24
4.2 Node 1 . . . 25
4.2.1 Optical Addressing . . . 25
4.2.2 Collecting NV Emission . . . 25
4.3 Single NV TPQI . . . 28
4.3.1 Set-Up . . . 28
4.3.2 Measurement Sequence . . . 28

5 Results and Discussion **30**
5.1 NV Calibrations . . . 30
5.1.1 CR Checks . . . 30
5.1.2 Single-shot Read Out . . . 30
5.1.3 Optical Pi Pulse Calibration . . . 31
5.2 Single NV TPQI experiment . . . 33
5.2.1 CR Checks during Experiment . . . 33
5.2.2 Laser Power Calibration during Experiment . . . 34
5.2.3 ZPL Single-Photon Detections . . . 35
5.2.4 Correction Factors . . . 36
5.2.5 Photon Indistinguishability . . . 40

5.3 Single NV TPQI model . . . 42
5.3.1 Model with Occurrence Probabilities . . . 42
5.3.2 Comparison Model and Data . . . 44
5.4 Two NV TPQI model . . . 47

6 Conclusions and Outlook **50**
6.1 Conclusions . . . 50
6.2 Outlook . . . 51

A Appendix Theory **52**
A.1 Joint Detection Probability . . . 52
A.2 No Constraint on Photon Detection Times . . . 52

B Appendix Results **55**
B.1 Selecting Signal Windows . . . 55
B.2 Coincidence Events due to Dark Counts . . . 55
B.3 Coincidence Counts in Time-Bins . . . 56
B.4 TPQI Model Verification . . . 56
B.5 Two NV TPQI Model . . . 57

Chapter 1

Introduction

Richard Feynman once said, "I think I can safely say that nobody understands quantum mechanics." (1965). It can be argued that this powerful statement has remained true over the entire century that the theory of quantum mechanics (QM) exists. Even though the debate of how to *interpret* this theory is still ongoing, QM is widely regarded as one of the most successful and accurate theories in physics: no experiment to date has ever contradicted its predicted outcomes. One of its outcomes is the property of quantum entanglement between two quantum systems.

A qubit is an example of a quantum system. It is a fundamental unit of information that is radically different than its classical analogue, the bit. Whereas a bit can take on either the value 0 or 1, a qubit can be in a so-called superposition of both states: it is in the state *0* and *1* at the same time. A measurement of the state of the qubit will however result in a single binary outcome: its state, or wavefunction, is said to collapse instantaneously onto either *0* or *1*, according to the Copenhagen interpretation [1]. A measurement therefore destroys the superposition, a property which forbids the possibility to either copy or amplify a quantum state, known as the no-cloning theorem.

Entanglement between qubits leads to correlations over large distances that are stronger than classically possible. If two qubits A and B are entangled, their state is non-separable. An example of such an entangled state is $(|0\rangle_A|0\rangle_B + |1\rangle_A|1\rangle_B)/\sqrt{2}$. If a measurement is performed on qubit A yielding the outcome, or observable, *1*, which corresponds to the state $|1\rangle_A$, then a subsequent measurement on qubit B will yield the outcome *1* as well, corresponding to the state $|1\rangle_B$, with *unit* probability. Even if the two qubits are spatially separated over a long distance, this argument holds. Not only is the property of entanglement a fascinating phenomena that is interesting enough to study in it itself, it can also be used for practical implementations: it is a key component of a quantum network.

Spatially separated stationary qubits can become the nodes of a quantum network. Entanglement generation between these nodes is mediated by photons, single light particles, which can travel over the optical fibers connecting the nodes. Photons are a form of qubits and are often named flying qubits owing to their mobile nature. This network of interconnected nodes can form the quantum internet, a fundamentally new internet technology that will enable quantum communication by transmitting qubits. The combination of the no-cloning theorem and the property of quantum entanglement ensures inherently safe quantum communication via this network. The quantum internet will allow for applications impossible with the classical internet, such as quantum key distribution, secure identification, clock synchronization and communication between quantum computers for distributed computing [2]. Even though the quantum internet is still in its early stages of development, rapid experimental progress has shown promising results. Entanglement between two nodes separated by 1.3 km has already been demonstrated [3].

One of next challenges in the building of a quantum network is to generate heralded entanglement between two network nodes separated by metropolitan distance. The QLink Demonstrator project aims to generate entanglement between a node situated in Delft and a node situated in Den Haag, mediated by a midpoint station in Rijswijk. The Nitrogen Vacancy (NV) center in diamond is a promising candidate for such a stationary network node as it allows for the generation of single photons entangled with its own qubit state. Other advantages are the long coherence times and the bright optical transitions enabling high-fidelity measurement and control of this solid state qubit [4]. Entanglement between two

NV centers is established by interference and measurement of two photons, each emitted by and entangled with the NV electronic spin of the particular node. This interference takes place at a beamsplitter situated in between the two nodes (at the midpoint station in Rijswijk), requiring each photon to travel the distance from their correlated node to the beamsplitter. The main limitation of the entanglement generation of NV centers over large distances are the high photon losses in the optical fibers, in the order of 8 dB km^{-1} for the natural emission frequency of NV centers [5]. The transmission of photons can be improved by down-converting the frequency of the photons to the telecom wavelength (1588 nm) using a Quantum Frequency Converter. The fiber losses of photons at this wavelength is much less, in the order of 0.2 dB km^{-1} [6].

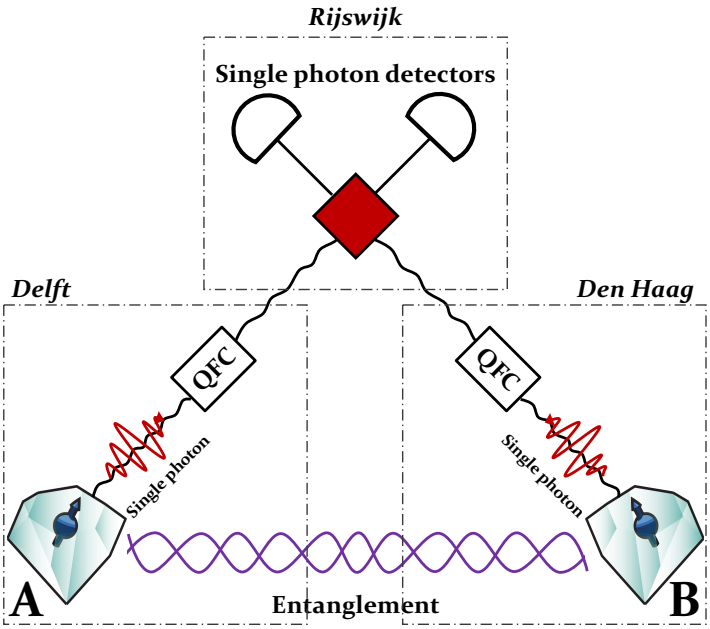

Figure 1.1: Schematic representation of a future set-up to generate remote entanglement between two NV centers A and B, located in Delft and in Den Haag, mediated by interference and detection at a midpoint station in Rijswijk. To reduce photonic loss, photons are converted to the telecom wavelength using Quantum Frequency Converters.

A schematic representation of the future set-up to generate entanglement over metropolitan distances is given in Fig. 1.1.

Next to the requirement of bridging the distance, the two photons are also required to be indistinguishable in all of their properties, being their frequency, their location in space-time, and their polarisation. If the photons are slightly distinguishable, then this directly decreases the fidelity of the entangled state. Therefore, the degree of indistinguishability of photons is an important property, which can be measured in a Two-Photon Quantum Interference (TPQI) experiment.

In the duration of this thesis project, only one of the two existing nodes was available, so a two-node TPQI experiment was not feasible. Therefore, a self-interference experiment of single photons emitted by one NV center will be performed, which serves as a stepping stone towards two-node TPQI experiments. The indistinguishability of the photons emitted by a single NV center will be determined. Additionally, a theoretical model of TPQI will be developed and applied on the self-interference experiment of one NV center, and also used for predictions of a future two-node TPQI experiment. In **Chapter 2**, a description of the physics of NV centers is given. In **Chapter 3**, the theory of TPQI is described, including the derivation of the model. In **Chapter 4**, a description of the experimental set-up is given. In **Chapter 5**, the results of the single NV TPQI experiments are presented, as well as a comparison with the TPQI model. Also, the predictions of a two-node experiment based on the model are presented here. Concluding remarks and an outlook can be found in **Chapter 6**.

Chapter 2

Theory Nitrogen-Vacancy Centers

In this chapter, the properties of the Nitrogen-Vacancy center are described, as well as the mechanisms that enable qubit state control in experiments. Next, a section follows on generating entanglement between the qubit state and a photonic state, followed by an explanation of two entanglement protocols of two Nitrogen-Vacancy centers. In addition, a short section is presented concerning the conversion of the photon frequency which will allow for longer transmitting distances of photons.

2.1 Nitrogen-Vacancy Centers in Diamond

2.1.1 Diamond Crystal Structure

The diamond crystal structure is a face-centered cubic Bravais lattice with two atoms in the basis, of which the first atom is at the position of a lattice point, while the second is shifted by $\frac{1}{4}$ along each axis. Each carbon atom forms covalent bonds with four nearest neighbour carbon atoms, at equal distances [7]. Nitrogen-vacancy (NV) centers are point defects in the carbon lattice of diamond, where a carbon atom is replaced by a nitrogen atom and at an adjacent lattice site a carbon atom is missing, resulting in a vacancy. The main axis of an NV center is defined as the vector from the vacancy to the nitrogen atom. It can have four possible orientations with respect to the crystallographic axes [8]. The carbon atoms in pure diamond have enclosed angles of 109.47°. Therefore, the four possible NV orientations are separated with this angle as well. See also Fig. 2.1.

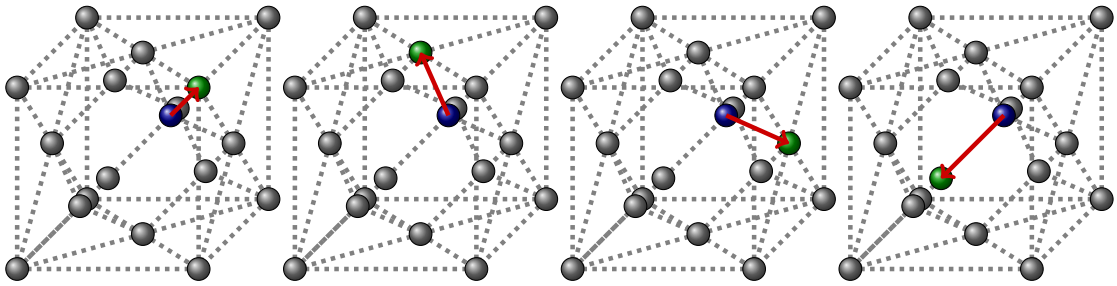

(a) [111] orientation **(b)** [$\bar{1}\bar{1}1$] orientation **(c)** [$\bar{1}1\bar{1}$] orientation **(d)** [$1\bar{1}\bar{1}$] orientation

Figure 2.1: The four possible orientations of a NV center in the diamond lattice. The carbon atoms are in grey, the vacancy is in blue and the nitrogen atom is in green. The origin of the coordinate system is at the location of the vacancy. The main axis of the NV is depicted by the red arrow.

For the application of single NV centers as potential nodes in a quantum network, it is preferable that the NV's main axis has an orientation parallel to surface normal of the sample, as both the photon collection efficiency and the optical addressing are optimal for an NV with this orientation [9]. For diamond samples with a surface along the (111) crystalline orientation, this would correspond to the [111] orientation shown in Fig. 2.1a.

2.1.2 Electronic Level Structure

In the NV center, three of the five valence electrons from the nitrogen atom covalently bond to neighbouring carbon atoms, while two of them remain unbonded. The neighbouring carbon atoms of the vacancy each have three unpaired electrons. In total, the neutrally charged NV center is accompanied by five electrons: two from the nitrogen atom and one from each of the three neighbouring carbon atoms. At the vacant spot of the NV center, an electron can be captured from the environment, resulting in a negatively charged NV center, NV^- [4]. In the remainder of this document, this particular charge state will be referred to as NV. The extra electron forms a spin-1 pair with one of the vacancy electrons, forming a triplet state. The electronic structure of the NV center is characterised by meta-stable singlet

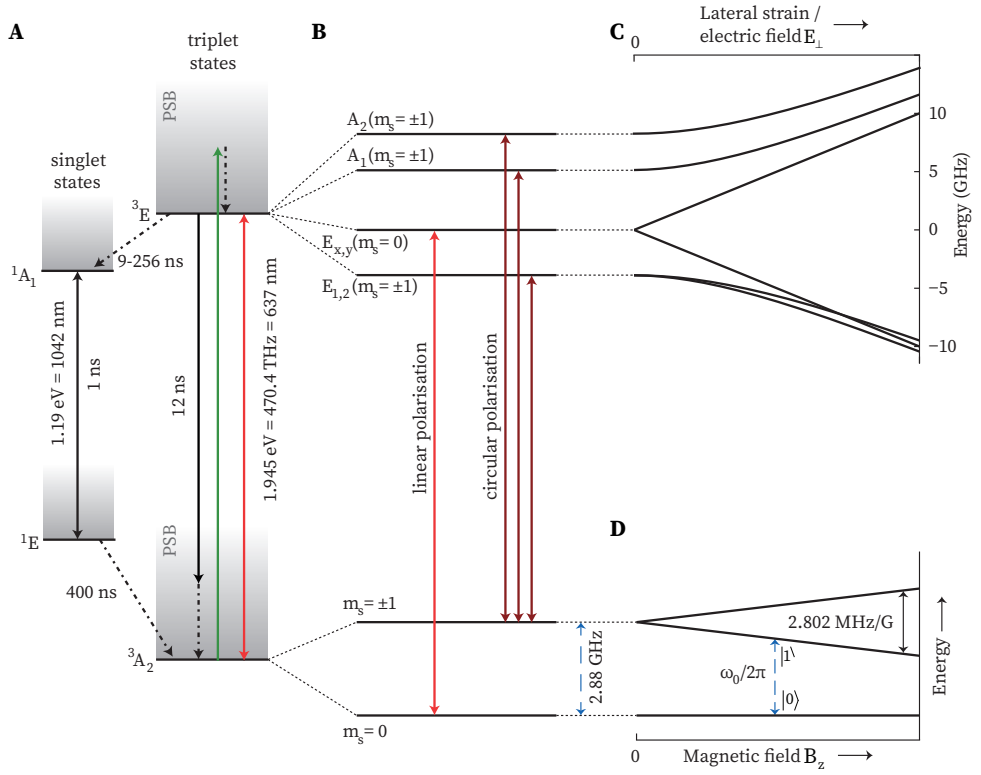

Figure 2.2: Electronic level structure of the negatively charged NV center, image taken from Faes[10]. **A)** Resonant (ZPL, bright red arrow) and off-resonant (PSB, green and black arrow) excitation and emission between the spin triplet ground state $^3A_2$ and excited state ^3E. The excited state can also decay via the singlet states, with the emission of photons with frequencies far from the excitation frequency. **B)** The splitting of energy levels at cryogenic temperatures, with no applied magnetic field. The $m_s = 0$ and $m_s = \pm 1$ states can be excited separately, represented by the bright red and dark red arrows, respectively. **C)** Lateral strain or an electric field splits the energy levels of the excited triplet state due to the DC Stark effect **D)** A magnetic field applied along the NV main axis lifts the degeneracy of the $m_s = \pm 1$ states due to the Zeeman effect, allowing for the definition of a qubit, $|0\rangle$ / $|1\rangle$, within the ground state triplet.

spin states and triplet spin states, of which the latter have the lowest ground state energy, see Fig. 2.2A. In the triplet ground state, the $m_s = 0$ and $m_s = \pm 1$ states are separated by the zero-field splitting of approximately 2.88 GHz mainly due to spin-spin interactions, while the $m_s = \pm 1$ states are degenerate in energy. An external magnetic field parallel to the NV main axis lifts this degeneracy due to the Zeeman effect (Fig. 2.2D) according to $\Delta\omega = 2.802 B_z$, with the level splitting $\Delta\omega$ in MHz and B_z in Gauss [1]. The $m_s = 0$ and one of the $m_s = \pm 1$ states together form a two level system which can be utilized as a qubit [4]. To this end, we define $|0\rangle$ as the $m_s = 0$ state and $|1\rangle$ as one of the $m_s = \pm 1$ states. The excited triplet energy levels can only be distinguished at cryogenic temperatures due to spin-spin and spin-orbit interactions [11]. When an electric field or lateral strain is present, the excited states shift in frequency, as is shown in Fig. 2.2C, due to the Stark effect. The $E_{x,y}$ states become degenerate in energy. The ground states experience only a weak shift with strain or an electric field [4].

The triplet ground states can be excited either resonantly or off-resonantly. Off-resonant excitation of one of the triplet ground states occurs to an energy level higher than the corresponding excited state. In this way, a phonon level above the excited state will become populated, indicated by the green arrow in Fig 2.2A. Non-radiative quick decay upon emission of a phonon brings the state back to the excited state [11].

The $m_s = 0$ state is degenerate in energy from the $m_s = \pm 1$ states. Therefore, resonant excitation of the $m_s = 0$ state occurs at a different frequency than resonant excitation of the $m_s = \pm 1$ states. Resonant excitation of the $m_s = 0$ state is done by applying a linearly polarised laser pulse of 637 nm, being the readout (RO) laser. The corresponding excited state is one of the $E_{x/y}$ states. This transition is depicted by the bright red arrow in Fig 2.2B. The $m_s = \pm 1$ states can be optically excited resonantly to one of the $E_{1/2}/A_{1/2}$ excited states by applying a circularly polarised laser pulse, being the spinpump (SP) laser. These transitions are indicated by the dark red arrows in Fig 2.2B.

After either resonant or off-resonant excitation has taken place, the excited triplet states are populated. Decay from the excited triplets to the ground state triplets can occur in three different ways. The first relaxation possibility is an indirect decay involving the emission of a photon to an energy level higher than the ground state, followed by the emission of a phonon, indicated by the black arrow in Fig. 2.2A. This emitted photon will have a wavelength of $\lambda > 637$ nm, and will enter the so-called phonon side band (PSB). The second possibility is decay via the meta stable singlet states to the triplet ground state, involving the emission of a photon far from the resonant excitation frequency, shown on the left side of Fig. 2.2A. Relaxation via the singlet states happens on much larger timescales. This transition is more likely to occur for the $m_s = \pm 1$ states than the $m_s = 0$ states. Therefore, the $m_s = \pm 1$ state is often named 'dark state', in contrast with the $m_s = 0$ state named 'bright state'[12]. The third possibility is direct relaxation from the excited state triplets to the ground state, under emission of a photon with a wavelength of $\lambda = 637$ nm. At the low temperature, low strain regime, the decay takes place in approximately 12 ns [13]. This transition is depicted by the bright red arrow in Fig 2.2A. As no phonons are involved in this relaxation process, the emitted photon will enter the so-called zero phonon line (ZPL). The photons emitted in the ZPL are indistinguishable in both frequency and polarisation [14], allowing them to be used for entanglement generation or for two-photon interference experiments. In Chapter 3 the importance of the indistinguishability of photons will be further elaborated. Unfortunately, the photon emission of NV centers in the ZPL upon resonant emission is small: it constitutes only 3% of the total emission [15].

To keep the probability of photon emissions in the ZPL as high as possible, the lasers used for excitation must be kept on resonance with the right transitions, and the NV center must remain in the NV^- charge state charge. So-called charge-resonance checks are done in-between experiments to make sure this is the case. This will be explained in more detail in the Chapters 4 and 5.

2.1.3 Control

The optical transitions described in the previous section allow for control of the qubit state of the NV center, being initialisation, readout and Bloch sphere rotations.

Initialisation

By cycling the spinpump transition, the qubit will be initialised in $m_s = 0$. Population from the $m_s = \pm 1$ state is excited to the $E_{1/2}/A_{1/2}$ states. Relaxation can happen either to the $m_s = 0$ ground state or to the $m_s = \pm 1$ ground states, where the spinpump laser will excite the state again. However, this laser is not resonant with the $m_s = 0$ transitions, so the system will be pumped into the dark state without being able to escape it. This process is indicated by the dark red lines in Fig. 2.3. The typical duration needed for initialisation is in the order of 2 µs.

Readout

The qubit state can be read out by cycling the readout transition. To this end, the readout laser is directed to the NV center for around 10 µs. If the qubit was initially in the $m_s = 0$ state, then excitation to the $E_{x/y}$

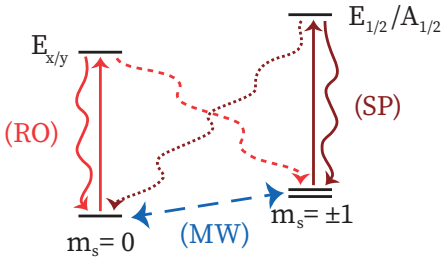

Figure 2.3: The initialisation, rotation and readout of the qubit makes use the transitions shown here. The dotted lines show lower probability processes. Image taken from Faes[10].

state occurs followed by relaxation via emission of a photon, into either the PSB (97 % of the time) or into the ZPL (3 %) of the time. This is depicted by the bright red lines in Fig. 2.3. If the qubit was initially in the $m_s = \pm 1$ state, then no excitation occurs and no photon will be emitted. Detection of a photon upon application of RO pulse therefore means that the qubit was in the state $m_s = 0$. Dark- and noise counts, which are false detection events or the detection of photons not emitted by the NV, respectively, directly limit the readout fidelity, as they might result in assigning the state $m_s = 0$ while the system actually was in $m_s = \pm 1$.

Bloch sphere rotations

By application of microwave (MW) pulses, the state of the qubit can be rotated over the Bloch sphere to a different spin state. A magnetic field oscillating at the Larmor frequency of the qubit, orthogonal to the NV main axis, will rotate the spin state. By changing the duration, power and shape of the pulse one can tune the amount of rotation of the spin state. A MW π-pulse is indicated by the blue dotted line in Fig. 2.3.

2.2 Entanglement Generation

The two spin states $m_s = 0$ and one of the $m_s = \pm 1$ form a two-level system which can be utilised as a qubit. In the following, the spin state $m_s = 0$ is written as $|\uparrow\rangle$ and one of the spin states $m_s = \pm 1$ is written as $|\downarrow\rangle$.

2.2.1 Spin-Photon Entanglement

When the NV center is in the $m_s = 0$ state, it can generate a photon upon resonant excitation in the ZPL. Therefore, the spin of the NV center can be entangled with a photonic quantum state written in the presence $|1\rangle$ and absence $|0\rangle$ encoding, which are two orthogonal states. The process to generate spin-photon entanglement using a presence-absence encoding is outlined below.

1. Initialise the NV center into the generalized superposition state $|\text{NV}\rangle = \sqrt{\alpha}\,|\uparrow\rangle + \sqrt{1-\alpha}\,|\downarrow\rangle$, where α denotes the bright-state population.

2. Selectively excite the $|\uparrow\rangle$ state by applying a short RO laser pulse, which rapidly decays again by emission of a photon. The $|\downarrow\rangle$ part of the state is not excited and will not emit a photon. In the presence- and absence encoding of the photon p, the resulting state is $|\text{NV}, p\rangle = \sqrt{\alpha}\,|\uparrow\rangle|1\rangle + \sqrt{1-\alpha}\,|\downarrow\rangle|0\rangle$. This state is non-separable, meaning entanglement of the NV center and the photon.

The method of the presence/absence encoding of the photonic state has as disadvantage that the loss of a photon completely rotates the photonic state. Next to entanglement between the spin of the NV center and a photonic quantum state in the presence and absence encoding, another method exists to entangle the NV spin with a photonic quantum state in a so-called time bin encoding. Here, detection of a photon in an early time window projects the photonic state to $|E\rangle$, early, and the detection of a photon in a later time window projects the photonic state to $|L\rangle$, late. The process to generate spin-photon entanglement using a time-bin encoding is outlined below.

1. Initialise the NV center into an equal superposition state $|\text{NV}\rangle = (|\uparrow\rangle + |\downarrow\rangle)/\sqrt{2}$
2. Selectively excite the $|\uparrow\rangle$ state by applying a short RO laser pulse, which rapidly decays again by emission of a photon in the early time bin. The $|\downarrow\rangle$ part of the state is not excited and will not emit a photon. The NV-photon state can be written as $(|\uparrow\rangle|E\rangle + |\downarrow\rangle|0\rangle)/\sqrt{2}$.
3. Flip the spin state of the NV center by applying a MW π-pulse, resulting in the state $(|\downarrow\rangle|E\rangle + |\uparrow\rangle|0\rangle)/\sqrt{2}$
4. Selectively excite the $|\uparrow\rangle$ state a second time by again applying a short RO laser pulse. The NV-photon state can then be written as $|\text{NV}, p\rangle = (|\downarrow\rangle|E\rangle + |\uparrow\rangle|L\rangle)/\sqrt{2}$. Detection of a photon in the early time bin will collapse the state of the NV to $|\downarrow\rangle$. Detection of a photon in the late time bin will collapse the sate of the NV to $|\uparrow\rangle$.

Spin-photon correlations give the quality of entanglement between the electron spin and photon. Due to dark- or noise counts, or the loss of photons, this quality deteriorates [16]. Using the method of entanglement between the spin state and a photonic quantum state in the time-bin encoding, near-perfect correlations have already been measured, even for frequency converted photons [17]. This method, however, has as disadvantage that two optical excitations are required, as well as a period of waiting time between them, meaning a lower rate as compared to the method using the presence/absence encoding.

2.2.2 Spin-Spin Entanglement

When two NV centers are both entangled with a photonic quantum state, interference of the two photons on a beamsplitter followed by measurement in the two output ports can swap the entanglement to the two spin states. A schematic of this process is shown in Fig. 2.4. A more elaborate discussion on

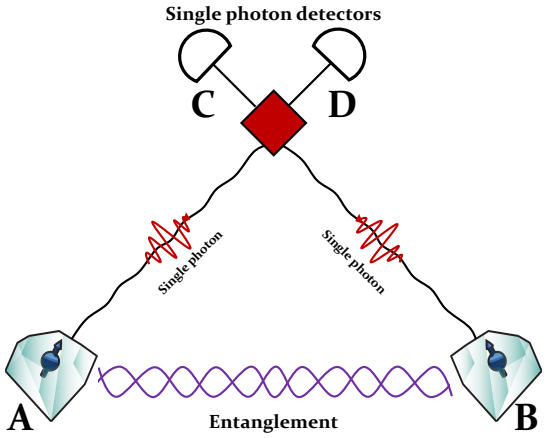

Figure 2.4: Entanglement generation between two NV centers, A and B, is established by interference of two emitted single photons, followed by detection in the two output ports C and D of the beamsplitter (red square).

photon overlap on a beamsplitter is included in Chapter 3. For now, it is assumed that the two photons emitted by the two NV centers are indistinguishable. Two different spin-spin entanglement schemes can be used, the first being the Single-Click scheme, requiring the detection of only one photon, and the second being the Barett and Kok scheme, requiring the detection of two photons.

Single-Click

The single-click scheme has a high entanglement generation rate as it only requires a single photon detection event. However, it requires active phase stabilisation, as will be shown soon after. The single-click protocol consists of the following steps:

1. Entangle NV_A with photon p_A and NV_B with photon p_B according to the procedure with the presence-absence encoding of the photons described in the section Spin-Photon Entanglement. The total state of both NV's and photons is then given as

$$(\sqrt{\alpha}\,|\uparrow\rangle\,|1\rangle + \sqrt{1-\alpha}\,|\downarrow\rangle\,|0\rangle)_A \otimes (\sqrt{\alpha}\,|\uparrow\rangle\,|1\rangle + \sqrt{1-\alpha}\,|\downarrow\rangle\,|0\rangle)_B \tag{2.1}$$

   The two photons are assumed to have the same frequency and polarisation.

2. The photons travel towards a balanced beamsplitter. This means that a photon entering the beamsplitter in one of the two input arms, has an equal probability to end up in one of the two output arms. It is assumed that the two photons arrive simultaneously at the beamsplitter. Therefore, the photons are indistinguishable. The beamsplitter has the input ports labelled A and B, and the exit ports labelled as C, D. The operation of the 50/50 beamsplitter on a photon number state with either 0 or 1 incoming photons in paths A and B can then be represented by the following equations [18]:

$$\begin{aligned}
|0\rangle_A\,|0\rangle_B &\rightarrow |0\rangle_C\,|0\rangle_D \\
|0\rangle_A\,|1\rangle_B &\rightarrow \frac{1}{\sqrt{2}}\,(|0\rangle_C\,|1\rangle_D + |1\rangle_C\,|0\rangle_D) \\
|1\rangle_A\,|0\rangle_B &\rightarrow \frac{1}{\sqrt{2}}\,(|0\rangle_C\,|1\rangle_D - |1\rangle_C\,|0\rangle_D) \\
|1\rangle_A\,|1\rangle_B &\rightarrow \frac{1}{\sqrt{2}}\,(|0\rangle_C\,|2\rangle_D - |2\rangle_C\,|0\rangle_D)
\end{aligned} \tag{2.2}$$

   Further explanation on the operations of beamsplitters is included in Chapter 3. The beamsplitter performs the operations given in Eq. (2.2) on the state given in Eq. (2.1). The state of the total system then becomes:

$$\begin{aligned}
&\frac{\alpha}{\sqrt{2}}\,|\uparrow\rangle_A\,|\uparrow\rangle_B\,(|0\rangle_C\,|2\rangle_D - |2\rangle_C\,|0\rangle_D) + \\
&\qquad \sqrt{(\alpha-\alpha^2)/2}\,(|\uparrow\rangle_A\,|\downarrow\rangle_B + |\downarrow\rangle_A\,|\uparrow\rangle_B)\,|0\rangle_C\,|1\rangle_D + \\
&\qquad \sqrt{(\alpha-\alpha^2)/2}\,(|\uparrow\rangle_A\,|\downarrow\rangle_B - |\downarrow\rangle_A\,|\uparrow\rangle_B)\,|1\rangle_C\,|0\rangle_D + \\
&\qquad\qquad (1-\alpha)\,|\downarrow\rangle_A\,|\downarrow\rangle_B\,|0\rangle_C\,|0\rangle_D
\end{aligned} \tag{2.3}$$

3. Two detectors in the two output ports of the beamsplitter will detect the photons after the beamsplitter. When one detector detects the presence of photons, and the other does not, heralded entanglement generation will be declared a success. However, the photon detectors are not photon number resolving, so they cannot distinguish between one and two photons. Therefore, the final state after the success event will be a mixed state of the target state $\left|\Psi^{\pm}\right\rangle \propto (|\uparrow\rangle_A\,|\downarrow\rangle_B \pm e^{-i\phi}\,|\downarrow\rangle_A\,|\uparrow\rangle_B)$ and $|\uparrow\rangle_A\,|\uparrow\rangle_B$. Also, an internal phase ϕ, has to be incorporated. This phase is composed from several phase accumulation processes, such as the fluctuations in optical path length and the phase of the short RO laser pulse at the position of the NV used for excitation [4][19]. The final quantum state after a detection in one detector is therefore described by the following density matrix:

$$|\Psi\rangle\langle\Psi| = (1-\alpha)\left|\Psi^{\pm}(\phi)\right\rangle\left\langle\Psi^{\pm}(\phi)\right| + \alpha\,|\uparrow\rangle_A\,|\uparrow\rangle_B\,\langle\uparrow|_A\,\langle\uparrow|_B\,, \tag{2.4}$$

   where $\left|\Psi^{\pm}(\phi)\right\rangle = \frac{1}{\sqrt{2}}(|\uparrow\rangle_A\,|\downarrow\rangle_B \pm e^{-i\phi}\,|\downarrow\rangle_A\,|\uparrow\rangle_B)$, with the sign depending on which detector clicked. The internal phase ϕ must be tracked or stabilized during experiments, otherwise the entangled pair is lost.

The fidelity of the final quantum state upon detection of a photon in one of the detectors is then given as $F = 1-\alpha$. If this entanglement scheme is applied, there is a trade-off between the fidelity, which decreases with increasing α, and the entanglement generation rate, which increases with increasing α, as the probability of a photon detection event depends directly on the bright state population.

Barett and Kok

The Barett and Kok entanglement scheme [20] has the advantage that it does not require active phase stabilisation, yet the rate of entanglement generation is lower than with the single click scheme, as it requires two single photon detection events. It consists of the steps presented below [19].

1. Entangle NV_A with photon p_A and NV_B with photon p_B according to the procedure with the time-bin encoding of the photons described in the section Spin-Photon Entanglement. The total state of the two NV centers with their photons is then given as

$$\frac{1}{2}(|\downarrow\rangle|E\rangle + |\uparrow\rangle|L\rangle)_A \otimes (|\downarrow\rangle|E\rangle + |\uparrow\rangle|L\rangle)_B \tag{2.5}$$

2. The photons travel towards the beamsplitter. The operations of the beamsplitter on the photon number input states as in Eq. (2.2) are rewritten to include the difference between the early and late time bin encoding in Eq. (2.6)

$$\begin{aligned}
|E\rangle_A|E\rangle_B &\rightarrow \frac{1}{\sqrt{2}}(|0\rangle_C|2\rangle_D - |2\rangle_C|0\rangle_D)_E \\
|E\rangle_A|L\rangle_B &\rightarrow \frac{1}{\sqrt{2}}(|0\rangle_C|1\rangle_D - |1\rangle_C|0\rangle_D)_E \otimes \frac{1}{\sqrt{2}}(|0\rangle_C|1\rangle_D + |1\rangle_C|0\rangle_D)_L \\
|L\rangle_A|E\rangle_B &\rightarrow \frac{1}{\sqrt{2}}(|0\rangle_C|1\rangle_D - |1\rangle_C|0\rangle_D)_L \otimes \frac{1}{\sqrt{2}}(|0\rangle_C|1\rangle_D + |1\rangle_C|0\rangle_D)_E \\
|L\rangle_A|L\rangle_B &\rightarrow \frac{1}{\sqrt{2}}(|0\rangle_C|2\rangle_D - |2\rangle_C|0\rangle_D)_L
\end{aligned} \tag{2.6}$$

   Here, it was assumed that the time difference between the early and late time bins is large enough such that two photons are fully distinguishable in arrival time. Therefore, the distinction is made between photons in output ports C or D in the early or late state. The beamsplitter acts on the state in Eq. (2.5), yielding the following state:

$$\begin{aligned}
&\frac{1}{2}|\downarrow\rangle_A|\downarrow\rangle_B \left\{\frac{1}{\sqrt{2}}(|0\rangle_C|2\rangle_D - |2\rangle_C|0\rangle_D)_E\right\} + \\
&\qquad \frac{1}{2}|\downarrow\rangle_A|\uparrow\rangle_B \left\{\frac{1}{\sqrt{2}}(|0\rangle_C|1\rangle_D - |1\rangle_C|0\rangle_D)_E \otimes \frac{1}{\sqrt{2}}(|0\rangle_C|1\rangle_D + |1\rangle_C|0\rangle_D)_L\right\} + \\
&\qquad \frac{1}{2}|\uparrow\rangle_A|\downarrow\rangle_B \left\{\frac{1}{\sqrt{2}}(|0\rangle_C|1\rangle_D - |1\rangle_C|0\rangle_D)_L \otimes \frac{1}{\sqrt{2}}(|0\rangle_C|1\rangle_D + |1\rangle_C|0\rangle_D)_E\right\} + \\
&\qquad\qquad \frac{1}{2}|\uparrow\rangle_A|\uparrow\rangle_B \left\{\frac{1}{\sqrt{2}}(|0\rangle_C|2\rangle_D - |2\rangle_C|0\rangle_D)_L\right\}
\end{aligned} \tag{2.7}$$

   where the labels A, B indicate the NV center, C and D indicate in which output port of the beamsplitter the photons are located, and E, L indicate when in time the photons exist.

3. Detection of a photon in both the early and the late time bin collapses the state in Eq. (2.7) to

$$|\Psi\rangle = \frac{1}{\sqrt{2}}(|\uparrow\rangle_A|\downarrow\rangle_B \pm |\downarrow\rangle_A|\uparrow\rangle_B), \tag{2.8}$$

   with a + sign for two clicks in the same detector (so twice a click in output port C, or twice in D), and a − sign for one click in each detector in the two rounds. This state is entangled, therefore the detection of a photon in both the early and late time bin heralds entanglement. The internal phase ϕ present in (2.4) is changed into a global phase by the additional optical excitation, meaning that this protocol is in theory insensitive to dephasing mechanisms.

This scheme does not limit the fidelity of the entangled state as in the single-click scheme. Also, it is not necessary to control or keep track of the picked up phase, as long as the possible phase fluctuations occur on a longer time scale than the time between the first and second photon detection event. The success probability, or entanglement rate, however, is lower than in the single-click scheme, as two photon detections are required. It is given as $P = 1/2\eta_A\eta_B$, where η_i is the overall detection efficiency of ZPL photons from NV_i, and the factor $1/2$ accounts for the fact that the spins can be projected into $|\downarrow\rangle_A|\downarrow\rangle_B$ (first term of Eq. (2.7)) or $|\uparrow\rangle_A|\uparrow\rangle_B$ (last term of Eq. (2.7)). These two possibilities are filtered out by their different photon signature [19].

2.3 Frequency Conversion

To be able to generate spin-spin entanglement between two nodes separated by metropolitan distances, the photons need to travel this distance over optical fibers. A main limitation are the losses in the optical fibers, which are in the order of 8 dB/km for the resonant photons emitted by NV centers with a wavelength of 637 nm [5]. Quantum-coherent frequency conversion to the telecom band (1588 nm) can mitigate these losses substantially: in this frequency range, photons can be transmitted with losses in the order of only 0.2 dB/km [6].

The non-linear optical process of difference frequency generation (DFG) is used to change the frequency of the target photons. The NV photons are combined with a strong pump laser at 1064 nm inside a periodically poled litium niobate (PPLN) crystal. The two input photons are annihilated while simultaneously one photon at a wavelength of λ_{target} is generated:

$$\lambda_{\text{target}} = \left(\frac{1}{\lambda_{\text{NV}}} - \frac{1}{\lambda_{\text{pump}}} \right)^{-1} \tag{2.9}$$

where $\lambda_{\text{NV}} = 637\,\text{nm}$ and $\lambda_{\text{pump}} = 1064\,\text{nm}$ such that $\lambda_{\text{target}} = 1588\,\text{nm}$ thus conserving both energy and momentum. In [5], it is shown that this frequency conversion preserves the quantum properties of the photons. Another advantage is that the frequency of the target photon can be precisely tuned by changing the pump laser frequency, such that two photons from different setups can be tuned to have the exact same frequency after the conversion process. The total front-to-end conversion efficiency of the quantum frequency converter (QFC) in which the PPLN crystal is located is in the order of 50%.

After the QFC, a spectral filtering process is applied to extract the down-converted photons from the high background noise. Possible contributions of this background are leakage photons from the pump laser, or noise that is generated in the DFG process. This filtering process introduces extra losses.

Chapter 3

Theory Two-Photon Quantum Interference

The remarkable quantum effect called Two-Photon Quantum Interference (TPQI) was first discovered in 1987 by C.K. Hong, Z.Y. Ou and L. Mandel [21]. It requires a beamsplitter with two input and two output arms that is as balanced (50/50) as possible. When a single photon impinges on a 50/50 beamsplitter in one of the two input arms, it has a 50% chance of being transmitted, and a 50% chance of being reflected. When two single photons, indistinguishable in all their properties being arrival time, frequency and polarisation, arrive at a 50/50 beamsplitter in distinct input paths, they will always exit together in one of the two output paths. This bunching effect originates from the Bose-Einstein statistics of single photons [22]. This means that coincidences - each photon in a distinct output path - will not be measured. The drop in coincidences as a function of the delay between the two photon wave packets is also referred to as a HOM dip.

In this chapter, the coincidence probability as a function of the detection time difference of the photons will be derived analytically, for various splitting ratios of the beamsplitter, arrival time differences, and frequency differences of the photons. Secondly, the probability that two photons arrive simultaneously at the beamsplitter will be derived for a self-interference TPQI experiment using a simple counting argument.

3.1 Derivation Coincidence Probability

In this section, an analytical expression will be derived for the probability that two single photons, incident in different input ports of a beamsplitter, will be detected in distinct output ports of the beamsplitter. The single photons in this model are emitted by NV centers and therefore described by a one-sided exponential decay. This derivation follows the approach in [23], with adaptations inspired by [10] and [24]. It is assumed that the polarisation state of the two photons is equal - something which can be realised in experiment with high polarisation extinction ratio filters. Note that this derivation can be used for both single NV and two NV TPQI experiments.

First, a mathematical background on beamsplitters will be given. Next, an expression for the joint detection probability will be derived for an imbalanced beamsplitter. Using one-sided exponential decay as photon wave functions, the coincidence probability can then be derived as a function of the detection time difference, the arrival time difference and the frequency difference of the photons, and of the splitting ratio's of the beamsplitter.

3.1.1 Beamsplitters

A lossless, imbalanced beamsplitter with input arms labelled S and L and output arms labelled 1 and 2 can be described by the following unity matrix $\mathcal{U}_{BS}$,

$$\mathcal{U}_{BS} = \begin{pmatrix} \sqrt{R} & \sqrt{T} \\ \sqrt{T} & -\sqrt{R} \end{pmatrix} \tag{3.1}$$

with R and T being its reflectivity and transmissivity, so $R+T=1$. See also Fig. 3.1.

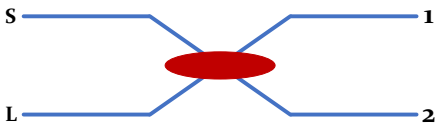

Figure 3.1: Schematic representation of a beamsplitter with incoming paths S and L, and exiting paths 1 and 2.

If two photons arrive in distinct input modes S and L of the beamsplitter, a classical way of thinking would tell us that there are four possibilities for the two photons to exit the beamsplitter:

1. Photon S and photon L exit both in output port 1 - S is reflected, and L is transmitted.
2. Photon S exits in output port 1 and photon L exits in output port 2 - both photons are reflected.
3. Photon S exits in output port 2 and photon L exits in output port 1 - both photons are transmitted.
4. Photon S and photon L exit both in output port 2 - S is transmitted, and L is reflected.

For fully distinguishable photons, this classical derivation holds. A coincidence event, meaning two photons in distinct output ports, is described by possibility 2 and 3. The probability of such a coincidence event is then given as

$$P_{\text{coinc}}(\text{dist.}|\text{diff. input}) = R^2 + T^2. \tag{3.2}$$

In the case of a balanced beamsplitter ($R=T=1/2$) , this gives a coincidence probability of $\frac{1}{2}$.
If two fully distinguishable photons arrive at the beamsplitter in the same input arm, so either both in input mode S or both in input mode L, the coincidence probability can also be derived classically. Now, a coincidence only occurs if the first photon is reflected and the second photon transmitted, or the other way around. This results in a probability of a coincidence event given as

$$P_{\text{coinc}}(\text{dist.}|\text{equal input}) = 2RT. \tag{3.3}$$

Again, this yields a coincidence probability of $\frac{1}{2}$ in the case of a balanced beamsplitter.

For indistinguishable photons, a different approach of calculating the coincidence probability is needed. The relation between the number of photons between the input and output arms of the beamsplitter can also be described using creation and annihilation operators. Using the creation operator $\hat{a}_i^\dagger$ for the creation of a photon in channel i, we can write the initial quantum state of two photons at distinct entrance ports of a beamsplitter as $\hat{a}_S^\dagger \hat{a}_L^\dagger |0_S 0_L\rangle = |1_S 1_L\rangle$. The creation operators in the output arms are related to the creation operators in the input arms as

$$\begin{pmatrix} \hat{a}_S^\dagger \\ \hat{a}_L^\dagger \end{pmatrix} = \begin{pmatrix} \sqrt{R} & \sqrt{T} \\ \sqrt{T} & -\sqrt{R} \end{pmatrix} \cdot \begin{pmatrix} \hat{a}_1^\dagger \\ \hat{a}_2^\dagger \end{pmatrix} = \begin{pmatrix} \sqrt{R}\hat{a}_1^\dagger + \sqrt{T}\hat{a}_2^\dagger \\ \sqrt{T}\hat{a}_1^\dagger - \sqrt{R}\hat{a}_2^\dagger \end{pmatrix}, \tag{3.4}$$

where we used that $\mathcal{U}_{BS}^{-1} = \mathcal{U}_{BS}$.

Using the Fock state representation of n single photons, $|n\rangle$, the creation and annihilation operators act on this state as follows [1]:

$$\begin{aligned} \hat{a}^\dagger |n\rangle &= \sqrt{n+1}\,|n+1\rangle \quad \text{for } n \in \mathbb{N} \cup \{0\} \\ \hat{a}|n\rangle &= \begin{cases} \sqrt{n}\,|n-1\rangle & \text{for } n \in \mathbb{N} \\ 0 & \text{for } n = 0 \end{cases} \end{aligned} \tag{3.5}$$

Therefore, the input state $\hat{a}_S^\dagger \hat{a}_L^\dagger |0_S 0_L\rangle$ will be projected to

$$\begin{aligned} \hat{a}_S^\dagger \hat{a}_L^\dagger |0_S 0_L\rangle &= (\sqrt{R}\hat{a}_1^\dagger + \sqrt{T}\hat{a}_2^\dagger)(\sqrt{T}\hat{a}_1^\dagger - \sqrt{R}\hat{a}_2^\dagger)\,|0_1 0_2\rangle \\ &= \left(\sqrt{RT}[\hat{a}_1^\dagger]^2 - R\hat{a}_1^\dagger \hat{a}_2^\dagger + T\hat{a}_1^\dagger \hat{a}_2^\dagger - \sqrt{RT}[\hat{a}_2^\dagger]^2\right)|0_1 0_2\rangle \\ &= \sqrt{2RT}\,(|2_1 0_2\rangle - |0_1 2_2\rangle) + (T-R)\,|1_1 1_2\rangle\,. \end{aligned} \tag{3.6}$$

If the beamsplitter is balanced, the output state will be $(|2_1 0_2\rangle - |0_1 2_2\rangle)/\sqrt{2}$ - i.e. both photons will always leave through the same output port. This is what is called Two-Photon Quantum Interference. In the case of an imbalanced beamsplitter, a fraction of $4RT$ photons will leave the same output port, and a fraction of $(T-R)^2$ photons will leave in different output ports, yielding a coincidence probability of $(T-R)^2$.

The transformations in Eq. (3.4) can also be expressed in terms of electric field operators of the two input (S, L) - and output $(1, 2)$ modes. The electric field operators of mode i read

$$\begin{aligned} \hat{E}_i^+(t) &= \zeta_i(t)\hat{a}_i \\ \hat{E}_i^-(t) &= \zeta_i^*(t)\hat{a}_i^\dagger, \end{aligned} \tag{3.7}$$

where $\zeta_i(t)$ is the normalized field mode of a photon in mode i [23][25]. Therefore, we can write in analogy with Eq. (3.4):

$$\begin{aligned} \hat{E}_1^\pm(t) &= \sqrt{R}\hat{E}_S^\pm(t) + \sqrt{T}\hat{E}_L^\pm(t) \\ \hat{E}_2^\pm(t) &= \sqrt{T}\hat{E}_S^\pm(t) - \sqrt{R}\hat{E}_L^\pm(t). \end{aligned} \tag{3.8}$$

3.1.2 Joint Detection Probability

The probability for photon detections in output ports 1 and 2 at times t_1 and t_2, respectively, is called the joint detection probability. The probability of measuring a photon at time t given that it is present in mode i is given by $\langle 1_i|\hat{E}_i^-(t)\hat{E}_i^+(t)|1_i\rangle$ [23]. Therefore, we can write for the joint detection probability

$$\begin{aligned} P_{\text{joint}}(t_1, t_2) &= \langle 1_S 1_L|\hat{E}_1^-(t_1)\hat{E}_2^-(t_2)\hat{E}_2^+(t_2)\hat{E}_1^+(t_1)|1_S 1_L\rangle \\ &= |T\zeta_S(t_2)\zeta_L(t_1) - R\zeta_L(t_2)\zeta_S(t_1)|^2. \end{aligned} \tag{3.9}$$

Here, equations (3.8) and (3.5) were used. The full derivation can be found in the Appendix, see A.2. In the case of a balanced beamsplitter with, the joint detection probability is given by $P_{\text{joint}}(t_1, t_2) = \frac{1}{4}|\zeta_S(t_2)\zeta_L(t_1) - \zeta_L(t_2)\zeta_S(t_1)|^2$, as derived in [23].

3.1.3 Photon Wave Function

Single photons emitted by NV centers in diamond can be described mathematically by a one-sided exponentially decaying wave packet [24]. If two photons emitted by the same NV center arrive asynchronously at two distinct input ports (S, L) of the beamsplitter at arrival times dt_S and dt_L, we can write their wave functions as

$$\begin{aligned} \zeta_S(t) &= \frac{1}{\sqrt{\tau_l}}\exp\left[-i(\omega - \Delta/2)t\right]\cdot\exp\left[-\frac{t-dt_S}{2\tau_l}\right]\cdot \mathrm{H}(t-dt_S) \\ \zeta_L(t) &= \frac{1}{\sqrt{\tau_l}},\exp\left[-i(\omega + \Delta/2)t\right]\cdot\exp\left[-\frac{t-dt_L}{2\tau_l}\right]\cdot \mathrm{H}(t-dt_L), \end{aligned} \tag{3.10}$$

where:

- τ_l is the excited state radiative lifetime of the emitted photons
- ω is the central frequency of the two emitted photons (i.e. $\omega = (\omega_S + \omega_L)/2$)
- Δ is the frequency difference of the two photons, defined as $\Delta = \omega_L - \omega_S$

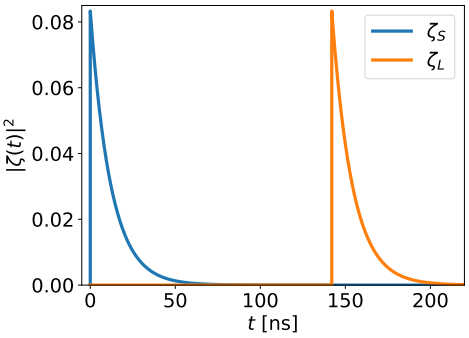

Figure 3.2: Probability amplitude of the wavefunctions ζ_S and ζ_L as a function of time t. Photon S arrives at $dt_S = 0$ ns and photon L arrives at $dt_L = 142$ ns. The lifetime is set to $\tau_l = 12$ ns.

The Heaviside-function $\mathrm{H}(t)$ ensures normalisation of the wave functions, i.e. $\int_{-\infty}^{\infty}|\zeta(t)|^2 dt = 1$ and removes any restrictions on the time t: it can take all values from $-\infty$ to $+\infty$. In Fig. 3.2, the probability amplitudes of the wavefunctions of Eq.(3.10) are displayed as a function of time, for a lifetime of $\tau_l = 12$ ns and an arrival time of photon S at $dt_S = 0$ ns and an arrival time of photon L at $dt_L = 142$ ns.

3.1.4 Coincidence Probability

Derive P_{joint}

Using the single photon wavefunctions given in Eq.(3.10), the joint detection probability given in Eq.(3.9) is derived and reads

$$P_{\text{joint}}(t_1, t_2, dt_S, dt_L) = \frac{1}{{\tau_l}^2} \exp\left[\frac{-t_1 - t_2}{\tau_l}\right] \exp\left[\frac{dt_S + dt_L}{\tau_l}\right] \cdot \left\{R^2 \cdot f_R(t_1, t_2, dt_S, dt_L) + T^2 \cdot f_T(t_1, t_2, dt_S, dt_L) - 2RT\cos\Delta(t_2 - t_1) \cdot f_{RT}(t_1, t_2, dt_S, dt_L)\right\} \tag{3.11}$$

with the terms

$$\begin{aligned} f_R(t_1, t_2, dt_S, dt_L) &= \mathrm{H}(t_1 - dt_S)\mathrm{H}(t_2 - dt_L), \\ f_T(t_1, t_2, dt_S, dt_L) &= \mathrm{H}(t_1 - dt_L)\mathrm{H}(t_2 - dt_S) \text{ and} \\ f_{RT}(t_1, t_2, dt_S, dt_L) &= f_R(t_1, t_2, dt_S, dt_L) f_T(t_1, t_2, dt_S, dt_L), \end{aligned} \tag{3.12}$$

where it was used that $\mathrm{H}^2(t) = \mathrm{H}(t)$. The full derivation can be found in the Appendix, see A.2. When $dt_S = dt_S$, meaning the photons have the same arrival time, this expression simplifies to

$$P_{\text{joint}}(t_1, t_2, dt) = \frac{1}{{\tau_l}^2} \exp\left[\frac{-t_1 - t_2}{\tau_l}\right] \exp\left[\frac{2dt}{\tau_l}\right] \left(R^2 + T^2 - 2RT\cos\Delta(t_2 - t_1)\right) \cdot \mathrm{H}(t_1 - dt)\mathrm{H}(t_2 - dt) \tag{3.13}$$

where dt is the arrival time of the two photons.

Include inhomogeneous broadening of frequency difference Δ

An undisturbed NV center has a Lorentzian spectral profile, with a FWHM of $\frac{1}{2\pi\tau_l}$, peaked at the resonance frequency of the ZPL, being 637 nm [24]. The emission line can be broadened by several processes. Homogeneous broadening of the emission line is caused by dynamic processes which are intrinsic to the molecular system, such as pure dephasing. The homogeneous broadening takes place at the time scale of the free evolution transverse relaxation time T_2, which is in the order of microseconds for NV centers [10]. On the other hand, inhomogeneous broadening processes of the emission line are caused by static effects, originating from for example local electric or magnetic field variations due to charge fluctuations in the diamond lattice [26][19]. Inhomogeneous broadening can be considered as a static ensemble averaging effect, essentially hiding the dynamical effects of homogeneous broadening [27]. The distribution function describing this process is a Gaussian.

As TPQI experiments are typically done in the limit of a long integration time, the frequency of the emitted photons is assumed to be Gaussian distributed [23]. Therefore, the frequency difference (Δ) of two photons originating from two different emitters is also Gaussian distributed with a standard deviation of σ_Δ and an average of μ_Δ. It is assumed that the frequency difference of two photons originating from a single NV center is also Gaussian distributed. This frequency distribution, $f(\Delta)$, is given as

$$f(\Delta) = \frac{1}{\sigma_\Delta\sqrt{2\pi}} e^{-\frac{1}{2}\left(\frac{\Delta - \mu_\Delta}{\sigma_\Delta}\right)^2}. \tag{3.14}$$

The inhomogeneously broadened joint detection probability $P_{\text{inh}}(t_1, t_2, dt_S, dt_L, \mu_\Delta, \sigma_\Delta)$ is then given as the integral over all possible values of Δ of the product of $f(\Delta)$ and $P_{\text{joint}}(t_1, t_2, dt_S, dt_L)$:

$$\begin{aligned} P_{\text{inh}}(t_1, t_2, dt_S, dt_L, \mu_\Delta, \sigma_\Delta) &= \int_{-\infty}^{\infty} f(\Delta) P_{\text{joint}}(t_1, t_2, dt_S, dt_L)\mathrm{d}\Delta \\ &= \frac{\exp\left[\frac{-t_1 - t_2}{\tau_l}\right]}{{\tau_l}^2} \exp\left[\frac{dt_S + dt_L}{\tau_l}\right] \left(R^2 f_R + T^2 f_T \right. \\ &\qquad \left. -2RT f_{RT} \cdot \exp\left[\frac{-\sigma_\Delta^2 (t_2 - t_1)^2}{2}\right] \cdot \cos\mu_\Delta(t_2 - t_1)\right). \end{aligned} \tag{3.15}$$

When $dt_S = dt_L := dt$, this expression simplifies to

$$\begin{aligned} P_{\text{inh}}(t_1, t_2, dt, \mu_\Delta, \sigma_\Delta) &= \int_{-\infty}^{\infty} f(\Delta) P_{\text{joint}}(t_1, t_2, dt) \mathrm{d}\Delta \\ &= \frac{1}{{\tau_l}^2} \exp\left[\frac{-t_1 - t_2}{\tau_l}\right] \exp\left[\frac{2dt}{\tau_l}\right] \mathrm{H}(t_1 - dt)\mathrm{H}(t_2 - dt) \\ &\quad \left(R^2 + T^2 - 2RT \cdot \exp\left[-\frac{\sigma_\Delta^2 (t_2 - t_1)^2}{2}\right] \cdot \cos \mu_\Delta (t_2 - t_1)\right). \end{aligned} \tag{3.16}$$

Integrate over all detection times t_1 and t_2

If we put no constraints on the detection times t_1 and t_2, we can derive an analytical expression for the coincidence probability as a function of the detection time difference $\tau := t_2 - t_1$, by integrating P_{inh} over all times $t := t_1$. Next to the variable change $t = t_1$ and $\tau = t_2 - t_1$, an arrival time difference $\delta = dt_S - dt_L$ is defined for easing the calculations. This yields $P(\tau, \mu_\Delta, \sigma_\Delta, \delta)$ given in Eq. (3.17).

$$\begin{aligned} P(\tau, \mu_\Delta, \sigma_\Delta, \delta) &= \int_{-\infty}^{\infty} P_{\text{inh}}(t, \tau, \sigma_\Delta, \delta)\, \mathrm{d}t \\ &= \frac{1}{2\tau_l} \left(R^2 \exp\left[\frac{-|\tau + \delta|}{\tau_l}\right] + T^2 \exp\left[\frac{-|\tau - \delta|}{\tau_l}\right] \right. \\ &\quad \left. -2RT \cdot \exp\left[-\frac{|\tau|}{\tau_l} - \frac{|\delta|}{\tau_l} - \frac{\sigma_\Delta^2 \tau^2}{2}\right] \cdot \cos \mu\tau \right). \end{aligned} \tag{3.17}$$

The full derivation of this coincidence probability, which is mostly equivalent to the derivation just presented, can be found in the Appendix.

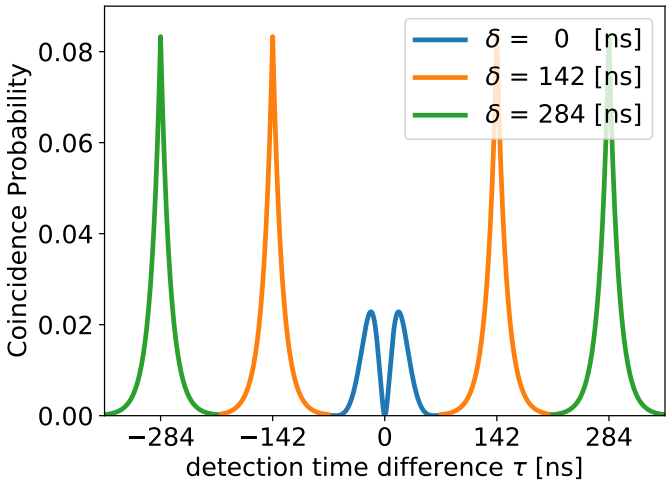

Figure 3.3: Coincidence probability versus detection time difference τ when restrictions on the detection times are applied, for arrival time differences of $\delta = 0, 142$ and 284 ns, a balanced beamsplitter, and a mean frequency difference of μ_Δ =100 MHz.

This coincidence probability is plotted as a function of τ for the arrival time differences of $\delta = 0, 142$ and 284 ns, a balanced beamsplitter ($R = T = 0.5$), $\sigma_\Delta = 0$ and μ_Δ =100 MHz in Fig. 3.3. These arrival time differences were chosen as they are the same as in the single NV TPQI experiment, which will be discussed in Chapter 5. This shows that even if the mean frequency difference between two photons is non-zero, perfect two-photon quantum interference (zero coincidence probability at $\tau = 0$) can be observed if the detectors have a high enough time resolution. Also, the shape of the interference dip around $\tau = 0$ is determined directly by the parameters μ_Δ and σ_Δ. Therefore, a fit on this dip of measured coincidences in an experiment can give information on the frequency difference distribution of the two photons, as was done for example in [28].

Integrate over constraint detection times t_1 and t_2

In an experiment, finite time windows are selected in which the photon detections must take place. This adds a constraint on the detection time t_1 of the photon in detector 1 and on the detection time t_2 of the photon in detector 2. A distinction must be made between the case where photons arrive at the same time at the beamsplitter, the case when the arrival time difference is large ($|dt_S - dt_L| >> \tau_l$) and the case when the arrival time difference is small ($|dt_S - dt_L| \approx \tau_l$).

Large arrival time difference When the photons arrive at the beamsplitter at times dt_S and dt_L, where $|dt_S - dt_L| >> \tau_l$, then there are two possible detection time windows for both detectors, window I and window II. Window I is defined as the interval $W_I = [dt_S + WS, dt_S + WE]$ where $WS > 0$ and $WE > WS$. Window II is defined as the interval $W_{II} = [dt_L + WS, dt_L + WE]$.

The detection time of photon 1 can be either in window I or in window II. Thus t_1 is constraint to $t_1 \in \{W_I, W_{II}\}$. The possible detection times of photon 2 is dependent on the detection time of photon 1. If photon 1 is detected in window I, then photon 2 can only be detected in window II, and vice versa. Therefore, we write out the two cases separately.

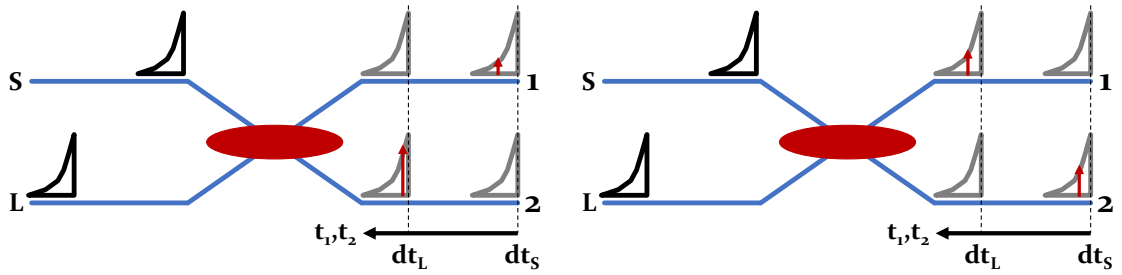

(a) Detector 1 clicks first, so $t_1 \in W_I$ and $t_2 \in W_{II}$.

(b) Detector 2 clicks first, so $t_2 \in W_I$ and $t_1 \in W_{II}$

Figure 3.4: Different possibilities of detection times t_1, t_2 given two photons in distinct inputs of the beamsplitter at a large arrival time difference. Photon detections are marked with a red arrow.

The coincidence probability when detector 1 clicks first, followed by a click in detector 2, given two photons in input ports S and L at a large arrival time difference where photon S arrives earlier than photon L ($dt_S << dt_L$), is obtained by integrating P_{inh} over all detection times t_1 and t_2, where $t_1 \in W_I$ and $t_2 \in W_{II}$:

$$P_{\text{coinc}}(\text{det1 first}|dt_S << dt_L) = \int_{t_2 \in W_{II}} \int_{t_1 \in W_I} P_{\text{inh}}(t_1, t_2, dt_S, dt_L, \mu_\Delta, \sigma_\Delta) \mathrm{d}t_1 \mathrm{d}t_2. \tag{3.18}$$

This integral can be solved numerically by applying the Simpson's rule [29]. A schematic picture of this situation is shown in Fig. 3.4a.

In a similar manner, the coincidence probability when detector 2 clicks first given two photons in distinct input ports at a large arrival time difference is derived. Now, the constraint on the detection times are $t_2 \in W_I$ and $t_1 \in W_{II}$. This yields

$$P_{\text{coinc}}(\text{det2 first}|dt_S << dt_L) = \int_{t_2 \in W_I} \int_{t_1 \in W_{II}} P_{\text{inh}}(t_1, t_2, dt_S, dt_L, \mu_\Delta, \sigma_\Delta) \mathrm{d}t_1 \mathrm{d}t_2. \tag{3.19}$$

A schematic picture of this situation is shown in Fig. 3.4b. The situation where photon L arrives earlier than photon S can be obtained in a similar manner.

Small arrival time difference The photons can also arrive at the beamsplitter at a very small arrival time difference, being $|dt_S - dt_L| << \tau_l$, for example due to wrong calibration of the photon generation times. A schematic representation of this situation is shown in Fig 3.5a. We assume that photon S arrives a time $D/2$ too soon, and photon L a time $D/2$ too late. The detection time windows are calibrated to

the case with 0 arrival time difference, so assuming $dt_S = dt_L := dt$, thus the detection times t_1 and t_2 are constraint to the same window $W = [dt + WS, dt + WE]$. This yields a coincidence probability of

$$P_{\text{coinc}}(dt_S \approx dt_L) = \int_{t_2 \in W} \int_{t_1 \in W} P_{\text{inh}}(t_1, t_2, dt_S - D/2, dt_L + D/2, \mu_\Delta, \sigma_\Delta) \mathrm{d}t_1 \mathrm{d}t_2. \tag{3.20}$$

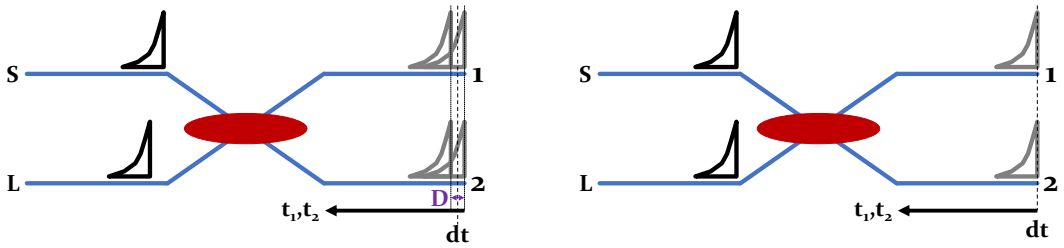

(a) A small arrival time difference of D of the two photons.

(b) Zero arrival time difference of the two photons.

Figure 3.5: Different possibilities of detection times t_1, t_2 given two photons in distinct inputs of the beamsplitter at either small (D) or zero arrival time difference.

Zero arrival time difference When the photons arrive at the beamsplitter at the same time, being $dt_S = dt_S := dt$, then the detection times t_1 and t_2 are constrained to the same window, being the interval $W = [dt + WS, dt + WE]$. See also Fig. 3.5b. This yields a coincidence probability of

$$\begin{aligned}
P_{\text{coinc}}(dt_S = dt_L) &= \int_{t_2 \in W} \int_{t_1 \in W} P_{\text{inh}}(t_1, t_2, dt, \mu_\Delta, \sigma_\Delta) \mathrm{d}t_1 \mathrm{d}t_2 \\
&= \int_{t_2 \in W} \left(\frac{1}{\tau_l} \exp\left[\frac{-t_2 + dt}{\tau_l} \right] \left(R^2 + T^2\right) \left(\exp\left[-\frac{WS}{\tau_l} \right] - \exp\left[-\frac{WE}{\tau_l} \right] \right) \right) \mathrm{d}t_2 \\
&\quad - 2RT \int_{t_2 \in W} \int_{t_1 \in W} \frac{1}{{\tau_l}^2} \exp\left[\frac{2dt}{\tau_l} \right] \exp\left[\frac{-t_1 - t_2}{\tau_l} \right] \exp\left[-\frac{\sigma_\Delta^2 (t_2 - t_1)^2}{2} \right] \cdot \cos \mu_\Delta (t_2 - t_1) \mathrm{d}t_1 \mathrm{d}t_2 \\
&= \left(R^2 + T^2\right) \left(\exp\left[-\frac{WS}{\tau_l} \right] - \exp\left[-\frac{WE}{\tau_l} \right] \right)^2 \\
&\quad - 2RT \int_{t_2 \in W} \int_{t_1 \in W} \frac{1}{{\tau_l}^2} \exp\left[\frac{2dt}{\tau_l} \right] \exp\left[\frac{-t_1 - t_2}{\tau_l} \right] \exp\left[-\frac{\sigma_\Delta^2 (t_2 - t_1)^2}{2} \right] \cdot \cos \mu_\Delta (t_2 - t_1) \mathrm{d}t_1 \mathrm{d}t_2
\end{aligned} \tag{3.21}$$

If the two photons are perfectly indistinguishable in their frequencies, we can further evaluate this coincidence probability by setting $\sigma_\Delta = \mu_\Delta = 0$. This yields:

$$P_{\text{coinc}}(\mu_\Delta = 0, \sigma_\Delta = 0, dt) = \left(R^2 + T^2 - 2RT\right) \left(\exp\left[-\frac{WS}{\tau_l} \right] - \exp\left[-\frac{WE}{\tau_l} \right] \right)^2 \tag{3.22}$$

If we set the window start at its minimum possible value, $WS = 0$, and let $WE \to \infty$, so allowing for all detection times t_1 and t_2 we recover the coincidence probability of $(T - R)^2$ as predicted by Eq.(3.6).

If the two photons are perfectly distinguishable in their frequencies, we can also further evaluate this coincidence probability by setting $\sigma_\Delta \to \infty$ and $\mu_\Delta = 0$. This yields:

$$P_{\text{coinc}}(\mu_\Delta = 0, \sigma_\Delta \to \infty, dt) = \left(R^2 + T^2\right) \left(\exp\left[-\frac{WS}{\tau_l} \right] - \exp\left[-\frac{WE}{\tau_l} \right] \right)^2 \tag{3.23}$$

If we set the window start at its minimum possible value, $WS = 0$, and let $WE \to \infty$, so allowing for all detection times t_1 and t_2 we recover the coincidence probability of $R^2 + T^2$ as predicted by Eq. (3.2).

3.2 Single NV TPQI

Using an imbalanced interferometer sketched in Fig. 3.6, photons emitted by one NV center can be interfered on a beamsplitter (BS_2). To this end, the NV center must be excited two successive times. The emitted photons are directed by a beamsplitter (BS_1) into either the short arm, or the long arm. If in the first excitation round the emitted photon enters the long arm, and in the second excitation round the emitted photon enters the short arm, two photons will arrive at the second beamsplitter at the same time, provided that the delay between the two excitations is well calibrated with the length of the delay arm. This delay time will be referred to as T in the following. However, the probability to get a ZPL photon upon excitation of the NV center is small, and the probability to get two ZPL photons after two successive excitations is even smaller. Therefore, in an experiment the sequence of two excitations is repeated many times to gather statistics. Coincidence events are registered by the two photon detectors det_1 and det_2, and are defined as *a single detection in both detectors within one experimental sequence of two excitations.*

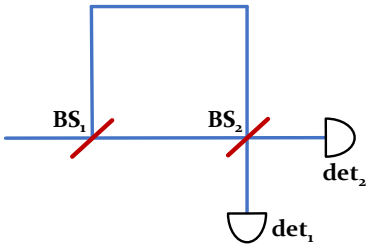

Figure 3.6: Sketch of the imbalanced interferometer with two beamsplitters and two detectors.

3.2.1 Photon Indistinguishability

A TPQI experiment can be used to measure the indistinguishability of photons. The probability to measure coincidences drops to 0 in the case of fully indistinguishable photons, and is non-zero for photons that are distinguishable to some degree. The contrast between the number of measured coincidences when the photons arrive at the same time at the beamsplitter, C_0, and the number of measured coincidences when the photons are fully distinguishable in arrival time, C_{dt}, is called the photon indistinguishability J, given as

$$J = 1 - \frac{C_0}{C_{dt}}. \tag{3.24}$$

This formula only provides knowledge about the photons itself if the TPQI setup is perfect, meaning no losses, equal beamsplitter splitting ratio's, and no noise- or dark counts. For an imperfect system, this contrast is referred to as the visibility V. It is expected that single photons emitted by a single NV center in the ZPL are highly indistinguishable, meaning a value of J close to 1.

3.2.2 Photon Counting Argument

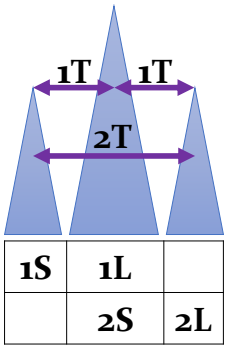

Figure 3.7: Photon counting argument

A repeated sequence of two excitations of the NV center will bring forth three peaks in the number of measured photon counts as a function of time, in both detectors. The earliest peak in photon detections is due to photons coming from the first excitation round of the NV center that travelled the short path (1S). The center peak in photon detections contains photons from both the first excitation that took the long arm (1L), and photons from the second excitation that took the short arm (2S). The latest peak in photon detections only contains photons from the second excitation round that took the long arm (2L). This is summarised in Fig. 3.7. Only in the center peak it is possible to get two photons at BS_2 at the same time. In an experiment, three detection time windows are selected, with a time spacing between them of $1T$.

Coincidence events can occur with either $0T$ detection time difference (center window), $1T$ detection time difference (early and center window, or center and late window), or $2T$ detection time difference (early and late window). For example, if a 1S photon is detected in detector 1, followed by a 2L photon detected in detector 2, then a coincidence event is registered with a detection time difference of $\tau = +2T$. The detection time difference τ is defined as positive if detector 1 clicked first, and negative if detector 2 clicked first.

-2T	-1T	0T	1T	2T
1S - 2L	1S - 2S	1L - 2S	1S - 2S	1S - 2L
	1L - 2L	1L - 2S	1L - 1L	

Table 3.1: All photon configurations that contribute to a coincidence count in one of the detection time difference bins $0T, \pm 1T$ and $\pm 2T$. In the detection time difference bins of $0T$ and $\pm 2T$, the photons enter the beamsplitter via distinct input ports. In the detection time difference bins of $\pm 1T$, the photons enter the beamsplitter in equal input ports. The colours emphasize which detector clicked first, green means detector 1 clicked first, red means detector 2 clicked first. Note that in the $0T$ detection time difference bin, the distinction is also made between the detection times in both detectors.

In Table 3.1, the different possibilities for coincidence counts are given as a function of the detection time difference. The detection time of the two detectors is binned in the three windows with the time spacing of $1T$, resulting in 5 binned detection time differences. The colors emphasize which detector clicked first; green means detector 1 clicked first, red means detector 2 clicked first. In the $0T$ detection time difference bin, the distinction is also made between positive or negative τ, assuming the detectors have a higher resolution than the binsize defining the windows.

For a detection time difference of $\tau = 0$ we would expect no coincidences in the case where our system would be perfect (50/50 splitting ratio's, no losses, no dark- or noise counts) and our photons fully indistinguishable. The expected ratio's of the five bins is therefore 1:2:0:2:1 for indistinguishable photons. For distinguishable photons, the expected ratio would be 1:2:2:2:1.

3.2.3 Dark- or Noise Counts

In a TPQI experiment, dark- or noise counts can also contribute to the coincidence counts. A dark count occurs when the detector accidentally 'clicks' while there actually was no photon present. A noise count occurs when stray light enters the set-up and is detected. In this analysis, both dark- and noise counts are treated as accidental clicks in the detectors. In the following, we therefore refer to both of them as dark counts. Coincidence events with dark counts can occur in two ways: either the combination of one dark count together with an NV photon, or the combination of two dark counts. As the probability to get a dark count is much smaller than the probability to get an NV photon upon excitation (by a factor in the order of $\sim 10^{-3}$), the possibility of two dark counts causing a coincidence can be safely neglected. The probability to get three or more clicks, due to for example two NV photons and one dark count, or two dark counts and one NV photon, is also neglected.

-2T	-1T	0T	1T	2T
1S - DC(3)	1S - DC(2)	1L - DC(2)	1S - DC(2)	1S - DC(3)
DC(1) - 2L	1L - DC(3)	2S - DC(2)	1L - DC(3)	DC(1) - 2L
	2S - DC(3)	1L - DC(2)	2S - DC(3)	
	DC(1) - 1L	2S - DC(2)	DC(1) - 1L	
	DC(1) - 2S		DC(1) - 2S	
	DC(2) - 2L		DC(2) - 2L	

Table 3.2: All configurations of one NV photon and one dark count that contribute to a coincidence event in one of the detection time difference bins $0T, \pm 1T$ and $\pm 2T$. The notation DC(i) means a dark count must be registered in time window number $i \in \{1,2,3\}$ corresponding to the selected detection time windows. The order of for example 1S - DC(3) means that first an NV photon is detected, followed by a dark count in window 3. The colours emphasize which detector clicked first, green means detector 1 clicked first, red means detector 2 clicked first.

For the possibility of one NV photon and one dark count causing a coincidence event (*ph-dc*), another photon counting argument must be made, but then for a single photon. To get a *ph-dc* coincidence contribution in the $0T$ bin, it is required that the emitted photon is detected in one detector, in either one of the three time windows, and the dark count is registered in the same window, in the other detector. Coincidence counts with $0T$ detection time difference in either window 1 or window 3 of Fig. 3.7 can only be due to at least one dark count. Therefore, these events are already filtered out in the experimental data set. In this dark count analysis, we only consider possible contributions of *ph-dc* coincidences

with $0T$ detection time difference that occurred in the center window. This means that the NV photon originates from either 1L or 2S. The NV photon must be detected in one detector, and then the dark count must be registered in the other detector. Either detector 1 clicks first, or detector 2 clicks first.

To get a *ph-dc* contribution with $+1T$ detection time difference, it is required that detector 1 clicks first. Either detector 1 registers a dark count first, or it detects a photon first. If the photon causes the first detection event, then it must be registered in either the early window or the center window, so it must originate from 1S, 1L or 2S (see also Fig. 3.7). The dark count must be registered one time window later, in detector 2. If the dark count causes the first detection event, the NV photon must be registered in detector 2 in either the center or the late time window, thus originating from 1L, 2S or 2L (see also Fig. 3.7). The dark count must be registered one time window earlier in detector 1.

To get a *ph-dc* contribution with $+2T$ detection time difference, it is again required that detector 1 clicks first. Either detector 1 registers a dark count first, or it detects a photon first. If the photon causes the first click, then it must be registered in the first time window, so originating from 1S. The dark count must be registered two time windows later, in detector 2, so in the third time window. If the dark count causes the first detection event, the NV photon must be registered in detector 2 in the third time window (2L). The dark count must be registered two time windows earlier in detector 1, so in the first time window.

A similar argument holds for the contributions of coincidences with dark counts in the $-1T$ and $-2T$ bins. The different configurations for each of the coincidence events with dark counts per detection time difference bin are summarised in Table. 3.2.

3.2.4 Introducing Imperfections

The single-NV TPQI set-up presented in Fig. 3.6 is not perfect. The following imperfections will have a direct consequence on the measured number of coincidence counts in each detection time difference bin:

- Imbalances in the first beamsplitter
- Imbalances in the second beamsplitter
- Finite polarisation extinction ratio's in the beamsplitters and optical fibers
- Photon losses throughout the set-up, due to insertion losses of the beamsplitters and transmission losses through the optical fibers
- Dark- or noise counts in the detectors

Therefore, we need to introduce a method to correct for the imperfections of our system such that we can extract the photon indistinguishability J from the measured number of coincidence counts per detection time difference bin. To this end, we define the parameters presented in Table 3.3 which can be extracted from the system. Using the time window length defined as $WL = WE - WS$, the number of experimental sequences of two excitations, N_{SYNCs}, and the parameters presented in Table 3.3, the following corrections can be performed:

1. Calculate the expected number of coincidence events caused by one noise- or dark count and one NV photon in each of the 5 bins. This is done using Table. 3.2 together with the dark count rates per detector, Γ_i, the used length of the time window, WL, the counts per shot per detector, CPS_i, and the number of experimental sequences of two excitations, N_{SYNCs}. This yields $P_j^{dc,ph}$ where $j = 0, \pm 1$ or ± 2, given as:

$$
\begin{aligned}
P_0^{dc,ph} &= N_{\text{SYNCs}} \cdot CPS_1 (P_L + P_S) \cdot \Gamma_2 WL + N_{\text{SYNCs}} \cdot \Gamma_1 WL \cdot CPS_2 (P_L + P_S) \\
P_{+1}^{dc,ph} &= N_{\text{SYNCs}} \cdot CPS_1 (P_S + P_L + P_S) \cdot \Gamma_2 WL + N_{\text{SYNCs}} \cdot \Gamma_1 WL \cdot CPS_2 (P_L + P_S + P_L) \\
P_{-1}^{dc,ph} &= N_{\text{SYNCs}} \cdot CPS_2 (P_S + P_L + P_S) \cdot \Gamma_1 WL + N_{\text{SYNCs}} \cdot \Gamma_2 WL \cdot CPS_1 (P_L + P_S + P_L) \\
P_{+2}^{dc,ph} &= N_{\text{SYNCs}} \cdot CPS_1 (P_S) \cdot \Gamma_2 WL + N_{\text{SYNCs}} \cdot \Gamma_1 WL \cdot CPS_2 (P_L) \\
P_{-2}^{dc,ph} &= N_{\text{SYNCs}} \cdot CPS_2 (P_S) \cdot \Gamma_1 WL + N_{\text{SYNCs}} \cdot \Gamma_2 WL \cdot CPS_1 (P_L)
\end{aligned}
\tag{3.25}
$$

Symbol	Meaning
C_0	measured number of coincidence counts in bin $0T$
C_{+1}	measured number of coincidence counts in bin $+1T$
C_{-1}	measured number of coincidence counts in bin $-1T$
C_{+2}	measured number of coincidence counts in bin $+2T$
C_{-2}	measured number of coincidence counts in bin $-2T$
P_S	probability photon passes through short arm
P_L	probability photon passes through long arm
R	reflectivity of second beamsplitter
T	transmissivity of second beamsplitter
FC	classical interference fringe contrast
Γ_1	dark count rate in detector 1
Γ_2	dark count rate in detector 2
CPS_1	average number of photons per excitation in detector 1
CPS_2	average number of photons per excitation in detector 2

Table 3.3: Parameters used for the correction of the imperfections in the system

This quantity can be interpreted as the expectation value to get a NV photon coincidence event with one dark count in each of the five bins. For each j, we define $P_j^{ph,ph} = C_j - P_j^{dc,ph}$. This quantity can be interpreted as the expectation value to get a photon-photon (*ph-ph*) coincidence event in each of the five bins. This step corrects for **noise contributions** in the set-up.

2. Re-scale the expectation value to get a photon-photon coincidence event to a situation of equal inputs at the second beamsplitter. For this, we use Table 3.1, and include the probability of each of the possible events represented in this table. The probability of *ph-ph* coincidence counts in the 0 bin is then given as $P_L P_S + P_L P_S$. The probability of *ph-ph* coincidence counts in the ± 1 bin is then given as $P_S P_S + P_L P_L$. The probability of *ph-ph* coincidence counts in the ± 2 bin is then given as $P_S P_L$. Re-scaling these probabilities to the 0 bin yields the factors 1 , $\frac{P_S^2+P_L^2}{2P_S P_L}$, and 1/2 for the 0, ± 1 and ± 2 bins, respectively.

$$\begin{aligned} \tilde{P}_0^{ph,ph} &= P_0^{ph,ph} \\ \tilde{P}_{\pm 1}^{ph,ph} &= P_{\pm 1}^{ph,ph} \cdot \frac{2P_S P_L}{P_S^2 + P_L^2} \\ \tilde{P}_{\pm 2}^{ph,ph} &= 2P_{\pm 2}^{ph,ph} \end{aligned} \tag{3.26}$$

This corrects for both the **imbalance in the first beamsplitter**, and for the **imbalance in loss in the two interferometer arms**, as a result of longer travelling distance in the long arm.

3. Calculate the equal-input, no noise, visibility using Eq. (3.24). Here, C_{dt} is taken as the average number of coincidences in the four non-zero detection time difference bins, assuming that the photons measured with either one or two pulse differences are fully distinguishable in arrival time.

$$V = 1 - \frac{\tilde{P}_0^{ph,ph}}{\frac{1}{4}\left(\tilde{P}_{+1}^{ph,ph} + \tilde{P}_{-1}^{ph,ph} + \tilde{P}_{+2}^{ph,ph} + \tilde{P}_{-2}^{ph,ph}\right)}. \tag{3.27}$$

4. Calculate the maximum attainable visibility as a result of imbalances in the second beamsplitter. To this end, we refer back to Eq. (3.22) where it was shown that the probability of a coincidence event if two fully indistinguishable photons impinge on different input ports at the second beamsplitter equals $P_{\text{coinc}}(\text{indist.})$. The probability of a coincidence event if two fully distinguishable photons impinge on different input ports at the second beamsplitter, $P_{\text{coinc}}(\text{dist.})$ is given by Eq. (3.23). This gives a maximum attainable visibility V_{max} of

$$V_{max} = 1 - \frac{P_{\text{coinc}}(\text{indist.})}{P_{\text{coinc}}(\text{dist.})} = 1 - \frac{(T-R)^2}{R^2+T^2} \tag{3.28}$$

5. Calculate the fringe contrast *corrected for imbalances in both beamsplitters.* The theoretical limit of the fringe contrast of an interferometer with imbalanced beamsplitter ratio's and imbalanced losses in the two arms, FC_{max}, is given as [24]:

$$FC_{max} = \frac{2}{\sqrt{\frac{P_S T}{P_L R}} + \sqrt{\frac{P_L R}{P_S T}}}. \tag{3.29}$$

   The corrected fringe contrast, FC_{corr} is then given as

$$FC_{corr} = \frac{FC}{FC_{max}} \tag{3.30}$$

   In this way, all other unknown system imperfections such as finite polarisation extinction ratio's are incorporated in this corrected fringe contrast.

6. Use the obtained correction factors to calculate the final photon indistinguishability as

$$J = \frac{V}{V_{max} \cdot FC_{corr}} \tag{3.31}$$

   Dividing by V_{max} corrects for **imbalances in the second beamsplitter**, and dividing by FC_{corr} corrects for possible **polarisation effects**.

3.2.5 Error Calculation

The final value of the photon indistinguishability J is calculated using the steps presented in the previous section (3.2.4). To calculate the standard deviation of the photon indistinguishability J, we need the standard deviations of all the parameters in Table 3.3. Next, a method to propagate these standard deviations into the photon indistinguishability is required.

Standard Deviation of parameters

The parameters $P_S, P_L, R, T, FC, \Gamma_1, \Gamma_2, CPS_1$ and CPS_2 vary over the duration of the experiment. For applying the corrections, the mean value over time is used, μ. The instantaneous value cannot be used as the number of coincidence counts in the 5 bins is built up over the course of the whole experiment. In the error propagation, the standard deviation of the instances of the parameter over time is used, σ. It is assumed that these parameters are then Gaussian distributed with a probability density function given as

$$f(x) = \frac{1}{\sigma\sqrt{2\pi}} \exp\left[-\frac{1}{2}\left(\frac{x-\mu}{\sigma}\right)^2\right] \tag{3.32}$$

for $-\infty < x < \infty$. [30]

The standard deviation of the parameters $C_0, C_{\pm1}, C_{\pm2}$ are the square roots of the values itself due to the underlying Poissonian statistics of single photon detection. Single photon detection involves the counting of independent, random events, measured over a long period of time at a constant rate. The number of photons measured, X, has a Poisson distribution with parameter $\lambda > 0$, with a probability mass function P given as

$$P(X = k) = \frac{\lambda^k}{k!} \exp(-\lambda), \tag{3.33}$$

where $k = 0, 1, 2, ...$ is the number of occurrences [30]. The mean and variance of a Poisson distribution are both equal to the parameter λ. The standard deviation thus equals $\sqrt{\lambda}$.

Monte-Carlo error propagation

For propagation of the errors of all the parameters in Table 3.3 into the photon indistinguishability J, the method of Monte-Carlo error propagation is applied. To this end, we first sample N random quantities of each of the parameters $P_j^{ph,ph} = C_j - P_j^{dc,ph}$, defined in step 1 of the correction method, of a Poissonian distribution, with $\lambda = P_j^{ph,ph}$ where $j = 0, \pm1$ or ±2. We assume that the quantities $P_j^{ph,ph}$ are Poissonian distributed as the error contribution due to the Poissonian nature of the measured coincidence counts C_j is leading over the much smaller Gaussian error in $P_j^{dc,ph}$ introduced by the error in the CPS values and Γ values. For each of the parameters $P_S, P_L, R, T,$ and FC, we take N random samples from a Gaussian distribution with μ corresponding to the mean value of the parameter over time and σ corresponding to the standard deviation of the instances of the parameter over time.

For each $n \in N$, we then calculate the corresponding photon indistinguishability J_n according to the steps 2-6 presented in Section 3.2.4, resulting in the array $\mathbf{J} = [J_0, J_1, ..., J_n, ..., J_N]$ of length N. Next, we make a histogram of this array $\mathbf{J}$, normalised such that the integral over the full range is 1. The next step is determining the bounds of the confidence interval. Given a confidence interval of size I, we integrate the histogram of the array $\mathbf{J}$ from the value of the determined photon indistinguishability J to the right until this integral equals $I/2$. The instance of $\mathbf{J}$ at this limit is the right bound, r. Similarly, we integrate the histogram of the array $\mathbf{J}$ from the value of J to the left until this integral equals $I/2$. The instance of $\mathbf{J}$ at this limit is the left bound, l. Then the value of the photon indistinguishability J with error is reported as J in interval $[l, r]$ with I% confidence.

For large λ, the Poisson distribution given in Eq. (3.33) can be approximated by a Gaussian distribution with $\mu = \lambda$ and $\sigma = \sqrt{\lambda}$. Therefore, for higher photon detection numbers, the histogram of the array $\mathbf{J}$ will be approximately Gaussian as all input parameters can then be approximated by Gaussian distributions. The histogram of $\mathbf{J}$ will be symmetric around the mean. For lower photon detection numbers, the histogram is a combination of a Poissonian and a Gaussian curve, and it will be asymmetric around the mean. This will then also result in an asymmetric confidence interval.

Chapter 4

Experimental Set-Up

In this chapter, the experimental set-up used to excite and control a single NV center, and to collect its photon emission, is described. The full experimental set-up, which will be used for future 2 NV experiments, consists of two nodes, both being able to excite, control, and collect emission from the NV center located in their diamond sample. In this thesis, experiments were only done using one of the two nodes, also referred to as Node 1. Next, the set-up used for the single NV TPQI experiments presented in Chapter 5 is described, as well as the applied measurement sequence.

4.1 Sample Fabrication

Single NV centers occur naturally in chemical-vapor deposition grown type IIa diamonds of high purity, which are grown along the (100) crystalline orientation and subsequently cleaved to obtain a (111) orientation [4]. It is shown that the NV centers in samples with this surface orientation are oriented with a ~ 97% probability along the [111] axis [31], which is the preferential alignment for a high photon collection efficiency as the emission of the NV center is then perpendicular to the air-diamond interface. In order to improve the photon collection efficiency even further, a hemispherical solid immersion lens (SIL) is fabricated around the NV center by milling away diamond in a focused ion beam. The size of the SIL is determined depending on the depth the NV center, which is selected in the range of 5-15 µm below the surface of the diamond [11]. This SIL reduces unwanted refraction and total internal reflection processes. A 200 nm thick gold microwave stripline is fabricated on top of the sample surface to deliver magnetic resonance pulses, used for Bloch sphere rotations. Gold gates are fabricated as well for applying DC voltages to be able to shift optical transition frequencies via the DC Stark effect. The fabrication of both the stripline and gates is done via electron beam lithography [11]. As a final main step in the production process, an anti-reflection coating (aluminium oxide) is applied on top of the diamond surface via atomic layer deposition to further enhance the collection efficiency. The diamond sample of

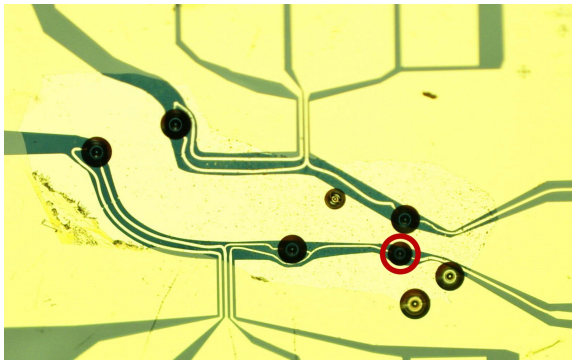

Figure 4.1: The diamond sample of Node 1. The circles are solid immersion lenses, milled into the diamond (green) at locations where NV centers are present. The yellow areas are gold layers. The SIL with NV center used in experiments is marked with a red circle.

Node 1 is shown in Fig. 4.1. There are multiple NV centers in this sample, the brightest NV with the right orientation is selected for experiments, being the one that is marked with a red circle.

4.2 Node 1

As explained in Chapter 2, the diamond sample must be cooled to cryogenic temperatures to allow for selective excitation of the SP and RO transitions. The sample is therefore placed on a cold finger and put inside a cryostat. A permanent magnet is mounted right behind the sample to split the energy levels of the $m_s = \pm 1$ states. Microwaves used for Bloch sphere rotations can be applied by sending electronic signals, generated and amplified by a microwave source, through the stripline, which is bonded with electrical wires that exit the cryostat. The cryostat is pumped to low pressure and cooled to a temperature around 4 K using helium. The optical connection to one specific NV center in the sample is made using an objective lens with stages to control the position of this lens. This objective is part of the cryostat chamber as well. A glass window closes the cryostat chamber while still allowing for an optical connection between the objective to the free space optics on the optical table.

4.2.1 Optical Addressing

Optical pulses from different lasers are used to control the state of the NV center, being the readout (RO) laser, that excites one of the two $m_s = 0 \Leftrightarrow E_{x/y}$ transitions, the spinpump (SP) laser, that excites both $m_s = \pm 1$ ground states to one of the $E_{1/2}/A_{1/2}$ transitions, and a repump laser of 532 nm (green) that can bring back an ionised NV to the negatively charged NV center [1]. The pulsing and power control of the continuous wave laser light of all lasers is done via acousto-optical modulators (AOM), which can quickly open and close an optical path, in the order of 100 ns. In addition to the AOMs, an electro-optical modulator (EOM) is included in the readout path to allow for even faster optical pulses with sharp rising and falling edges, in the order of 2 ns. The AOMs and EOMs are controlled by both an arbitrary waveform generator (AWG) and an integrated micro-controller (ADwin). The ADwin functions as trigger to let the AWG know when sequences must be played, and the AWG notifies the ADwin when the sequences are completed. In this way, the timing of optical pulses can be precisely controlled. The frequencies of the lasers are monitored and controlled. All single photon detectors used in experiments are connected to time-taggers, which is a device that can tag the detection of a single photon to a specific time. A so-called SYNC pulse sent out by the AWG resets the clock of the time-tagger. An experimental sequence always starts with such a SYNC pulse, to inform the time-tagger that it should start counting from 0 again. In this way, time in experiments is always with respect to the SYNC pulse. To synchronize the timing between the two nodes and the midpoint station in future two node experiments, a time distribution system is used. See also the diagram of the communication between the control and measurement equipment in Fig. 4.2. The laser light of the different lasers enters the free-space optics of the set-up. A combination of half-wave plates, quarter-wave plates and polarisers ensures that the laser light arrives in the right polarisation. By using tunable mirrors, the laser paths are aligned through the objective to overlap in focus on the sample.

4.2.2 Collecting NV Emission

The single photons emitted by the NV center must be collected and coupled to fibers connecting to avalanche photon detectors (APD). The photons are separated into the phonon side band (PSB) and the zero-phonon line (ZPL) by using a dichroic mirror (DM), that has different reflection coefficients for different wavelengths. The photons in the PSB are directly coupled in fiber towards the APD, and are used in the experiments in this thesis for charge-resonance checks and the readout of the electron spin. The photons in the ZPL pass through three different waveplates and are filtered in polarisation and frequency using a polarising beamsplitter, an angle tunable filter and a polarising band pass [10]. This filtering process ensures that all ZPL photons have identical frequency and polarisation.

The frequency of the emitted ZPL photons of the NV center is the same as the frequency of the RO laser that is used to excite the transition. The reflections of the RO light from the sample must be filtered from the NV photons as this light does not have a single-photon nature and can therefore not be used

[1] Repumping can also be done using a 575 nm (yellow) laser.

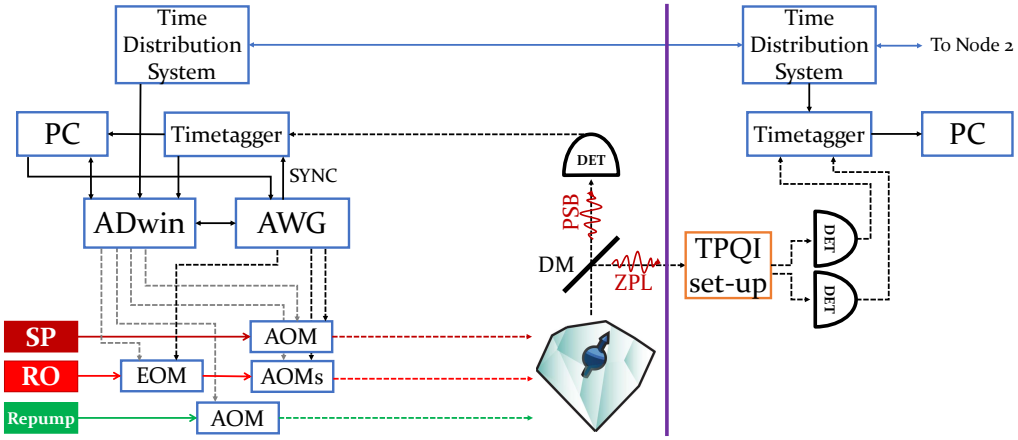

Figure 4.2: A simplified schematic describing the communication between the control and measurement equipment of Node 1, and the Midpoint station (separated by the purple vertical line). The measurement PC is used to run measurement scripts and store and analyse the gathered data. It also programs the control loop on the ADwin and pulse sequences on the AWG. Sequences on the AWG are triggered by the ADwin. Both the AWG and ADwin generate laser pulses via the AOMs from the continuous wave SP and RO lasers. The AOM of the green repump laser is only controlled by the ADwin. An extra EOM in the readout path allows for short optical excitations. A dichroic mirror (DM) separates the PSB and ZPL photons. The PSB photons are collected by the APD, and time-tagged using the time-tagger in combination with the counting module of the ADwin. A SYNC pulse sent out by the AWG resets the time of the time-tagger. The ZPL photons can enter the TPQI set-up, where the two detectors are connected to a time-tagger situated at the Midpoint. The Time Distribution System gives the SYNC pulse for the time-tagger at the midpoint.

in two-photon quantum interference experiments. The filtering of the reflections of the RO light is done by a method called cross-polarisation rejection, which will be explained in the next paragraph.

Cross-polarisation rejection

The two excited states of the $m_s = 0$ state are the E_x and E_y state. When the NV center is excited resonantly by a linearly polarised RO laser pulse, the relaxation to the ground state happens with the emission of a photon that is also linearly polarised. Either the $m_s = 0 \Leftrightarrow E_x$ or the $m_s = 0 \Leftrightarrow E_y$ transition is chosen, depending on which excited state has an energy level that is furthest away from the energy levels of the excited states of the $m_s = \pm 1$ states. This is dependent on the specific NV center that is used. In the following, we refer to the $m_s = 0$ state as $|\uparrow\rangle$, the E_x state as $|E_x\rangle$ and the E_y state as $|E_y\rangle$. The state $|E_x\rangle$ is orthogonal to the state $|E_y\rangle$. The most successful excitation occurs when the excitation light has the exact same polarisation as one of the chosen $E_{x,y}$ transitions. Then, however, it is not possible to filter the laser light from the NV photons by a polarisation method. Therefore, a concession must be made. The linearly polarised excitation light is rotated using a half-wave plate to an angle ϕ with respect to one of the chosen $|E_x\rangle$ or $|E_y\rangle$ states. The amount of coupling of the excitation light is then given as $\cos\phi$. In Fig. 4.3 , the principle of cross-polarisation rejection is depicted.

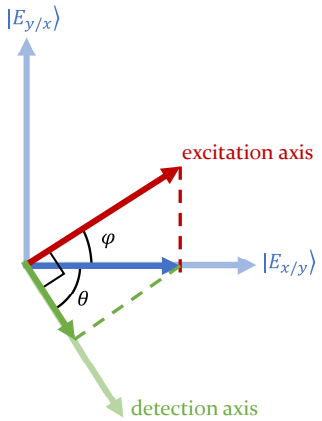

Figure 4.3: The principle of cross-polarisation rejection. Figure adapted from [19].

The best filtering in polarisation between the excitation light and the emitted photons can occur if the polarisations of these two are orthogonal. Therefore, not only the excitation axis is rotated away from the ideal coupling, but the polarisation of the detected axis is also rotated away from the ideal coupling. In the detection path, the combination of another half-wave plate and a polariser defines a detection axis, which is rotated to an angle θ with respect to one of the chosen $|E_x\rangle$ or $|E_y\rangle$ states. This angle θ is such that the detection axis is orthogonal to the excitation axis, meaning $\phi + \theta = 90°$. Now that the excitation light is orthogonal to the emitted light,

these two can be separated by using a polarising beamsplitter. The optimum in both the rejection from the laser light, the excitation efficiency of the NV and the collection efficiency of the NV is reached by varying the two angles θ and ϕ while keeping the sum of the two equal to 90°. An additional quarter wave plate is placed in the detection path as well to correct for possible circular polarisation components that are introduced by non-ideal optical elements. Finally, the free-space light is coupled in-fiber.

Using the Zero-Phonon Line

The optical fiber containing the zero-phonon line photons can be directly connected to an APD, to for example calibrate the RO excitation pulse that generates ZPL photons. It can also be used as input to the imbalanced interferometer of the single NV TPQI setup, which will be explained in Section 4.3.

For future 2-node experiments with down-converted photons (not performed in this thesis), the zero-phonon lines of both of the nodes are connected to two quantum frequency converters (QFC). As explained in Chapter 2, the QFC converts the frequency of the input photons from 637 nm to the telecom wavelength of 1588 nm using a pump laser at 1064 nm. To filter out noise produced in the down-conversion process, a narrow (50 MHz bandwidth) Fibre Bragg Grating is introduced around the target wavelength. The shape of the filter in the frequency domain is a Lorentzian. See also the schematic of a 2-node setup in Fig. 4.4.

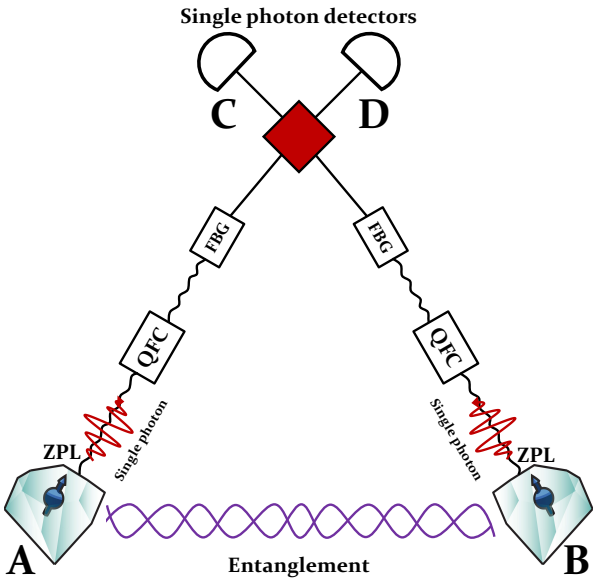

Figure 4.4: Schematic representation of the set-up which will be used in future experiments (**not performed in this thesis**) to generate entanglement between NV centers A and B using down-converted photons, converted by the QFC, and filtered by the FBG.

Using a feedback loop, the position of the two filters is kept at the right place in the frequency domain to ensure maximal transmission of the down-converted photons. By small modifications of the pump laser frequency at both nodes, the frequencies of the converted photons can be tuned to the exact same value. The front to end conversion efficiency of Node 1 is approximately 51 %, and of Node 2 approximately 47 %. The filtering process introduces extra losses; its efficiency for both nodes is estimated to be 10 %.

For the entanglement generation schemes explained in Chapter 2, the converted photons of both nodes are overlapped on a beamsplitter (Evanescent Optics), with a reflectivity of $R = 0.494$ and a transmissivity $T = 0.506$. At the output ports C, D of the beamsplitter, two superconducting nanowire single photon detectors (SNSPD) will detect the photons, with detection efficiencies of around 60 %. The two FBGs, the beamsplitter and the SNSPDs are located at a midpoint station. None of the equipment of the two nodes or the midpoint station is shared, which allows for large distance separation for future experiments. Only telecom optical fibers and classical communication fibers connect the two nodes with the midpoint.

4.3 Single NV TPQI

4.3.1 Set-Up

The set-up used for the single NV TPQI experiments described in the next chapter is built on a breadboard such that it is easily portable, and can also be used to measure self-interference on other NV centers. It consists of a 1:2 beamsplitter (BS_1), which in the ideal case is balanced, a delay arm of 30 m, a 2:2 beamsplitter (BS_2) which is in the ideal case also balanced, and two APDs. See also the schematic representation in Fig. 4.5. The fibers are all polarisation maintaining. The two beamsplitters (Thorlabs) are both specified to have a polarisation extinction ratio of above 22 dB. The two detectors (Laser Components) have specified detection efficiencies of 69 % and 75 %, for detector 1 and 2, respectively.

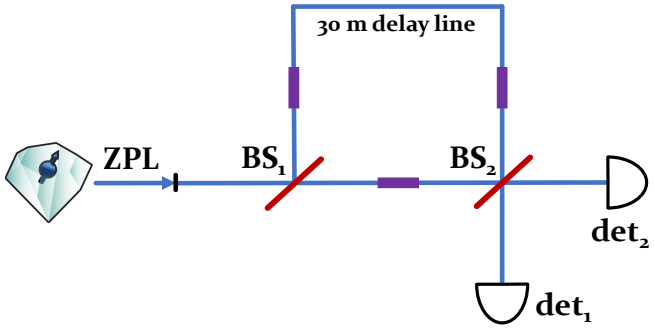

Figure 4.5: Schematic representation of the single NV TPQI setup used in experiments, with a ~30 m delay line. It requires input from the ZPL, which is connected to the interferometer with a connector piece (in black). The locations of the splices are indicated in purple.

Optical fibers are in general terminated by a fiber tip that can easily catch dirt or get scratched. When connecting two polarisation maintaining fibers, a connector piece has to be used to align the fiber cores and match the polarisation axes. This connection introduces extra losses (in the order of 1 dB per connection), and can introduce non-ideal alignment of the polarisation axes. To mitigate the losses and low polarisation extinction ratios caused by the fiber connectors, it was decided to splice the connection from the first beamsplitter to the second beamsplitter (the short arm), and the two connections from the delay arm to the two beamsplitters. Another advantage of this splicing is that the fibers cannot catch dirt anymore. Splicing two fiber ends means to melt two bare fibers together using a localised heat source. The typical insertion loss of a spliced connection is below 0.1 dB. The polarisation extinction ratio of a spliced connection is above 30 dB. A disadvantage of splicing is that the connection is made permanent. The total losses introduced by the single NV TPQI set-up are in the order of 2 dB.

The single NV TPQI set-up only requires input of the ZPL from the full node set-up, and a connection of the two detectors to a time-tagger.

4.3.2 Measurement Sequence

For two-photon quantum interference to occur, two indistinguishable single photons must be present. As explained in Chapter 2, the NV center can generate photons with the same frequency and polarisation in the ZPL. To generate precisely one photon, a very short (<2 ns) excitation pulse resonant with the $m_s = 0 \Leftrightarrow E_{x/y}$ transition is applied. This pulse, callend an optical pi pulse, is calibrated in power such that the transition is precisely saturated. As the probability that a single optical pi pulse actually results in a ZPL photon detection is small (in the order of 0.1 %), sequences of optical pi pulses must be repeated many times to gather statistics.

The extra travel time of photons in the long arm with respect to the short arm is determined by a repeated sequence of a single optical pi pulse. This sequence will yield two peaks as a function of time in the measured number of counts in the two detectors. The time difference between the two maxima is then determined, yielding a delay time of $T = 142.0 \pm 0.4$ ns.

For the single NV TPQI experiment, two optical pi pulses with a delay of T are sent out after a SYNC pulse. Every 5 blocks of 2 optical pi pulses, a spinpump pulse of 1.5 µs is sent out to reinitialise in the $m_s = 0$ state. The sequence of these $5 \cdot 2$ optical pi pulses in combination with the SP pulse is repeated a

total of 108 times. A period of charge-resonance (CR) checks takes place after this block. The sequence of the repeated SP, optical pi pulses and CR checks is repeated 40000 times. This constitutes one measurement repetition. Every 12 measurement repetitions, a period of automated calibrations will take place. During this period, the classical fringe contrast is determined by moving the objective focus to the stripline of the sample, and using reflected readout laser light. Next, the position of the objective is re-optimized on the NV center. The readout and spinpump lasers are re-calibrated in power. The amount of maximum readout power available is measured, and then it is determined if this value is still enough to saturate the $m_s = 0 \Leftrightarrow E_{x/y}$ transition. The measurement sequence is shown in Fig. 4.6.

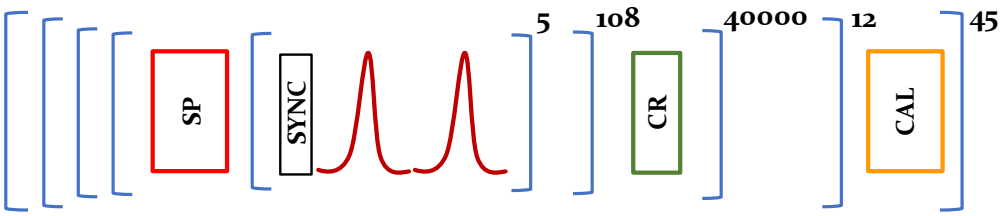

Figure 4.6: Schematic representation of the applied measurement sequence. After a SYNC pulse that resets the measurement time of the detectors to 0, two optical pi pulses, in dark red, are sent out. This is repeated 5 times. A spin-pump (SP) pulse of 1.5 µs, in bright red, re-initialises in the $m_s = 0$ state. This is repeated 108 times, after which a period of charge-resonance (CR) checks takes place, in green. This sequence is repeated 40000 times, constituting one measurement repetition. Every 12 measurement repetitions, a period of calibrations ('CAL', yellow) takes place. In total 45 of such sequences were carried out, yielding 540 measurement repetitions.

The experiment was originally planned to execute 1200 measurement repetitions. However, after 540 repetitions, corresponding to a measurement time of ~12 h, the maximum available power of the RO laser had drifted below the threshold needed for saturating the $m_s = 0 \Leftrightarrow E_{x,y}$ transition, and the measurement was aborted. The total number of sent out optical pi pulses therefore amounts to $45 \cdot 12 \cdot 40000 \cdot 108 \cdot 5 \cdot 2 = 23.3$ billion.

Chapter 5

Results and Discussion

5.1 NV Calibrations

For the single NV TPQI experiment, the NV center of Node 1 is used as a single photon emitter. To be able to precisely excite the readout transition such that the NV emits a single photon into the ZPL, several calibrations must be performed. First, the readout, spinpump and green lasers are calibrated in power. Next, the focus of the objective is optimized on the NV center by performing line scans. If the objective is focused well, a continuous green laser power in the order of 30 µW excites the NV center off-resonantly resulting in many emitted photons into both the PSB and ZPL. If this measurement is done for a range of xyz-coordinates, the location of the NV center shows up as a peak in the measured counts in the PSB. After the laser power calibration and the objective focus optimisation, a charge resonance (CR) check measurement is done, followed by a single-shot readout. Finally, the optical pi pulse that will excite the right transition of the NV center is calibrated.

5.1.1 CR Checks

During a CR check measurement it is checked if the NV center is in the right charge state (NV^-) and if the lasers are on resonance with the chosen transition. The switching between the desired negative charge state and the neutral charge state can be caused by a two-photon absorption process [13]. The optical transitions of the NV center fluctuate due to small changes in the strain or the electric field of the environment, requiring the lasers to follow these drifts for optimal addressing. To this end, both the readout and the spinpump transition of the NV center are excited simultaneously, causing a steady-state situation where there is population in both spin states of the NV center. Decay from both of these states results in emission of PSB and ZPL photons. The counts in the PSB are measured during this short (~ 50 µs) excitation period. If the number of detected counts exceeds a certain threshold, the CR check is labelled a success and the experiment can continue. Then the two lasers are on resonance with the right transitions. If the number of detected counts is below the threshold, this step is repeated until either a success, or when the number of repetitions exceeds a next threshold. Then the NV center is expected to be in the unwanted charge state (NV^0). An off-resonant strong green laser pulse that resets the full charge environment of the NV center can be used as repump pulse to bring back the NV to the negative charge state.

5.1.2 Single-shot Read Out

The calibration of the readout of the electron spin state is a good way to check if both the readout and the spinpump lasers are on resonance with the transitions of the NV center, as it is a measurement that is highly sensitive to off-resonance of the laser frequencies. Here, the fidelity of the readout of the $m_s = 0$ and the $m_s = \pm 1$ is determined separately. To determine the $m_s = 0$ readout fidelity, the spin state is initialised by cycling the spinpump transition for 250 µs (see also the dark red dashed line in Fig. 2.3) and subsequently read out by applying a readout laser pulse of varying duration. The readout is successful if a photon is detected in the PSB. To determine the $m_s = \pm 1$ readout fidelity, the spin state is initialised by applying a readout laser pulse for 250 µs (see also the bright red dashed line in Fig. 2.3)

and subsequently read out by applying a readout laser pulse of varying duration. Now the readout is successful if no photons are detected. Both processes are done repetitively 5000 times to average the data points. The results of a readout where both lasers were on resonance with the transitions of the NV center are presented in Fig. 5.1. Here, the readout fidelity of both spin states is plotted as a function of the duration of the readout laser pulse. The mean of the two fidelities is taken for each duration of the

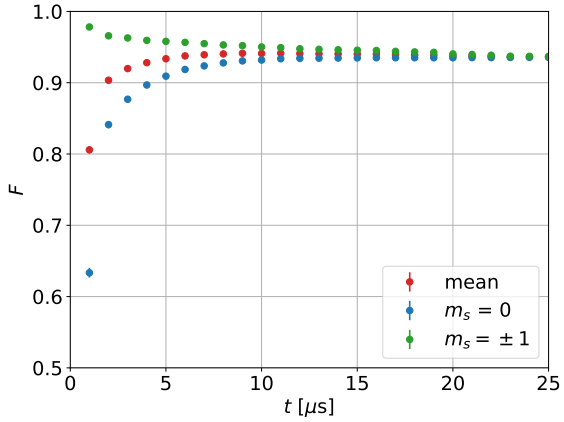

Figure 5.1: Single-shot readout, showing the fidelity versus the readout pulse duration in µs. Green datapoints are the fidelity for the $m_s = \pm 1$ state, blue datapoints are the fidelity for the $m_s = 0$ state. Red datapoints are the average of those two. The maximum average fidelity $F = 94.67 \pm 0.30$ % for a readout duration t = 8 µs.

readout laser pulse. This overall fidelity F is maximal, 94.67 ± 0.30 %, when the readout duration t is 8 µs.

If, for example, the spinpump laser was off-resonance, this would result in a bad initialisation into the $m_s = 0$ state, resulting in less photon detection after the readout laser pulse of varying duration. So a lower fidelity of the $m_s = 0$ state can indicate off-resonance of the SP laser. On the other hand, if the readout laser was off-resonance, then the initialisation of the $m_s = \pm 1$ state would be poor. It is possible that now more photons are detected, resulting in a lower fidelity of the $m_s = \pm 1$ state. However, as the readout laser pulse of varying duration will not excite the readout transition, the number of measured counts of the $m_s = 0$ state will be low, also resulting in a lower fidelity of the $m_s = 0$ state.

In the single NV TPQI experiment, the single-shot readout measurement is mainly used as a tool to confirm if the spinpump and readout laser are on resonance with the right NV transitions. In other experiments, such as a spin-photon correlation experiment, this determination of the non-perfect readout fidelity can be used to apply corrections on data, showing the results in the hypothetical case that the readout had been perfect.

5.1.3 Optical Pi Pulse Calibration

To be able to generate single ZPL photons, the $m_s = 0 \Leftrightarrow E_{x/y}$ transition, indicated by the bright red line in Fig. 2.3, must be saturated. This is done an optical pi pulse, which is a short (≤ 2 ns) pulse of readout light of a certain calibrated power. The calibration of this pulse consists of 2 main steps. The first is calibrating the voltage levels the AWG must apply on both the AOM and EOM as a function of time, such that the light path of the RO laser is opened for a very short instance. The second is the calibration of the readout power to precisely saturate the transition.

AOM and EOM voltage levels and time calibration

The AOM is used to open and close the light paths coming from the continuous wave RO laser. It can close a light path with an extinction level of more than 50 dB. The standard setting of the AOMs used in all the laser paths is such that the light paths are closed. The opening and right thereafter closing again of an AOM takes in the order of ~ 100 ns. The set voltage level on the AOM controls how much the device opens the light path. Therefore, the voltage level determines the amount of laser power that is let through. The timing of the applied voltage to open the AOM determines when in time the light path is opened, thus determining the timing of the light pulse.

To be able to generate a very short readout laser light pulse, an extra EOM is included in the readout laser path. It has a lower extinction ratio than the AOM, in the order of 30 dB. The standard configuration of the EOM is that it is always open, so without a voltage bias (0 V). A positive (or negative) constant voltage level of ~0.5 V makes the EOM closes the light path. If the voltage level is pulsed from a negative level to a positive level as fast as possible, the EOM briefly opens the light path during the short time that the voltage level crosses the 0 V line. The voltage level before and after the opening is set to the same, but opposite level, to avoid charging effects. The time of the opening of the EOM is calibrated such that it happens on the falling edge of the AOM, meaning that when the AOM starts to close the light path, the EOM briefly opens the light path. The timing of the opening of the EOM is therefore always calibrated with respect to the timing of opening of the AOM. The duration of the positive or negative

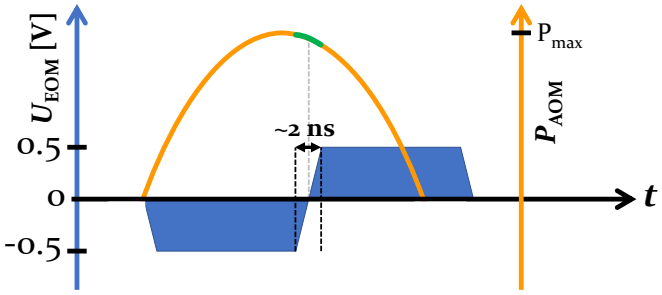

Figure 5.2: A schematic representation of the voltage levels U applied to the EOM (blue, left axis) as a function of time, overlaid with the optical power passing through due to the opening of the AOM, P_{AOM} (orange, right axis). Only in the short period of ~ 2 ns, indicated in green, the EOM opens the light path, thus allowing the RO light to pass to excite the NV center. The RO light is suppressed by the EOM at all other times when the AOM is open.

voltage level of the EOM right before and right after the short pulse must be such that all pulse light due to the opening of the AOM is suppressed. This prevents reflected laser light from interfering with the NV photon signal. Therefore, the minimum duration of one optical pi pulse is the time it takes for the AOM to open and close again. A schematic representation of the timings of the applied voltage levels to the EOM with respect to when the AOM is open is included in Fig. 5.2.

Readout power calibration

The calibration of the amount of power needed to saturate the transition is done by sweeping the AOM voltage level, resulting in different readout powers. In Fig. 5.3, the counts per shot (CPS) in both the PSB and ZPL are plotted as a function of the readout power. The counts per shot is defined as the probability that one optical pi pulse generates an NV photon that is also detected. The window start and end are calibrated to a time of 38 ns and 72 ns after the SYNC pulse, respectively. There can be seen that at a readout power around 17 µW the transition is saturated, resulting in the highest counts per shot value.

Now that the readout power and the AOM and EOM settings have been calibrated, a repeated sequence of optical pi pulses is sent out, and the counts in the PSB and ZPL are recorded and time-tagged. The histogram of the number of counts as a function of time after the SYNC pulse in the ZPL is shown in Fig. 5.4. The exponential decay from the NV center is visible as a straight line in the semi-log scale. A background measurement is done as well to see how much reflected pulse light still leaks through the set-up, after the application of the cross-polarisation rejection scheme explained in Chapter 4. This is done by deliberately changing the frequency of the readout laser, such that the NV center is not excited, and will not emit photons in the ZPL. The only photons counts that are recorded with an optical pi pulse with light of the wrong frequency originate from the reflected pulse light. Selecting the start of the signal window after the peak of the reflected pulse light is an additional method to filter residual reflected resonant excitation light from the NV photons.

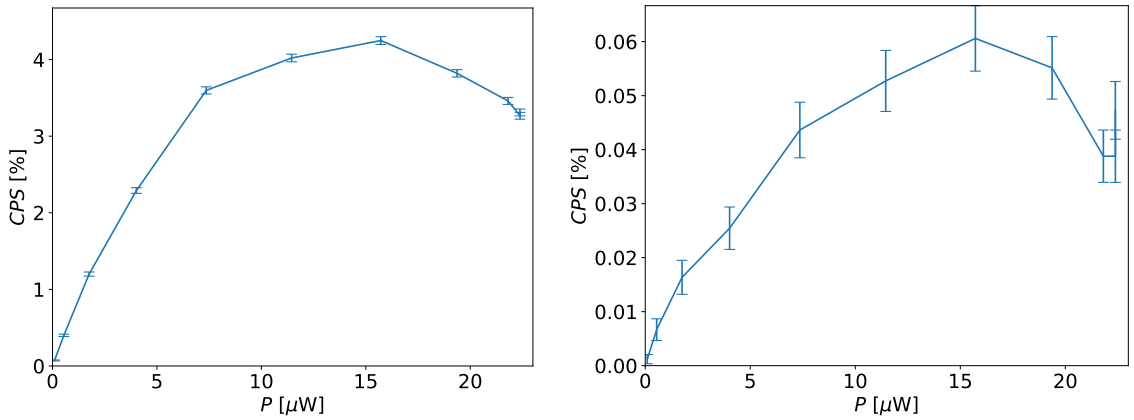

(a) Counts per shot in the **PSB** as a function of readout power in μW, using a time window of 38-72 ns after the SYNC pulse.

(b) Counts per shot in the **ZPL** as a function of readout power in μW, using a time window of 38-72 ns after the SYNC pulse. .

Figure 5.3: PSB and ZPL counts per excitation as a function of the readout power. Errorbars represent one standard deviation. Around P =17 μW, the transition is saturated.

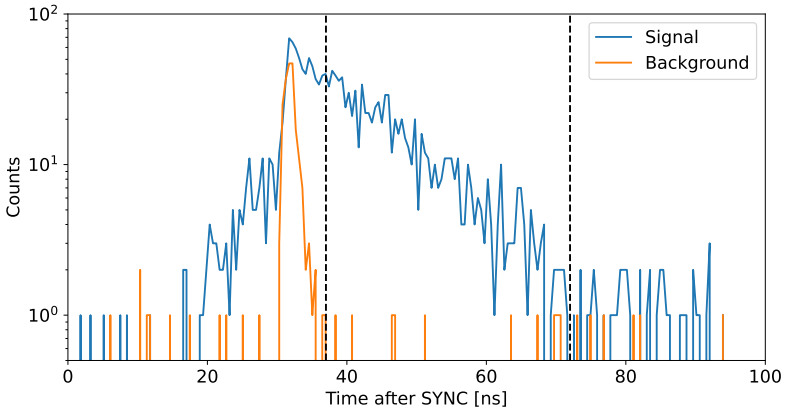

Figure 5.4: Histogram of measured counts in the ZPL as a function of time after the sync, using a binsize of 0.5 ns. The signal as a result of resonant excitation is plotted in blue, the background as a result of off-resonant excitation is plotted in orange. The selected time window is indicated by the black vertical lines.

5.2 Single NV TPQI experiment

5.2.1 CR Checks during Experiment

As shown in the schematic of the measurement sequence in Fig. 4.6, every sequence of 540 SYNCs is followed by a block of charge-resonance checks. The measured number of counts in the very last CR check after such a sequence is labelled as 'CR before' as it indicates how well the lasers are on resonance right before a next experimental sequence. The measured number of counts in the very first CR check after such a sequence is labelled as 'CR after', as this number can indicate if a NV ionisation process took place during the previous experimental sequence. A histogram of the two quantities 'CR before' and 'CR after' is made over the course of the full experiment, using a binsize of 5 counts, see also Fig. 5.5. The number of counts right after an experimental sequence is on average lower than right before a sequence due to the small drifts over time in the frequencies of the NV transitions as well as small drifts in laser frequencies. In approximately 6% of the datasets, ionisation took place resulting in a measured 0 number of counts right after the experimental sequence. Ideally, these datasets need to be filtered out as it is not possible to generate indistinguishable photons with an ionised charge state. This can be done by setting a threshold on the number 'CR after'. If the measured number of counts is lower than this threshold, then all the data of the previous 540 SYNCs is labelled as ionised and needs to be removed.
Unfortunately, a small error occurred in data taking. The time-tagger did not register the sent out num-

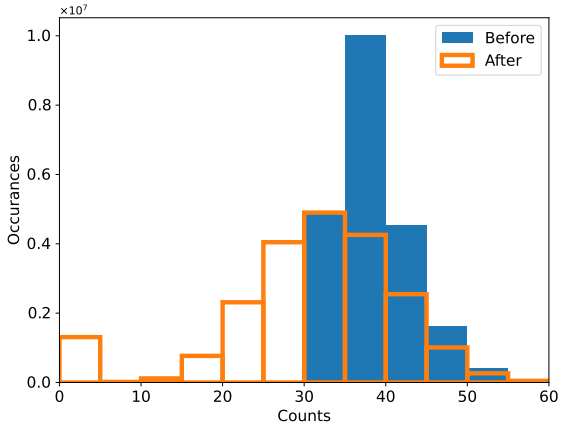

Figure 5.5: A histogram of the number of measured counts in the very last CR check after an experimental sequence (CR before) in blue and the number of measured counts in the very first CR check (CR after) in orange. The binsize is 5 counts. Ionisation took place in ~ 6 % of the datasets.

ber of $540 \cdot 40000$ SYNCs per measurement repetition, but a varying multiple of 540 SYNCs less. The CR check dataset is complete. Therefore, the mapping between the CR check dataset and the time-tagger dataset is not one-to-one, and it is not possible to discard the datasets labelled as ionised.

5.2.2 Laser Power Calibration during Experiment

Every 12 measurement repetitions, it is checked if the set laser powers of the spinpump and readout laser still agree with the measured laser powers. If this calibration is off, the laser power will be re-calibrated. This ensures that the readout power required to saturate the transition for the generation of ZPL photons can actually be set to that precise value.

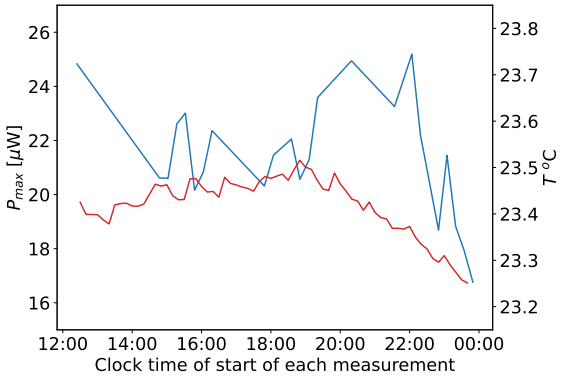

Figure 5.6: Maximum available readout laser power in μW, left axis, and the temperature of the optical table of Node 1 in °C, right axis, as a function of the clock time at the start of each measurement. At 23:45, the maximum available readout power had drifted to below the threshold of 17 μW required for an optical pi pulse. Therefore the measurement was aborted.

In Fig. 5.6, the maximum available readout power is plotted as a function of the measurement time. This power fluctuates a lot, and at the time of 23:00, the maximum available readout power had decreased to below the threshold of 17 μW required for an optical pi pulse, causing the measurement to abort. A possible explanation for these power drifts might be the changes in temperature in the lab. When the temperature started to decrease at around 20:00, the laser power also started to decrease. The fluctuations over time in the temperature at the optical table of the Node 1 set-up are also plotted Fig. 5.6.

5.2.3 ZPL Single-Photon Detections

As explained in Chapter 3 (section 3.2), a repeated sequence of two consecutive optical pi pulses will yield three peaks in the measured number of counts in both detectors as a function of time after the SYNC. A histogram of the measured single photon counts in both detectors converted to Hz are shown

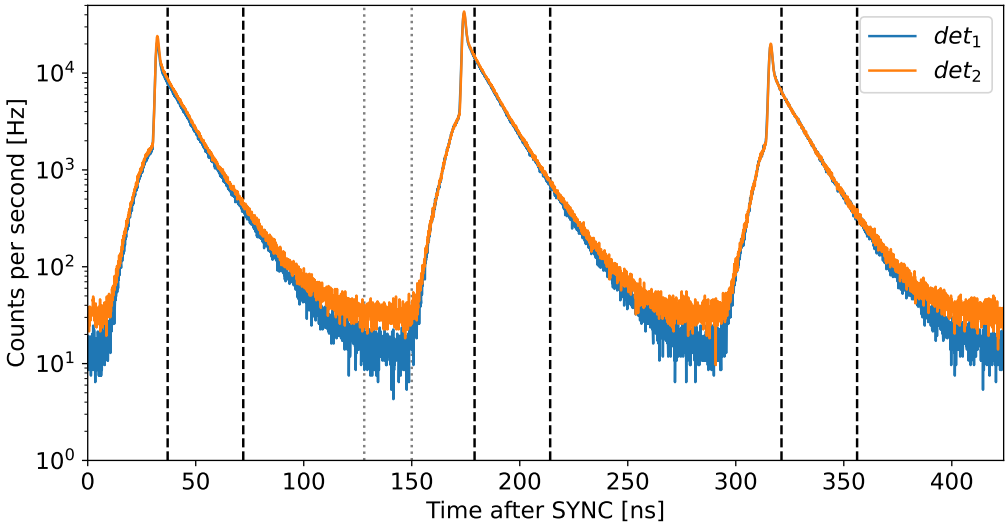

Figure 5.7: Measured count rate in Hz in both detectors as a function of time after the SYNC in ns. The black striped vertical lines indicate the chosen time window of photon counts used for the coincidence analysis. The grey dotted vertical lines indicate the time window where noise counts are recorded.

in Fig. 5.7 as a function of the time after the SYNC pulse. The histogram binning size is the same as the binsize of the time-tagger, being 80 ps. The highest narrow peak at the start of each rise in counts is due to reflected pulse light that is not fully rejected. The exponential decay of the NV light is visible as a straight line on the semi-log scale of the plot. The flat count rate in between the signal of two peaks is due to noise counts. In the following paragraphs, the argumentation for the selection of the signal- and noise windows is presented.

Selecting noise windows

The grey-dotted window in Fig. 5.7 is the region where the noise floors of both detectors are determined, from a time of 128 ns to 150 ns after the sync pulse. This window is chosen as it contains negligible light from the NV center, indicated by the flat slope. It does not contain any pulse light as the signal representing the second peak has not started yet. Therefore, the only contribution of registered photons in this window must be due to dark- and noise counts. The noise floor of detector 2 is higher than the noise floor of detector 1.

Selecting signal windows

For the TPQI coincidence analysis, three windows must be selected containing only single photons emitted by the NV center. To this end, the start and end of the first window is determined based on signal-to-noise ratio arguments. The second and third window use these same window start and end, but require an extra time shift of $+T$ and $+2T$, respectively, where $T = 142$ ns is the calibrated time between the two optical pi pulses.

The decision in choosing the start of the window is based on maximizing the number of detected counts emitted by the NV center, while at the same time minimizing noise contributions due to the reflections of the optical pi pulse light. The data of the optical pi pulse calibration presented in section 5.1 is used to determine when in time reflections of the pulse light are not present anymore. Due to more repetitions of the optical pi pulses in the single NV TPQI experiment as compared to this optical pi pulse calibration, the data of the latter is scaled. A plot of the scaled data from the optical pi pulse overlaid

with the earliest peak of the count rates of Fig. 5.7 is included in the Appendix, see also Fig. B.1. In this way, a window start of 37 ns after the SYNC is chosen, ensuring that the contribution of residual pulse photons in the time window is minimal with an estimated signal-to-noise ratio of above 50.

The end of the window is selected such that the signal-to-noise ratio in each detector exceeds a value of 10 at all times after the SYNC. As detector 2 has the highest noise floor, we use this as noise level. The point in time where the count rate level of 11 times the noise rate of detector 2 crosses the decaying signal the earliest is determined as the window end. In this way, the criterion of an SNR above 10 in all the three time windows is ensured. This yields a window end of 72 ns after the SYNC. The full window length is therefore 35 ns.

5.2.4 Correction Factors

To extract the photon indistinguishability J from the measured coincidence counts, a correction for system imperfections is required, as explained in Chapter 3 in Section 3.2. The parameters needed for these corrections are the long and short arm passing probabilities, the splitting ratio of the second beamsplitter, the classical fringe contrast, the average number of photons per excitation per detector and the noise rates in both detectors (P_S, P_L, T/R, FC, CPS_1, CPS_2, Γ_1 and Γ_2). These parameters, except for the fringe contrast, are extracted from all the single photon counts that together constitute Fig. 5.7. These parameters can be determined with a certain accuracy. To deduce how accurate, or with which standard deviation, these parameters can be extracted from the dataset, the fluctuations of each parameter over time are determined.

For that reason, the full dataset of 540 measurement repetitions is split in sets of 12, yielding a total of 45 groups of 12 datasets. The decision on the number of sets is based on the period of the calibration block in the measurement, which occurred every 12 measurement repetitions. The calibrations took place approximately every 15 min. Therefore, if a parameter is computed for each group of measured photon counts, each instance of that parameter represents its state of the past 15 min.

Passing probabilities long and short arm

The first two parameters which are determined are the long and short arm passing probabilities, being P_S and P_L. The ratio of these factors can be interpreted as the ratio of photons that entered the single NV TPQI set-up and passed through the short arm, or the long arm. Therefore, the ratio of these parameters represents both the splitting ratio of the first beamsplitter, and the imbalance in photon loss in the short versus the long arm. It is expected that the ratio of P_S/P_L is larger than 1 as photons have a smaller probability to be lost in the short arm than the long arm. They can be determined from the number of measured counts in the first time window of Fig. 5.7, which contains only photons that travelled the short arm, and the number of measured counts in the last time window, which only contains photons that travelled the long arm. These two probabilities are the same for both reflected pulse light and NV photons. To reduce the error bar on P_S and P_L, larger time windows are selected also containing reflected pulse light. The window end is kept at the same time after the SYNC as in the coincidence analysis, being 72 ns. The window start is moved to the left, to a time of 25 ns after the SYNC.

Per group, the total number of photon detections summed in both detectors (1,2) in the first time window (E, early) is determined, and labelled as $E_1 + E_2$. The noise floors of both detectors are subtracted from E_1 and E_2. These noise floors are calculated as the noise rate per detector times the selected window length. Similarly, the total number of photon detections summed in both detectors in the third time window (L, late) is determined, yielding L_1 and L_2. The parameters P_S and P_L are then determined as

$$\begin{aligned} P_S &= \frac{E_1 + E_2}{E_1 + E_2 + L_1 + L_2}, \\ P_L &= \frac{L_1 + L_2}{E_1 + E_2 + L_1 + L_2}. \end{aligned} \tag{5.1}$$

In this way, these two parameters are normalised such that $P_S + P_L = 1$. The standard deviation of each instance of P_S and P_L is calculated using error propagation, using that the standard deviations of E_1, E_2, L_1 and L_2 are equal to the square root of the number due to the underlying Poisson statistics of single photon counts.

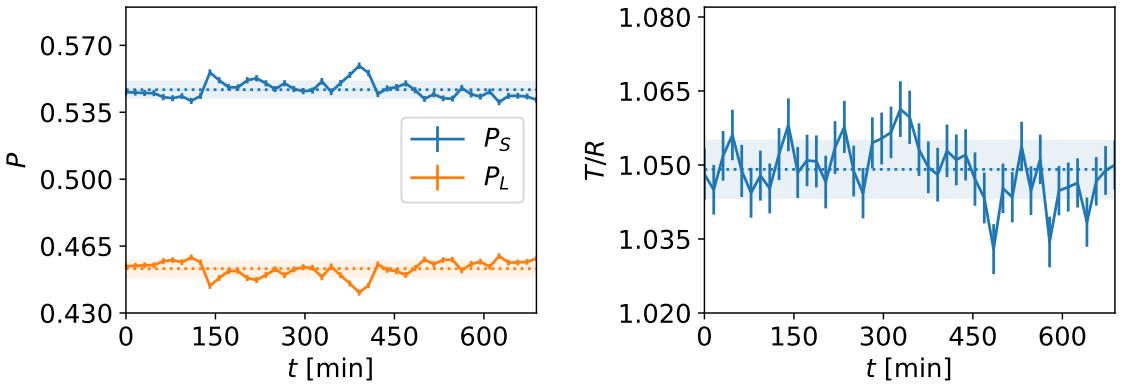

(a) The parameters P_S and P_L versus the total measurement time t in min, including error bars representing one standard deviation. The dotted line indicates the mean over time, the shaded areas indicates one standard deviation of the instances over time, yielding $P_S = 0.547 \pm 0.004$ and $P_L = 0.453 \pm 0.004$.

(b) Splitting ratio T/R of the second beamsplitter over the total measurement time t in min, including error bars representing one standard deviation. The dotted line indicates the mean over time, the shaded areas indicates one standard deviation of the instances over time, yielding $T/R = 1.049 \pm 0.006$.

Figure 5.8: The parameters defining the imbalances in the two beamsplitters and the imbalance in losses in the interferometer.

In Fig. 5.8a, P_S and P_L are plotted as a function of total measurement time including error bars. The fluctuations around the mean values over time are larger than the error bars representing one standard deviation of the individual data points. Therefore, the uncertainty of the final P_S and P_L is taken as the standard deviation of the data points over time. This gives $P_S = 0.547 \pm 0.004$ and $P_L = 0.453 \pm 0.004$.

Splitting ratio second beamsplitter

To determine the splitting ratio of the second beamsplitter, the number of photon counts in the early and late time bin are used again. This splitting ratio is the same for both reflected pulse light and NV photons. Therefore, the same time window of 25 ns until 72 ns is used, just as in the calculation of the factors P_S and P_L. The number of counts in the early and late time bins per detector, with the corresponding noise contribution subtracted, and per group of 12 measurement repetitions (E_1, E_2, L_1 and L_2) are therefore the same as in Section 5.2.4.

These integrated photon counts per group of the two detectors (1,2) in the early E and late L time bin are $E_1 = N\eta_1 T_1 \epsilon_S R_2$, $E_2 = N\eta_2 T_1 \epsilon_S T_2$, $L_1 = N\eta_1 R_1 \epsilon_L T_2$ and $L_2 = N\eta_2 R_1 \epsilon_S R_2$, where N is the total number of input photons, η_i is the detection efficiency of detector i, ϵ_j is the photon survival probability of arm j and R_i, T_i are the reflectivity and transmissivity of beamsplitter i. The splitting ratio of the second beamsplitter is therefore given as $T/R := T_2/R_2 = \sqrt{\frac{L_1 E_2}{E_1 L_2}}$. The standard deviation of each instance of the splitting ratio T/R is calculated using error propagation of the standard deviations of the parameters E_1, E_2, L_1 and L_2.

In Fig. 5.8b, the splitting ratio is plotted as a function of total measurement time including error bars. Again, the fluctuations around the mean values over time are slightly larger than the error bars representing one standard deviation of the individual data points. Therefore, the uncertainty of the final T/R is taken as the standard deviation of the data points over time. This yields $T/R = 1.049 \pm 0.006$. Using the second equation $R + T = 1$, one can solve for the two parameters R and T. To determine the uncertainty of the R and T itself, it is assumed that the standard deviation of R equals the standard deviation of T; $\sigma_R = \sigma_T = \sigma_{RT}$. Using

$$\sigma_{T/R} = \frac{T}{R}\sqrt{\frac{\sigma_R^2}{R^2} + \frac{\sigma_T^2}{T^2}} = \frac{T\sigma_{RT}}{R}\sqrt{\frac{1}{R^2} + \frac{1}{T^2}},$$

one can solve for σ_{RT}, yielding $\sigma_{RT} = \sigma_{T/R} \cdot \frac{R}{T} \cdot \sqrt{\frac{R^2 T^2}{R^2 + T^2}}$. This gives $R = 0.488 \pm 0.002$ and $T = 0.512 \pm 0.002$.

Counts per Shot

The counts per shot per detector i (CPS_i)is defined as the average probability that one optical pi pulse generates an NV photon, and that this photon is detected. It is dependent on the selected time window. Now, the same signal windows are used as for the single photon coincidence analysis. Therefore, the parameters E_1, E_2, L_1 and L_2 are redefined to the shorter signal window containing only NV photons with a window start of 37 ns and a window end of 72 ns. The noise floor of each detector is subtracted from the corresponding parameter. These parameters are again determined per group of 12 measurement repetitions to see the fluctuation of CPS_i over time. The first beamsplitter splits the signal of one optical pi pulse over two arms. As we only consider the windows where no interference of photons has taken place, we define the combination of the photons of the first optical pi pulse that travelled the short arm (E_i) plus the photons of the second optical pi pulse that travelled the long arm (L_i) as the signal of one full optical pi pulse detected in detector i. This gives

$$CPS_i = \frac{E_i + L_i}{N_{\text{SYNCs}}}, \tag{5.2}$$

where N_{SYNCs} is number of recorded syncs per group of 12 measurement repetitions. The overall counts per shot (CPS) is then defined as $CPS_1 + CPS_2$. The standard deviation of each instance of CPS_i per detector is calculated using error propagation.

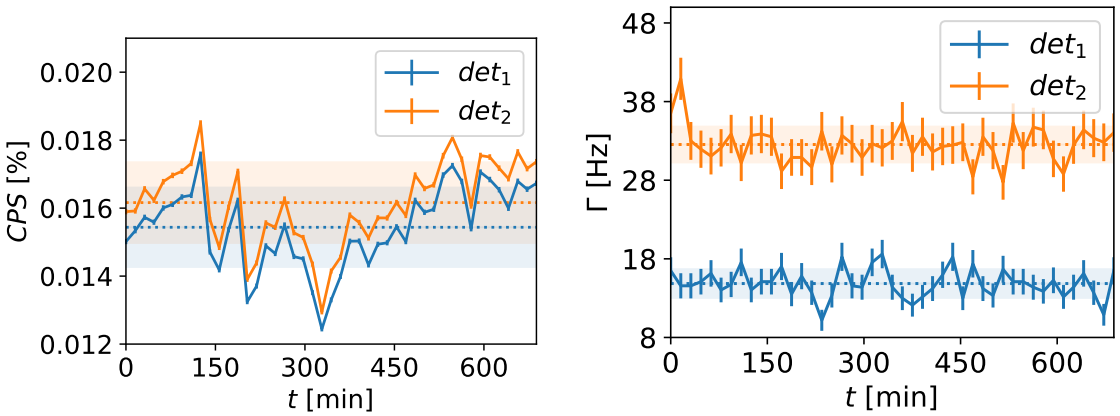

(a) The counts per shot per detector versus the total measurement time t in min, including error bars representing one standard deviation. The dotted line indicates the mean over time, the shaded areas indicates one standard deviation of the instances over time, yielding $CPS_1 = 0.0154 \pm 0.0012$ % and $CPS_2 = 0.0162 \pm 0.0012$ %.

(b) The noise rates per detector versus the total measurement time t in min, including error bars representing one standard deviation. The dotted line indicates the mean over time, the shaded areas indicates one standard deviation of the instances over time, yielding $\Gamma_1 = 14.9 \pm 1.8$ Hz and $\Gamma_2 = 32.5 \pm 2.3$ Hz.

Figure 5.9: The parameters used to correct for coincidence events caused by detector noise counts.

In Fig. 5.9a, both CPS_1 and CPS_2 are plotted as a function of time including error bars representing one standard deviation. It can be seen that the fluctuations around the mean values over time are larger than the error bars of the individual data points. Therefore, the uncertainty of the final CPS_i is defined as the standard deviation of the data points over time. This yields the values of $CPS_1 = 0.0154 \pm 0.0012$ % and $CPS_2 = 0.0162 \pm 0.0012$ %. The optical pi pulse calibration right before the start of the TPQI measurement gave a maximum counts per shot in the ZPL of $CPS = 0.0530 \pm 0.0017$ %, measured directly at the output of the ZPL fiber. Compared with the total CPS measured with the imbalanced interferometer in between, being $CPS_1 + CPS_2 = 0.0316 \pm 0.0017$ %, the total losses introduced by the single NV TPQI setup are calculated to be 2.2 dB.

Noise Rates

The noise rate per detector, Γ_i, is determined by integrating the measured number of photon counts in the noise window per group, and dividing by the total number of SYNCs times the length of the noise window. It is assumed that noise counts are also Poissonian distributed. The standard deviation of each

instance of Γ_i per detector is then determined as the square root of the measured number of photon counts in the noise window, divided by the total number of SYNCs times the length of the noise window.

In Fig. 5.9b, both Γ_1 and Γ_2 are plotted as a function of time including error bars representing on standard deviation. The fluctuations around the mean values over time are larger than the error bars of the individual data points. Therefore, the uncertainty of the final Γ_i is defined as the standard deviation of the data points over time. This yields the values of $\Gamma_1 = 14.9 \pm 1.8$ Hz and $\Gamma_2 = 32.5 \pm 2.3$ Hz.

Classical Fringe Contrast

The classical fringe contrast is measured in the period of calibrations shown in the schematic representation of the applied measurement sequence in Fig. 4.6. To this end, the objective stage moves its focus to the gold stripline of the sample. For a duration of 30 s, a readout power of 5 nW is reflected from the stripline. The highly coherent and monochromatic reflections of this readout laser light enter the ZPL, and the light travels through the imbalanced interferometer. Due to the varying phase difference of the light in the short arm versus the long arm, constructive and destructive interference will take place [18]. As a result, the intensity of the light, and so the measured number of counts, in the two output arms of the second beamsplitter fluctuates. In ideal settings, meaning perfectly monochromatic and coherent light and an ideal interferometer, the fringe contrast FC will equal 1. It is defined in Eq. (5.3) as

$$FC = \frac{P_{max} - P_{min}}{P_{max} + P_{min}}, \tag{5.3}$$

where P_{max} is the highest measured power, and P_{min} is the lowest measured power. The number of

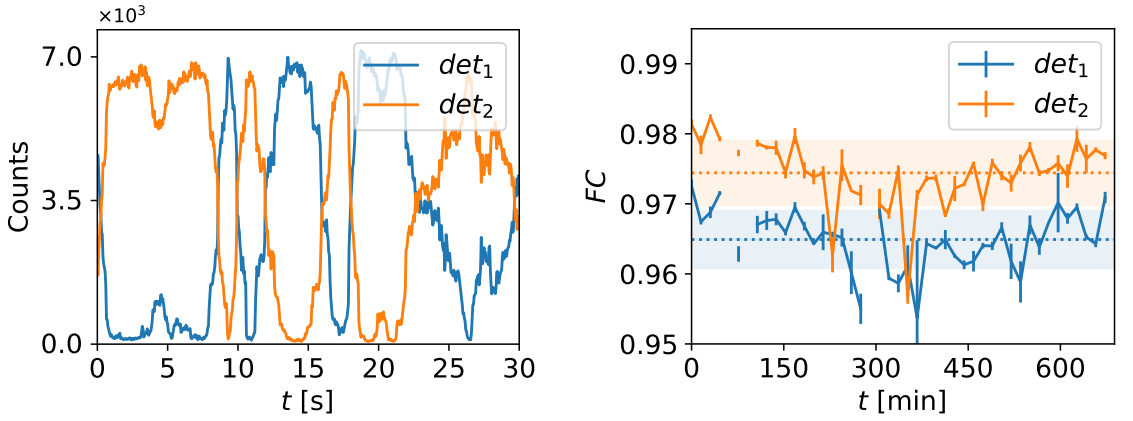

(a) Fluctuations of the measured number of counts in the two detectors, over the course of 30 s. This trace corresponds to the very first fringe contrast measurement.

(b) The measured fringe contrast FC per detector versus the total measurement time t in min, including error bars representing one standard deviation. The dotted line indicates the mean over time, the shaded areas indicates one standard deviation of the instances over time.

Figure 5.10: Fringe contrast measurements to be able to correct for polarisation effects in the interferometer, yielding $FC_{\text{det}_1} = 0.965 \pm 0.004$ and $FC_{\text{det}_2} = 0.974 \pm 0.005$.

counts in the two output arms is measured for a total duration of 30 s. This is done by integrating the measured number of counts of 50 ms intervals. This results in the trace shown in Fig. 5.10a. In every such trace, the average number of counts of the two highest peaks per detector is taken, resulting in the parameter P_{max}. Also, the average number of counts of the two lowest valleys per detector is taken, resulting in the parameter P_{min}. Then the fringe contrast for each detector at this time instance in the full measurement can be calculated using Eq. (5.3). The standard deviation σ_{FC} per detector is calculated using error propagation.

During the full measurement of 12 hours, the fringe contrast was measured 45 times. The measured instances are plotted against total measurement time in Fig. 5.10b. Sometimes, the measured number of counts did not reach a minimum or maximum during an instance measurement of 30 s, but it remained either flat, or the measurement time stopped during a slope. This is due to the phase difference between

the long and short arm being too constant during the particular measurement. These traces, which would result in a low fringe contrast, were removed from the data set, showing as gaps in the graph of Fig. 5.10b.

The fluctuations around the mean value over time are larger than the errorbars representing one standard deviation of the individual data points. Therefore, the uncertainty of the final fringe contrast per detector is taken as the standard deviation of the data points over time. This yields the values of $FC_{\text{det}_1} = 0.965 \pm 0.004$ and $FC_{\text{det}_2} = 0.974 \pm 0.005$. Due to the difference in detection efficiencies, the fringe contrast per detector is different. The final value used for the fringe contrast is taken as the average of the fringe contrast of the two detectors, corrected for detector efficiency imbalance, giving $FC = 0.970 \pm 0.003$. Due to imperfect splitting ratio's of the beamsplitters, imbalances in losses in the long versus the short arm, and possible polarisation modifications due to the finite polarisation extinction ratios, the measured fringe contrast is lower than the ideal value of 1. The theoretical limit of the fringe contrast of an interferometer with imbalanced beamsplitter ratios and imbalanced losses in the two arms is given by Eq. (3.29). Using P_S, P_L, and R and T as measured, this gives a theoretical maximum of $FC_{max} = 0.9931 \pm 0.0008$. The measured fringe contrast is corrected for the the imperfect splitting ratio's and imbalanced losses. It is not possible to correct for any other system imperfections as these could not be measured. The corrected fringe contrast (Eq. (3.30)) is therefore $FC_{corr} = 0.9768 \pm 0.0031$.

5.2.5 Photon Indistinguishability

The measured number of coincidence counts $C_0, C_{\pm 1}$ and $C_{\pm 2}$ in the selected signal windows are plotted as a function of the detection time difference τ in units of the calibrated time period T between two pulses in Fig. 5.11. The error bars represent one standard deviation. The typical Hong-Ou-Mandel dip of lower coincidence counts at 0 detection time difference is visible.

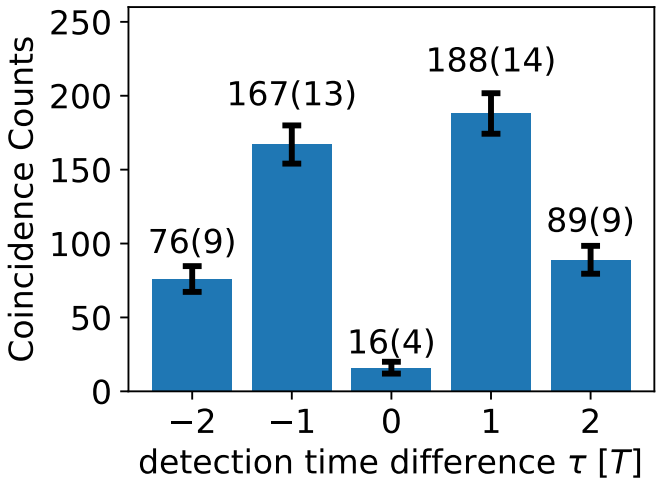

Figure 5.11: Measured number of coincidence counts as a function of the detection time difference τ in units of the calibrated time period T between two pulses, yielding a raw Hong-Ou-Mandel interference visibility of 0.91 ± 0.02

In the Appendix, in Fig. B.2, the coincidence counts are plotted as a function of the detection time difference in ns. The two-sided exponential decay of the peaks at large detection time difference, as predicted in the Chapter 3 is visible. Too little data is available to be able to fit a curve around $\tau = 0$, which would give insight in the frequency distribution of the photons. Without applying any corrections on the system imperfections, the raw Hong-Ou-Mandel interference visibility is determined as $V = 1 - 2 \cdot \frac{C_0}{C_{+1}+C_{-1}} = 0.91 \pm 0.02$.

To correct for the system imperfections, we use the correction method explained in Chapter 3 in Section 3.2. First, the coincidences caused by a combination of one NV photon and one darkcount are determined for each of the 5 detection time difference bins, $P_j^{dc,ph}$, using Eq. (3.25) with the measured parameters summarised in Table 5.1. Subtracting these contributions from the measured coincidences C_j yields the values $P_j^{ph,ph}$. These results are included in the Appendix, in Table B.1.

After the correction for noise contributions, we proceed with steps 2-6 of the correction method using the data and correction factors summarised in Table 5.1.

Parameter	Value	Type
$P_0^{ph,ph}$	13 ± 4	Poisson
$P_{+1}^{ph,ph}$	183 ± 14	Poisson
$P_{-1}^{ph,ph}$	163 ± 13	Poisson
$P_{+2}^{ph,ph}$	87 ± 9	Poisson
$P_{-2}^{ph,ph}$	75 ± 9	Poisson
P_S	0.547 ± 0.004	Normal
P_L	0.453 ± 0.004	Normal
R	0.488 ± 0.002	Normal
T	0.512 ± 0.002	Normal
FC	0.970 ± 0.003	Normal
CPS_1	0.0154 ± 0.0012 %	Normal
CPS_2	0.0162 ± 0.0012 %	Normal
Γ_1	14.9 ± 1.8 Hz	Normal
Γ_2	32.5 ± 2.3 Hz	Normal

Table 5.1: Summary of all system parameters extracted from the measurement data, including one standard deviation. The distributions of the parameters are included as well.

In combination with the Monte-Carlo error propagation method, we find the final value of the photon indistinguishability $J = 0.945$ in the interval [0.920, 0.966] with 68.3% confidence. The distribution of the array of **J** of size $N = 10 \cdot 10^6$ is shown in Fig. 5.12.

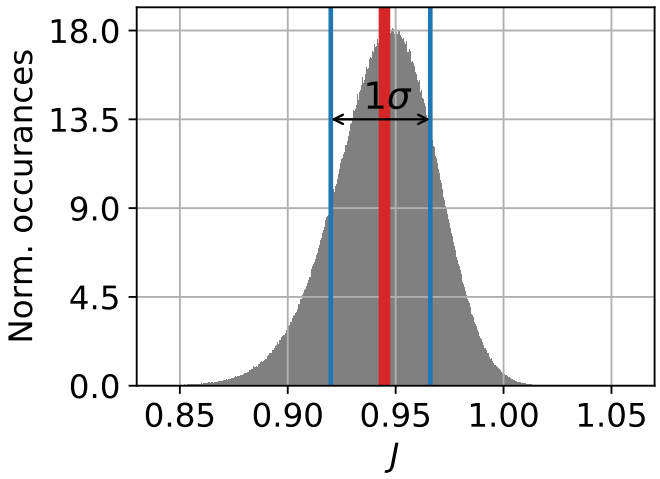

Figure 5.12: Histogram of the array of the photon indistinguishability **J**, generated by a Monte-Carlo method with $N = 10 \cdot 10^6$ samples. The value of $J = 0.945$ is depicted in red, with the derived asymmetric 68.3% (1σ) confidence interval of [0.920,0.966] in blue.

There can be seen in this histogram that there is a very small probability to get a value of J above 1. This is an nonphysical situation, yet included here for completeness. Using the distributions of the found correction parameters, the Monte-Carlo method might introduce an over-correction of the measured coincidences, as there has not been put any restrictions on the correction parameters.

The measured value of J indicates that the photons emitted by the NV center on Node 1 are highly indistinguishable, which is expected from a self-interference experiment. The possible causes of the deviation from the ideal value of $J = 1$ are investigated using the single NV TPQI model.

5.3 Single NV TPQI model

In this section, the probabilities of coincidence events given different configurations of two photons at the input of the second beamsplitter, as derived in Chapter 3, will be used to calculate the expected number of coincidences in each of the five detection time difference bins, given the measured system imperfections. Two extra parameters need to be introduced, being the probability to actually get two photons in the required configuration at the input of the second beamsplitter, P_{occ}, and the number of tryouts in the experiment, N. The occurrence probability is derived using the probabilities to pass through the short and the long arm, P_S and P_L, and the photon counting argument. The arrival times of the photon in the short arm, dt_S, and the photon in the long arm, dt_L, can be derived as well. This is summarised in Table 5.2.

	-2*T*	**-1*T***	**0*T***	**1*T***	**2*T***
P_{occ}	$P_S P_L$	$P_S P_S + P_L P_L$	$2P_S P_L$	$P_S P_S + P_L P_L$	$P_S P_L$
Arrival times	$dt_S << dt_L$	$dt_S << dt_L$	$dt_S \approx dt_L$	$dt_S << dt_L$	$dt_S << dt_L$

Table 5.2: The occurrence probabilities and relative arrival times of the two photons in the long and short arm, for each of the five detection time difference bins.

Coincidence counts with detection time difference of $\pm 2T$ can only occur if the first photon took the short arm, and the second photon the long arm. Photon S will therefore always arrive before photon L, fixing the sign of the arrival time difference. Coincidence counts with a detection time difference of $\pm 1T$ can only occur if both photons take the same arm. Similar to the $\pm 2T$ case, we also fix the sign of the arrival time difference in this case. The argumentation why this assumption is valid will follow in the next section, 5.3.1.

In the next section, the model is extended by considering these occurrence probabilities, and also verified considering extreme cases. Next a comparison between the model and the data will be made. To be able to compare the model with the measurement data, we need to calculate the expected amount of coincidence events in each of the 5 detection time difference bins. Therefore, we need to multiply the derived coincidence probabilities in each bin with the number of sent out excitation pulses N and the probability that two photons are emitted and detected in each detector, $CPS_1\,CPS_2$. The expected number of coincidence counts per bin as a result of a darkcount and one NV photon are calculated as well, using the Equations 3.25, and added to the expected number of photon-photon coincidence counts per bin.

5.3.1 Model with Occurrence Probabilities

The coincidence probability is derived for three possible configurations of photons at the second beamsplitter, being the case where the two photons have a very small arrival time difference, an arrival time difference of $1T$ and an arrival time difference of $2T$.

Small or zero arrival time difference

The time between two optical pi pulses, T, is calibrated to the difference in travelling time in the long versus the short arm. If, however, this calibration is a bit off, the photons will arrive at a small arrival time difference D at the second beamsplitter, see also Fig. 3.5a. This increases the coincidence probability as the photons become slightly distinguishable in arrival time.

For the case when $D = 0$ and the two photons are perfectly indistinguishable in their frequencies (and polarisation), an analytical expression of the coincidence probability using a window start of WS and a window end of WE is given by equation Eq. (3.22). This window start and - end is defined with respect to the excitation step. We verify if the numerical integration by the Simpson's rule as in Eq. (3.20) yields the same result by setting $\sigma_\Delta = \mu_\Delta = 0$. The found deviation of the numerical result from the expected value is less than 0.32%. By increasing the number of data points for the two detection times t_1 and t_2, this deviation will decrease.

An arrival time difference of 0 (or $D << \tau_l$) will result in a possible detection time difference that falls in the $0T$ detection time difference bin. Therefore, we define

$$P_{\text{coinc}}(0T) = P_{\text{coinc}}(dt_S \approx dt_L) \cdot P_{\text{occ}}(0T), \tag{5.4}$$

with $P_{\text{coinc}}(dt_S \approx dt_L)$ as in Eq.(3.20), and $P_{\text{occ}}(0T) = 2P_S P_L$ as explained by the photon counting argument.

Arrival time difference of $1T$

In the experiment, two photons will only arrive at an arrival time difference of one pulse period T at the second beamsplitter when they both consecutively pass through the short arm, or both consecutively pass through the long arm. The coincidence probabilities are derived assuming two photons in distinct input ports. One could argue that this derived coincidence probability is not valid anymore if the photons arrive in equal input ports. However, as the arrival time difference is much larger than the lifetime, no interference will be observed anyway: the photons are distinguishable. For a balanced beamsplitter, the coincidence probability will be the same for the case of two photons in distinct input ports at a large arrival time difference, and for the case of two photons in equal input ports at a large arrival time difference. For an imbalanced beamsplitter, however, this probability needs to be corrected. Instead of two reflections or two transmissions, one reflection and one transmission is required to get a coincidence event. Using Eq. (3.2) for the case of distinct input arms, and Eq. (3.3) for the case of equal input arms, the required correction factor is calculated as the ratio of those two, yielding $\frac{2RT}{R^2+T^2}$. This correction factor equals 1 in the case of a balanced beamsplitter. Therefore, the situation occurring in the experi-

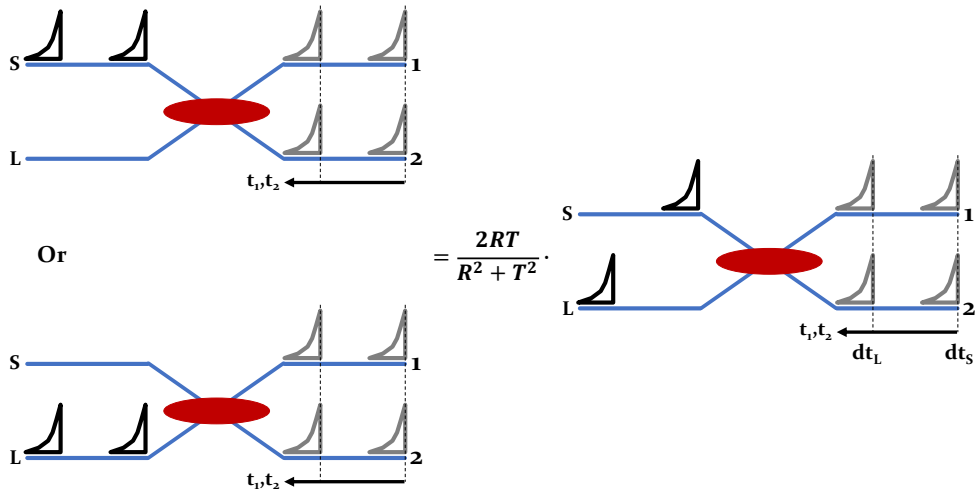

Figure 5.13: Equivalence of two input photons in equal input ports at a large arrival time difference, with two input photons in distinct input ports using a correction factor.

ment depicted on the left side in Fig. 5.13 is equivalent to the situation depicted on the right side of this figure, if the correction factor is applied. Here, we define photon S to arrive earlier than photon L, i.e. $dt_S << dt_L$. This yields the coincidence probability

$$P_{\text{coinc}}(+1T) = \frac{2RT}{R^2+T^2} P_{\text{coinc}}(\text{det1 first} | dt_S << dt_L) \cdot P_{\text{occ}}(+1T), \tag{5.5}$$

and

$$P_{\text{coinc}}(-1T) = \frac{2RT}{R^2+T^2} P_{\text{coinc}}(\text{det2 first} | dt_S << dt_L) \cdot P_{\text{occ}}(-1T), \tag{5.6}$$

with $P_{\text{coinc}}(\text{det1 first} | dt_S << dt_L)$ and $P_{\text{coinc}}(\text{det2 first} | dt_S << dt_L)$ as in Eq. (3.18) and Eq. (3.19), respectively. The occurrence probabilities are given as $P_{\text{occ}}(\pm 1T) = P_S P_S + P_L P_L$, as explained by the photon counting argument.

Arrival time difference of $2T$

An arrival time difference of $2T$ will result in a possible detection time difference in the $+2T$ or $-2T$ bin, depending on which detector clicks first. In the experiment, the only possibility that contributes to this case is when photon S arrives $2T$ earlier than photon L. This yields the coincidence probabilities

$$P_{\text{coinc}}(+2T) = P_{\text{coinc}}(\text{det1 first}|dt_S << dt_L) \cdot P_{\text{occ}}(-2T), \tag{5.7}$$

and

$$P_{\text{coinc}}(-2T) = P_{\text{coinc}}(\text{det2 first}|dt_S << dt_L) \cdot P_{\text{occ}}(+2T), \tag{5.8}$$

with $P_{\text{coinc}}(\text{det1 first}|dt_S << dt_L)$ and $P_{\text{coinc}}(\text{det2 first}|dt_S << dt_L)$ as in Eq. (3.18) and Eq. (3.19), respectively. The occurrence probabilities are given as $P_{\text{occ}}(\pm 2T) = P_S P_L$, as explained by the photon counting argument.

Coincidence probabilities for a perfect system with distinguishable photons

As explained in Section 3.2 the expected probabilities of a coincidence event in the five pulse difference bins are $1/8 : 1/4 : 1/4 : 1/4 : 1/8$ for a perfect interferometer modelled as $R = T = P_S = P_L = 1/2$, and fully distinguishable photons. In the model, the photons are made distinguishable in their frequencies by letting $\mu_\Delta \to \infty$. With the earliest possible window start of $WS = 0$ and in the limit of large window length, the model should recover the expected probabilities in each detection time difference bin. The obtained probabilities by using the model are shown in the Appendix, in Fig. B.3. The deviation from the expected probabilities in each bin is less than 0.25 %, confirming that the model works. The small deviation is attributed to finite precision due to numerical integration.

5.3.2 Comparison Model and Data

The measured system imperfections are now incorporated in the model, using $P_S = 0.547$, $P_L = 0.453$, $R = 0.488$ and $T = 0.512$ and the number of sent out optical pi pulses $N = 23.328 \cdot 10^9$. The expected number of coincidence events due to a dark count and one NV photons per detection time difference bin is calculated using Eq. (3.25). The same window length as in the experiment is used, being 35 ns. In the model this is included by setting the window start WS =0 ns, and the window end WE = 35 ns. The parameters controlling the frequency difference of the two photons are both set to 0, i.e. $\mu_\Delta = \sigma_\Delta = 0$. The lifetime τ_l is set to the excited state lifetime of the NV center, being 12 ns.

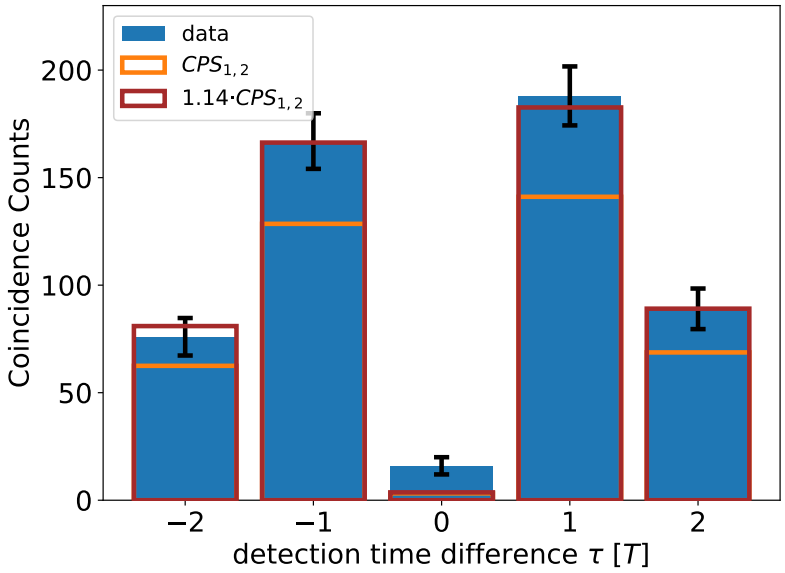

Figure 5.14: Expected number of coincidence counts by the model for the measured counts per shot values in orange, and the scaled counts per shot values in red, overlaid with measurement data in blue.

The expected number of total coincidence counts per detection time difference bin is calculated using the values $CPS_{1,2}$ found in the experiment. The same calculation is done a second time with scaled values of $CPS_{1,2}$, with a scaling factor of 1.14 times the values found in the experiment. The results are overlaid with the measurement data in Fig. 5.14.

If the scaling factor of 1.14 is applied in both of the measured CPS values, the model agrees within error bar with the data in all the detection time difference bins, except for the 0 bin. It is not known why this extra scaling factor is required in the model to get overlap with the data. It might be possible that the method to extract the CPS from the measurement data underestimates the actual probability to measure a ZPL photon given one optical pi pulse.

There are more coincidence counts measured in the 0 detection time difference bin than can be predicted by the now included system imperfections of imbalanced beamsplitters and dark count contributions. Three possible causes of the higher coincidence counts in this bin can be identified. Either, the delay of the interferometer is wrongly calibrated, resulting in a non-zero arrival time difference in the 0 bin. Another cause is a frequency mismatch between the photons, meaning that the photons are slightly distinguishable in frequency. The third cause can be the effect of polarisation mismatch. It might be that the interferometer slightly changes the polarisation of the two photons in a different way. The first two causes can be investigated by using the model.

Using the model, we can identify what arrival time difference would result in the same amount of measured coincidence in the 0 bin. To this end, we sweep the value of D for the case of the scaled CPS-values. In Fig. 5.15a, the number of coincidence counts in the 0 detection time difference bin as predicted by the model is plotted as a function of the arrival time difference D. An arrival time difference of $D = 2.0$ ns can explain the measured number of coincidences in the 0 detection time difference. The calibration of the delay in the interferometer was done with an accuracy limited by the AWG sample time being 0.416 ns. It is therefore unlikely that the calibration of the delay was 2 ns off. However, a mismatch in arrival time in the order of this 0.416 ns is possible.

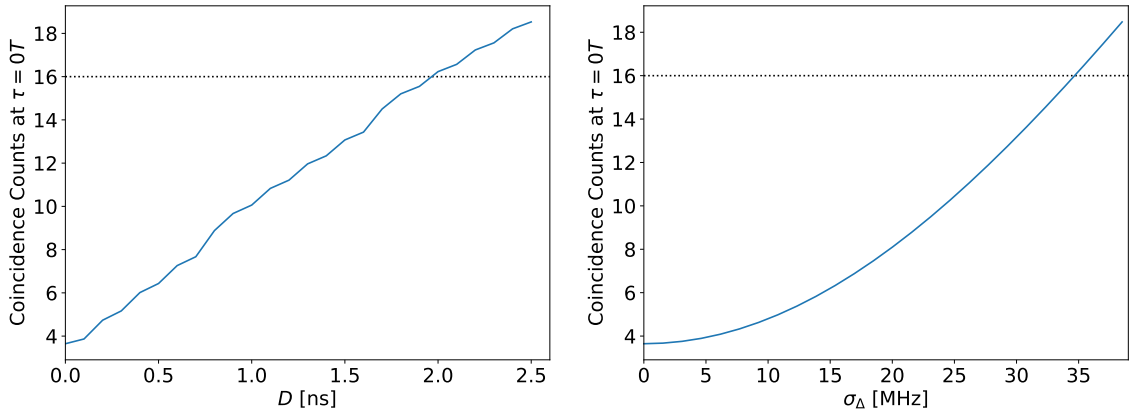

(a) The predicted number of coincidence counts in the $0T$ detection time difference bin as a function of the arrival time difference D of the two photons.

(b) The predicted number of coincidence counts in the $0T$ detection time difference bin as a function of the standard deviation of the frequency difference σ_Δ of the two photons.

Figure 5.15: Possible explanations of the higher measured number of coincidence counts (black dotted line) in the $0T$ detection time difference bin.

Again using the model, we can identify what standard deviation of the frequency difference would result in the same amount of coincidences in the 0 bin as measured. To this end, we sweep the value of σ_Δ for the case of the scaled CPS-values. The average of the frequency difference is still set to $\mu_\Delta = 0$. In Fig. 5.15b, the number of coincidence counts in the 0 detection time difference bin as predicted by the model is plotted as a function of the standard deviation of the frequency difference σ_Δ. A value of $\sigma_\Delta = 0.0347\,\text{ns}^{-1} = 34.7$ MHz can explain the measured number of coincidences in the 0 detection time difference. In the short period between 2 consecutive optical pi pulses, it is unlikely that perturbations which broaden the emission line take place. If the NV center is entirely undisturbed, the spectral profile of the ZPL is purely Lorentzian with a full-width half-maximum (FWHM) of $\frac{1}{2\pi\tau_l} = 13$ MHz [24]. Therefore, the assumption that the frequency difference between the two consecutively emitted photons is Gaussian might actually not be the best. It is advised to redo the calculations with a Lorentzian spectral

profile. Nevertheless, it is not excluded that two consecutively emitted photons of a single NV center, both taken from the same Lorentzian spectral distribution centered at 637 nm with a FWHM of 13 MHz, have a slight frequency difference. If the single NV TPQI experiment would have been done over a longer measurement time thus resulting in more coincidence events, then information of the frequency distribution of the emitted photons could have be found from a fit of the dip in measured coincidence events as a function of the detection time difference τ around $\tau = 0$, as was explained in Chapter3. This graph is included in the Appendix, see Fig. B.2.

Most likely, the combination of an accidental small arrival time difference (<0.416 ns) and an inherent slight distinguishability due to the frequency difference of two consecutively emitted ZPL photons explains most of the coincidence counts in the 0 bin. An extra contribution of the measured raw coincidence counts in the 0 bin can be a result of polarisation effects. In the measurement, the final indistinguishability is corrected for possible polarisation effects by using the classical fringe contrast. In this model, the direct effect on the raw coincidence events as a result of polarisation mismatch cannot be investigated. The model can be extended to also include possible polarisation mismatches of the photons.

5.4 Two NV TPQI model

The derived two-photon coincidence probabilities in Chapter 3 can also be used for the prediction of a two-node TPQI experiment with photons down-converted to the telecom wavelength. A schematic of the set-up of such an experiment is given in Fig. 4.4. To this end, the labels S and L, referring to the short and long arm, respectively, are replaced with the labels A and B, where A represents the NV of Node 1 and B represents the NV of Node 2. The excited state lifetimes of the two NV centers are assumed to be equal (12 ns). The measured visibility V of a two-node TPQI experiment sets an upper limit to the Barett and Kok entanglement fidelity F, according to [19]:

$$F \leq 1/2 + 1/2V. \tag{5.9}$$

Here, we will derive what raw visibility can be measured with a two-node TPQI experiment with photons converted to the telecom wavelength, given the system imperfections. Both NV A and NV B are excited at calibrated times such that the emitted photons of both NV centers arrive at the beamsplitter simultaneously. We consider a two-pulse scheme, where each NV is excited two times, with a time between pulses called T. This will result in arrival time differences close to 0 ($dt_A \approx dt_B$), if the two NV centers actually both emit a photon in the same excitation pulse. When after each excitation pulse only one of the NV centers emits a photon, the arrival time difference will be $|dt_A - dt_B| = T$. In this case, the photons are distinguishable in arrival time as $T >> \tau_l$. The coincidence events as a function of the detection time difference τ will therefore show two large peaks at $\tau = \pm T$, and a (small) peak at $\tau = 0$.

We will derive the expected number of coincidence events in detection time difference bins of $\tau \in [-WL, WL]$, $\tau \in [T - WL, T + WL]$ and $\tau \in [-T - WL, -T + WL]$, where WL is the selected window length, given possible system imperfections. These three bins are called $0T$, $+1T$ and $-1T$. This will be derived as a function of σ_Δ. For the detection time difference bin $0T$, we assume that the arrival time difference between the two photons is Gaussian distributed with mean μ_D and standard deviation σ_D. This is included as an extra numerical integral over all possible values of D of the product of the Gaussian distribution of D, $f(D)$, and the derived P_{inh} as in Eq. (3.15) in the model. The integration is performed for various values of σ_D. For the detection time difference bins $\pm 1T$, the arrival time difference is T. As the photons are already distinguishable in arrival time, the extra effect of the Gaussian distribution of the arrival time around this value is negligible, and is not included.

We assume the mean of the frequency difference is $\mu_\Delta = 0$, as the quantum frequency converters can tune the frequencies of the photons to the same value. Dark counts are included as well, and are modelled as counts that are inherent to the used detectors, and therefore do not travel through the system. This way of modelling noise is actually the worst-case scenario. If fully distinguishable noise counts, from both the NV photons and other noise photons, would travel through the system, then they would only cause a coincidence count in 1/2 of the times (for a balanced beamsplitter). In this model with 2 excitation steps, it is assumed that at most 2 photons (or dark counts, or one photon and one dark count) are detected in one round of 2 excitations. The probability of multi-photon (≥ 3) detection events is neglected, as this will be even smaller than the probability of 2 photon detection events.

The expected number coincidence events due to a combination of a dark count and one photon is the same in each of the three detection time difference bins. It is calculated using

$$P^{dc,ph} = 2N\left[\Gamma_1 \cdot WL \cdot (T \cdot CPS_A + R \cdot CPS_B) + \Gamma_2 \cdot WL \cdot (R \cdot CPS_A + T \cdot CPS_B)\right], \tag{5.10}$$

where N is the number of 2-excitation rounds, Γ_i are the dark count rates per detector i and CPS_j is the average number of down-converted photons per excitation of $NV\,j$ detected by the telecom detectors, in the selected signal window. The expected number of coincidence counts due to two dark counts is also the same in each of the three detection time difference bins and is calculated using

$$P^{dc,dc} = N \cdot \Gamma_1 \Gamma_2 WL^2. \tag{5.11}$$

The expected number of photon - photon coincidence events per detection time difference bin is calculated using the derived coincidence probabilities, and read

$$\begin{aligned} P^{ph,ph}_{0T} &= \int_{-\infty}^{\infty} P_{\text{coinc}}(dt_A \approx dt_B, D) \cdot f(D)\,\mathrm{d}D \cdot P_{\text{occ}}(0T) \\ P^{ph,ph}_{+1T} &= P_{\text{coinc}}(\text{det1 first} | dt_A >> dt_B) \cdot P_{\text{occ}}(+1T) \\ P^{ph,ph}_{-1T} &= P_{\text{coinc}}(\text{det2 first} | dt_A >> dt_B) \cdot P_{\text{occ}}(-1T), \end{aligned} \tag{5.12}$$

where the coincidence probabilities are given by Equations (3.20), (3.18) and (3.19). Again, the situation where two photons are incident via the same port on the beamsplitter with a large arrival time difference is modelled as if they entered in distinct input ports, with applying a correction factor for possible beamsplitter imbalances. The cases where the photon from NV B was first to arrive are modelled as if the photon from NV A was first, as these are equivalent. The occurrence probabilities are derived using a photon counting argument included in Table B.2 in the Appendix, and read

$$\begin{aligned} P_{\text{occ},0T} &= N \cdot 4 \cdot CPS_A \cdot CPS_B \\ P_{\text{occ},\pm 1T} &= N \cdot \left(2 \cdot CPS_A \cdot CPS_B + CPS_A \cdot CPS_A \cdot f_{corr} + CPS_B \cdot CPS_B f_{corr}\right) \end{aligned} \tag{5.13}$$

where the correction factor $f_{corr} = 2RT/(R^2+T^2)$ is applied when two photons enter the beamsplitter in the same input port. The expected number of coincidences in each bin i is then given as $C_i = P_i^{ph,ph} + P^{dc,ph} + P^{dc,dc}$. The visibility is then determined as

$$V = 1 - \frac{2C_0}{C_{+1} + C_{-1}}. \tag{5.14}$$

Its standard deviation is determined by using error propagation, with the standard deviations of each of the parameters C_i taken as the square root of the value. The parameters presented in Table 5.3 are used in the model.

Parameter	**Definition**	**Value**
τ_l	lifetime	12 ns
WS	window start	0 ns
WE	window end	25 ns
μ_Δ	mean frequency difference	0
μ_D	mean arrival time difference	0
R	reflectivity	0.494
T	transmissivity	0.506
η_A	QFC_A conversion efficiency	0.51·0.1
η_B	QFC_B conversion efficiency	0.47·0.1
ϵ_{APD}	detection efficiency APD	0.75
$\epsilon_{1,2}$	detection efficiency SNSPDs	0.6
CPS_A	counts per shot converted photons node A	$0.07\ \% \cdot \eta_A \cdot (\epsilon_1+\epsilon_2)/(2\epsilon_{APD})$
CPS_B	counts per shot converted photons node B	$0.07\ \% \cdot \eta_B \cdot (\epsilon_1+\epsilon_2)/(2\epsilon_{APD})$
$\Gamma_{1,2}$	darkcount rates SNSPDs	80 Hz
T	period between excitations	150 ns
t_{meas}	measurement time	24 h
t_{ratio}	fraction of time spent on pulse sequences	0.13
t_{seq}	duration one pulse sequence	250 ns
N	number of pulse sequences	$t_{meas} \cdot t_{ratio}/t_{seq}$

Table 5.3: Parameters used for the two NV TPQI model.

The window length is 25 ns. Here, $\eta_{A(B)}$ is the conversion efficiency of the QFC of node A (B) including insertion losses from the narrow fiber Bragg grating, and t_{meas} is the total measurement time. The parameter t_{seq} is the time duration of each sequence of two pulses. The parameter t_{ratio} is the fraction of time in the full measurement spent on the actual two-pulse sequence, considering NV calibrations and CR checks also must take place. This is calculated using the single NV TPQI experiment, which yielded $1.17 \cdot 10^{10}$ two-pulse sequences over the course of 688 min. As each pulse sequence in the single node experiment took ~450 ns, we spent a fraction of $t_{ratio} = 0.13$ of the total measurement time on the pulse sequences itself. Assuming that the calibrations on the 2 nodes are done simultaneously and take the same amount of time, we estimate that we also spend a fraction of $t_{ratio} = 0.13$ of the total measurement time on the pulse sequence itself in a two-node experiment. This yields the expected raw HOM interference visibility plotted in Fig. 5.16a as a function of the standard deviation of the frequency difference and for different values of the standard deviation of the arrival time difference.

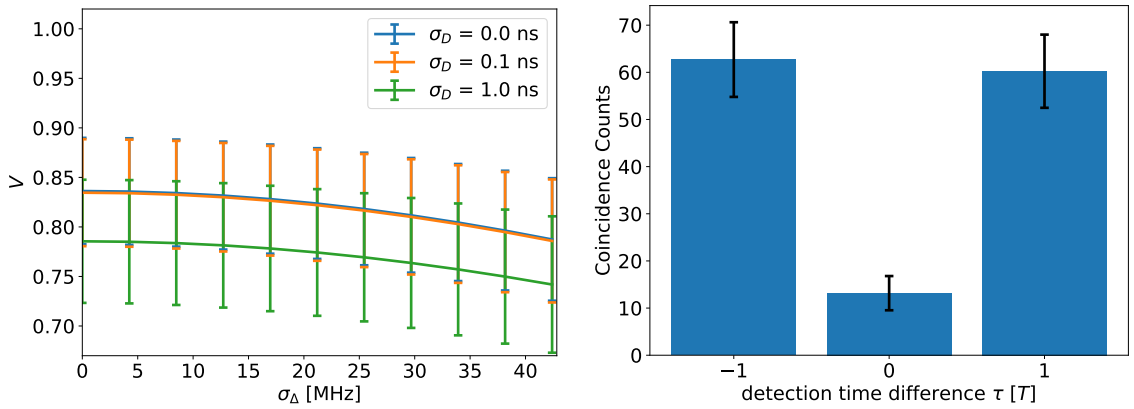

(a) Raw HOM interference visibility that can be measured during a 2-node TPQI experiment, as a function of σ_Δ, for different values of σ_D. Errorbars represent one standard deviation.

(b) Expected number of coincidences in the three detection time difference bins for a measurement taking 24 h when $\sigma_\Delta = 42.2$ MHz and $\sigma_D = 0.1$ ns.

Figure 5.16: Expectations of a 2-node TPQI experiment with photons down-converted to the telecom wavelength. The system parameters used in the model are shown in Table 5.3.

The timing accuracy is limited by the accuracy of the time-tagger and the EOMs used to excite the NV centers. It is expected that time jitter in 2-node experiments will be in the order of 0.1 ns. As can be seen in Fig. 5.16a, the effect of this timing jitter on the visibility with respect to the ideal situation ($\sigma_D = 0$) is small, it reduces the visibility by less than 0.2 % on average. If this jitter would be an order of magnitude larger ($\sigma_D = 1$ ns), the effect is more significant, resulting in a reduction of visibility of 6 % with respect to the 0 time jitter case.

As explained in Section 3.1.4, the frequency difference two photons emitted by two NV centers can be assumed to be Gaussian distributed in the limit of a long integration time, due to inhomogeneous broadening processes. The photons in the future 2-node experiment are down-converted in frequency. The narrow fiber Bragg grating which filters the photons in frequency has a Lorentzian shape, with a FWHM of 50 MHz. In the limit of very little inhomogenous broadening, i.e. $\sigma_\Delta << 50$ MHz, then the assumption of the Gaussian distribution of the frequency difference remains valid. However, when the standard deviation of the distribution of the frequencies of the two photons is in the order of the width of the filters, the frequency distributions are changed by the filter. As the frequency distributions of the two photons are modified, the distribution of frequency difference is modified as well. Therefore, the assumption that the frequency difference is Gaussian distributed might not be valid in this limit. If the frequency distributions of each of the two photons are Lorentzian with a FWHM of 50 MHz each (due to the filter), then the distribution of the frequency difference will be Lorentzian as well, with a FWHM of 100 MHz [30]. The TPQI model can be improved to include the effect of frequency distribution modification due to the fiber Bragg gratings.

For a measurement lasting 24 h, using a window length of 25 ns and setting $\sigma_D = 0.1$ ns, the expected number of coincidence counts in the three detection time difference bins is depicted in Fig. 5.16b, when the standard deviation of the frequency difference of the two photons is set to 42.4 MHz. This value of σ_Δ this corresponds to a FWHM of 100 MHz of a normal distribution. This yields the raw interference visibility of $V = 0.79 \pm 0.06$. This would give a maximum Barrett and Kok entanglement fidelity according to Eq. (5.9) of $F = 0.89 \pm 0.03$.

The dark- and noise counts in a 2-node TPQI experiment with photons converted to the telecom wavelength decrease the visibility significantly, in the order of 15 % compared to the same situation with zero dark- or noise counts. Even in the case of $\sigma_\Delta = 0$, which would mean photons indistinguishable in their frequencies, the visibility is only 0.84 ± 0.05. Also, for a 24 h measurement, it is expected that only 101 coincidence counts will be measured in the two distinguishable photons bins (with detection time differences of $\pm 1T$), yielding a distinguishable photon coincidence rate of 1.2 mHz. To both slightly increase this rate, and to reduce the error bar on the visibility, one can also apply a repeated pulse train of more than 2 excitations on both NV centers.

Chapter 6

Conclusions and Outlook

6.1 Conclusions

For the entanglement generation between two NV centers mediated by interference and detection of single photons, it is required that the photons are indistinguishable in all of their properties, being polarization, frequency and location in space-time. The degree of indistinguishability can be measured by a Two-Photon Quantum Interference (TPQI) experiment.

When two indistinguishable photons impinge on a 50/50 beamsplitter in distinct input ports, the remarkable quantum effect of TPQI predicts that the photons will always exit together in one of the two output ports. Therefore, coincidence counts - a detection of a photon in both output ports - will vanish at 0 delay between the two photons. In this research, two photons from consecutive photon emission of a single NV center have been repeatedly impinged on a beamsplitter. From the measured coincidence counts as a function of the detection time difference, the raw interference visibility has been determined, resulting in $V = 0.91 \pm 0.02$. To extract the photon indistinguishability J, a method to correct for system imperfections has been developed, such as beamsplitter imbalances, photon losses and dark- or noise counts. Together with a Monte-Carlo method of error propagation, this resulted in the value $J = 0.945$ in the 1σ-confidence interval of [0.920, 0.966], demonstrating near-perfect indistinguishability of zero-phonon line photons emitted by a single NV center.

In addition, a TPQI model was developed by calculating the coincidence probability as a function of the detection time difference after the beamsplitter. The model includes several system imperfections, such as beamsplitter imbalance, photon losses and dark- or noise counts. The photons, modelled as exponentially decaying wavepackets, can be made distinguishable in two of their three properties, being frequency and arrival time at the beamsplitter. To be able to compare the model with experimental data, the notion of finite detection time windows of the two detectors was included. The comparison showed that the ratio of coincidence events in the distinguishable detection time difference bins is predicted correctly. However, for agreement with the measurement data, the predicted coincidence events needs to be scaled with a factor of 1.14 per detector. The origin of why this scaling factor is required is not known. Nevertheless, the scaling factor is not as relevant as the ratio itself, as the visibility is calculated with only the ratio of coincidence counts. Moreover, more coincidence counts in the 0 delay bin were measured than predicted by the model with system imperfections, using photons indistinguishable in frequency and arrival time. A possible explanation for this discrepancy is that the emission of the single NV center has a non-zero line width (FWHM of at least 13 MHz), resulting in a potential slight frequency difference between two consecutively emitted photons. Another explanation is that the delay of the interferometer was calibrated with a small error, resulting in a possible arrival time difference smaller than of 0.416 ns. The third explanation is that polarisation effects might have played a role. In the measurement, the final photon indistinguishability is corrected for these possible polarisation effects by using the classical fringe contrast. In this model, the direct effect on the raw coincidence events as a result of polarisation mismatch of the photons cannot be investigated.

Furthermore, the TQPI model was used for predictions of a future two-node TPQI experiment with down-converted photons. Assuming a 2-pulse sequence and a measurement duration of 24 h, the dark- and noise-count limited visibility is predicted to be 0.79 ± 0.06 with a distinguishable photon coincidence rate of 1.2 mHz, allowing for measuring a double-click entanglement fidelity of 0.89 ± 0.03.

6.2 Outlook

The TPQI model can be further improved by also including possible polarisation mismatches of the photons. This can be done by assuming the photons are linearly polarised with a non-zero angle between their polarisation directions, as was done for Gaussian shaped photon wave-packets in [25]. Furthermore, the effect of inhomogeneous broadening of the emission line widths was included in the model by assuming a Gaussian distribution of the frequency difference of the photons. In a single NV TPQI experiment, this distribution might not be Gaussian. It is advised to redo the calculations with a Lorentzian spectral profile. For a two NV TPQI experiment without down-conversion, the assumption of a Gaussian frequency difference distribution is valid. Yet, in an experiment with down-converted photons their respective frequency distributions are influenced by the Lorentzian shaped filter which is necessary to filter out noise photons. The difference of two Lorentzian distributions is again Lorentzian, which is why it is also advised for this situation to redo the calculations assuming a Lorentzian distribution of the frequency difference.

The application of the TPQI model on a two NV experiment showed that the most important source of visibility reduction with the state of the set-ups right now are the dark- and noise counts in the detectors. Also, for a double excitation scheme on the two NV centers, the error bar on the visibility of a 24 h measurement is 6 %. It is advised to perform a measurement with a pulse train of more than two excitations to both reduce this error bar, and slightly increase the distinguishable photon coincidence rate.

This research has proven near-perfect indistinguishability of photons emitted by a single NV center, which in turn predicts a high indistinguishability of photons emitted by two NV centers. At the time of writing, the two nodes are up and running again, allowing for a TPQI experiment with two NV centers with down-converted photons. The next step is local entanglement generation using the double-click scheme with down-converted photons in the lab. If this succeeds, it is time to move one of the nodes to Den Haag to demonstrate heralded entanglement generation between two network nodes separated by metropolitan distances, creating the world's first elementary link of a quantum network.

Appendix A

Appendix Theory

A.1 Joint Detection Probability

The full derivation of Eq. (3.9) is given as

$$\begin{aligned}
P_{\text{joint}}(t_1,t_2) &= \langle 1_S 1_L|\,\hat{E}_1^-(t_1)\hat{E}_2^-(t_2)\hat{E}_2^+(t_2)\hat{E}_1^+(t_1)\,|1_S 1_L\rangle \\
&= \langle 1_S 1_L|\,(\sqrt{R}\hat{E}_S^-(t_1)+\sqrt{T}\hat{E}_L^-(t_1))(\sqrt{T}\hat{E}_S^-(t_2)-\sqrt{R}\hat{E}_L^-(t_2))\cdot \\
&\quad (\sqrt{T}\hat{E}_S^+(t_2)-\sqrt{R}\hat{E}_L^+(t_2))(\sqrt{R}\hat{E}_S^+(t_1)+\sqrt{T}\hat{E}_L^+(t_1))\,|1_S 1_L\rangle \\
&= \langle 0_S 0_L|\left(-R\zeta_S^*(t_1)\zeta_L^*(t_2)+T\zeta_L^*(t_1)\zeta_S^*(t_2)\right)\left(-R\zeta_S(t_1)\zeta_L(t_2)+T\zeta_L(t_1)\zeta_S(t_2)\right)|0_S 0_L\rangle \\
&= |T\zeta_S(t_2)\zeta_L(t_1)-R\zeta_L(t_2)\zeta_S(t_1)|^2,
\end{aligned} \tag{A.1}$$

where we used Eq. (3.8) and Eq. (3.5). Using the expressions for the photon wave functions as in Eq. (3.10), we obtain the following expression for the joint detection probability:

$$\begin{aligned}
P_{\text{joint}}(t_1,t_2,dt_S,dt_L) &= |T\zeta_S(t_2)\zeta_L(t_1)-R\zeta_L(t_2)\zeta_S(t_1)|^2 \\
&= T^2\zeta_S(t_2)\zeta_L(t_1)\zeta_S^*(t_2)\zeta_L^*(t_1)+R^2\zeta_L(t_2)\zeta_S(t_1)\zeta_L^*(t_2)\zeta_S^*(t_1)- \\
&\quad TR\zeta_S(t_2)\zeta_L(t_1)\zeta_L^*(t_2)\zeta_S^*(t_1)-TR\zeta_S^*(t_2)\zeta_L^*(t_1)\zeta_L(t_2)\zeta_S(t_1) \\
&= \frac{1}{{\tau_l}^2}\exp\left[\frac{-t_1-t_2}{\tau_l}\right]\exp\left[\frac{dt_S+dt_L}{\tau_l}\right]\cdot \\
&\quad \big(R^2\cdot(f_R(t_1,t_2,dt_S,dt_L))^2+T^2\cdot(f_T(t_1,t_2,dt_S,dt_L))^2 \\
&\quad -TR\exp[i\Delta(t_2-t_1)]\cdot f_{RT}(t_1,t_2,dt_S,dt_L)-TR\exp[-i\Delta(t_2-t_1)]\cdot f_{RT}(t_1,t_2,dt_S,dt_L)\big) \\
&= \frac{1}{{\tau_l}^2}\exp\left[\frac{-t_1-t_2}{\tau_l}\right]\exp\left[\frac{dt_S+dt_L}{\tau_l}\right]\cdot \\
&\quad \big(R^2\cdot f_R(t_1,t_2,dt_S,dt_L)+T^2\cdot f_T(t_1,t_2,dt_S,dt_L)-2RT\cos\Delta(t_2-t_1)\cdot f_{RT}(t_1,t_2,dt_S,dt_L)\big)
\end{aligned} \tag{A.2}$$

with the terms

$$\begin{aligned}
f_R(t_1,t_2,dt_S,dt_L) &= \mathrm{H}(t_1-dt_S)\mathrm{H}(t_2-dt_L), \\
f_T(t_1,t_2,dt_S,dt_L) &= \mathrm{H}(t_1-dt_L)\mathrm{H}(t_2-dt_S) \text{ and} \\
f_{RT}(t_1,t_2,dt_S,dt_L) &= f_R(t_1,t_2,dt_S,dt_L)f_T(t_1,t_2,dt_S,dt_L),
\end{aligned} \tag{A.3}$$

where we used that $\mathrm{H}^2(t)=\mathrm{H}(t)$. When $dt_S=dt_L=dt$, this simplifies to Eq. (3.13) as presented in the main text.

A.2 No Constraint on Photon Detection Times

If we do not put a constraint on the detection times t_1 and t_2, the coincidence probability can be derived analytically. To this end, we change variables and define t as the time of detection in detector 1, and τ

as the detection time difference between detector 1 and 2, i.e. $\tau = t_2 - t_1$. Following a similar approach as before, the joint detection probability is given as

$$\begin{aligned} P_{\text{joint}}(t,\tau) &= \langle 1_S 1_L | \hat{E}_1^-(t)\hat{E}_2^-(t+\tau)\hat{E}_2^+(t+\tau)\hat{E}_1^+(t) | 1_S 1_L \rangle \\ &= |T\zeta_S(t+\tau)\zeta_L(t) - R\zeta_L(t+\tau)\zeta_S(t)|^2, \end{aligned} \tag{A.4}$$

where we used Eq. (3.8) and Eq. (3.5).
We simplify the notion of arrival times by only considering the arrival time difference $\delta = dt_S - dt_L$. Therefore, we redefine the photons wave functions as presented in the main text (Eq. (3.10)) to the following:

$$\begin{aligned} \zeta_S(t) &= \frac{1}{\sqrt{\tau_l}} \exp\left[-i(\omega - \Delta/2)t\right] \cdot \exp\left[-\frac{t-\delta/2}{2\tau_l}\right] \cdot \mathrm{H}(t-\delta/2) \\ \zeta_L(t) &= \frac{1}{\sqrt{\tau_l}} \exp\left[-i(\omega + \Delta/2)t\right] \cdot \exp\left[-\frac{t+\delta/2}{2\tau_l}\right] \cdot \mathrm{H}(t+\delta/2). \end{aligned} \tag{A.5}$$

This means that if $\delta > 0$, photon L will arrive earlier at the beamsplitter than photon S. Using the expressions for the photon wave functions as in Eq. (A.5), we obtain the following expression for the joint detection probability:

$$\begin{aligned} P_{\text{joint}}(t,\tau,\delta) &= |T\zeta_S(t+\tau)\zeta_L(t) - R\zeta_L(t+\tau)\zeta_S(t)|^2 \\ &= \frac{\exp\left[\frac{-2t-\tau}{\tau_l}\right]}{{\tau_l}^2} \left\{T^2 (f_T(t,\tau,\delta))^2 + R^2 (f_R(t,\tau,\delta))^2 - \right. \\ &\quad \left. TR\exp[i\Delta\tau] f_{RT}(t,\tau,\delta) - TR\exp[-i\Delta\tau] f_{RT}(t,\tau,\delta)\right\} \\ &= \frac{1}{{\tau_l}^2} \exp\left[\frac{-2t-\tau}{\tau_l}\right] \left(R^2 \cdot f_R(t,\tau,\delta) + T^2 \cdot f_T(t,\tau,\delta) - 2RT\cos\Delta\tau \cdot f_{RT}(t,\tau,\delta)\right) \end{aligned} \tag{A.6}$$

with the terms

$$\begin{aligned} f_R(t,\tau,\delta) &= \mathrm{H}(t-\delta/2)\mathrm{H}(t+\tau+\delta/2), \\ f_T(t,\tau,\delta) &= \mathrm{H}(t+\delta/2)\mathrm{H}(t+\tau-dt/2) \text{ and} \\ f_{RT}(t,\tau,\delta) &= f_R(t,\tau,\delta) f_T(t,\tau,\delta), \end{aligned} \tag{A.7}$$

where we used that $\mathrm{H}^2(t) = \mathrm{H}(t)$.
Again using Eq. (3.14) we can include inhomogeneous broadening of the frequency difference Δ. The inhomogeneously broadened joint detection probability $P_{\text{inh}}(t,\tau,\delta,\mu_\Delta,\sigma_\Delta)$ is then given as the integral over all possible values of Δ of the product of $f(\Delta)$ and $P_{\text{joint}}(t,\tau,\delta)$:

$$\begin{aligned} P_{\text{inh}}(t,\tau,\delta,\mu_\Delta,\sigma_\Delta) &= \int_{-\infty}^{\infty} f(\Delta) P_{\text{joint}}(t,\tau,\delta)\mathrm{d}\Delta \\ &= \frac{1}{{\tau_l}^2} \exp\left[\frac{-2t-\tau}{\tau_l}\right] \left(R^2 f_R(t,\tau,\delta) + T^2 f_T(t,\tau,\delta) - \right. \\ &\quad \left. 2RT f_{RT}(t,\tau,\delta) \int_{-\infty}^{\infty} \cos\Delta\tau f(\Delta)\mathrm{d}\Delta\right) \\ &= \frac{\exp\left[\frac{-2t-\tau}{\tau_l}\right]}{{\tau_l}^2} \left(R^2 f_R(t,\tau,\delta) + T^2 f_T(t,\tau,\delta) - 2RT f_{RT}(t,\tau,\delta) \cdot \exp\left[\frac{-\sigma_\Delta^2 \tau^2}{2}\right] \cdot \cos\mu\tau\right). \end{aligned} \tag{A.8}$$

Integrating this over all possible detection times t we get the probability of detecting two photons in the output ports 1 and 2 as a function of the detection time difference τ and the mean and standard deviation of the distribution of the frequency difference $(\mu_\Delta, \sigma_\Delta)$, $P_{\text{coinc}}(\tau,\mu_\Delta,\sigma_\Delta,\delta)$, given as

$$
\begin{aligned}
P(\tau,\mu_\Delta,\sigma_\Delta,\delta) &= \int_{-\infty}^{\infty} P_{\text{inh}}(t,\tau,\sigma_\Delta,\delta)\,\mathrm{d}t \\
&= \frac{1}{2\tau_l}\left\{R^2\cdot\left(\mathrm{H}(\tau+\delta)\exp\left[\frac{-\delta-\tau}{\tau_l}\right]+\mathrm{H}(-\tau-\delta)\exp\left[\frac{\tau+\delta}{\tau_l}\right]\right)+\right. \\
&\qquad T^2\cdot\left(\mathrm{H}(\tau-\delta)\exp\left[\frac{\delta-\tau}{\tau_l}\right]+\mathrm{H}(-\tau+\delta)\exp\left[\frac{\tau-\delta}{\tau_l}\right]\right)- \\
&\qquad \left. 2RT\cdot\exp\left[-\frac{|\tau|}{\tau_l}-\frac{|\delta|}{\tau_l}-\frac{\sigma_\Delta^2\tau^2}{2}\right]\cdot\cos\mu\tau\right\} \\
&= \frac{1}{2\tau_l}\left(R^2\exp\left[\frac{-|\tau+\delta|}{\tau_l}\right]+T^2\exp\left[\frac{-|\tau-\delta|}{\tau_l}\right]\right. \\
&\qquad \left.-2RT\cdot\exp\left[-\frac{|\tau|}{\tau_l}-\frac{|\delta|}{\tau_l}-\frac{\sigma_\Delta^2\tau^2}{2}\right]\cdot\cos\mu\tau\right).
\end{aligned}
\tag{A.9}
$$

where we used that

$$
\begin{aligned}
\int_{-\infty}^{\infty} f_R(t,\tau,\delta)\exp\left[\frac{-2t}{\tau_l}\right]\mathrm{d}t &= \frac{\tau_l}{2}\left(\mathrm{H}(\tau+\delta)\exp\left[\frac{-\delta}{\tau_l}\right]+\mathrm{H}(-\tau-\delta)\exp\left[\frac{2\tau+\delta}{\tau_l}\right]\right), \\
\int_{-\infty}^{\infty} f_T(t,\tau,\delta)\exp\left[\frac{-2t}{\tau_l}\right]\mathrm{d}t &= \frac{\tau_l}{2}\left(\mathrm{H}(\tau-\delta)\exp\left[\frac{\delta}{\tau_l}\right]+\mathrm{H}(-\tau+\delta)\exp\left[\frac{2\tau-\delta}{\tau_l}\right]\right), \quad \text{and} \\
\int_{-\infty}^{\infty} f_{RT}(t,\tau,\delta)\exp\left[\frac{-2t-\tau}{\tau_l}\right]\mathrm{d}t &= \frac{\tau_l}{2}\exp\left[-\frac{|\tau|}{\tau_l}-\frac{|\delta|}{\tau_l}\right].
\end{aligned}
\tag{A.10}
$$

Appendix B

Appendix Results

B.1 Selecting Signal Windows

In the following figure, the scaled data from the optical pi pulse calibration with background is overlaid with the early peak of the number of counts measured in the TPQI experiment. For agreement of peak heights, the data from the optical pi pulse was scaled by a factor of over 10000.

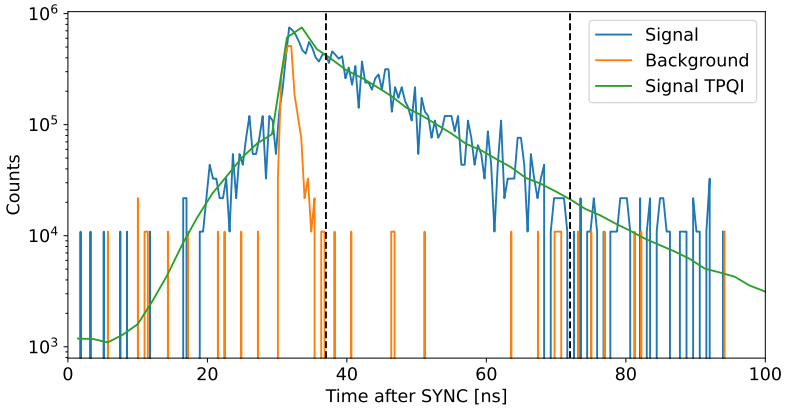

Figure B.1: Scaled optical pi pulse with reflected pulse light (reflections were measured by deliberate detuning the frequency of the RO laser), overlaid with the earliest peak in counts measured in the TPQI experiment. As the measurement time of this optical pi pulse calibration was much shorter, a scaling factor of more than 10000 is required for agreement of the peak heights. The selected time window is indicated with the black vertical lines.

At a window start of 37 ns after the SYNC, the contribution of reflected pulse light is minimal, with an SNR above 50.

B.2 Coincidence Events due to Dark Counts

The expected number of coincidence contributions due to one dark count and one NV photon in each detection time difference bin is calculated using Eq. (3.25), and presented in Table B.1.

	-2T	**-1T**	**0T**	**1T**	**2T**
$P^{dc,ph}$	1.46 ± 0.12	4.5 ± 0.4	3.03 ± 0.25	4.6 ± 0.4	1.56 ± 0.13
$P^{ph,ph}$	75 ± 9	163 ± 13	13 ± 4	183 ± 14	87 ± 9

Table B.1: The first row gives the expectation value of photon- dark count coincidence events in each of the 5 detection time difference bins, with error bar representing one standard deviation. The second row gives the expectation value of photon-photon coincidence events in each of the five bins calculated as $C_j - P_j^{dc,ph}$.

B.3 Coincidence Counts in Time-Bins

The measured number of coincidence counts as a function of the detection time difference τ in ns is shown in the following figure. There is too little data around $\tau = 0$ to be able to extract information of the frequency distribution of the photons from the shape of the curve. The two-sided exponential decay as predicted in the Chapter 2 is visible in the distinguishable photon coincidence peaks.

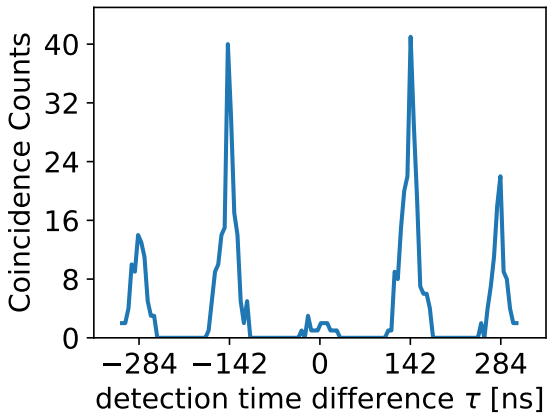

Figure B.2: A histogram of the measured number of coincidence counts as a function of the detection time difference τ in ns using a binsize of 5 ns. The photon counting argument explains why the outermost peaks have maximum which is $\sim 1/2$ of the maximum of the two peaks around $\pm$ 142 ns.

B.4 TPQI Model Verification

In the following figure, the obtained probabilities of coincidence events are plotted per detection time difference bin, in the case of a perfect system with fully distinguishable photons and in the limit of large window lengths. The deviation from the expected probabilities in each bin is less than 0.25 %, confirming that the model works. The small deviation is attributed to finite precision due to numerical integration.

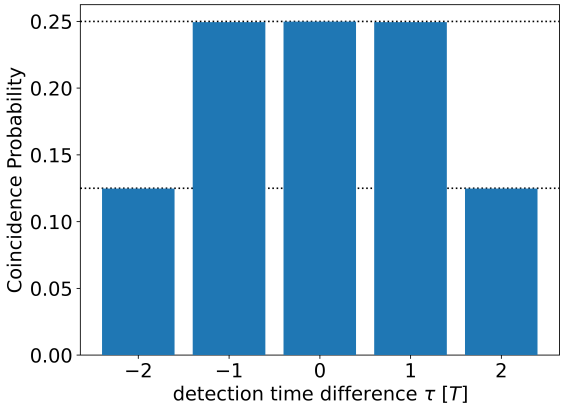

Figure B.3: Verification of the TPQI model with distinguishable photons. The dotted lines represent the expected probabilities of 1/8 and 1/4. The model (the bars in blue) recovers these values with a deviation less than 0.25 %.

B.5 Two NV TPQI Model

The photon counting argument for a repeated sequence of two excitations of two NV centers, A and B, is given in the following table.

-1*T*	**0*T***	**1*T***
1A - 2A	1A - 1B	1A - 2A
1A - 2B	2A - 2B	1A - 2B
1B - 2A	1A - 1B	1B - 2A
1B - 2B	2A - 2B	1B - 2B

Table B.2: All photon configurations that contribute to a coincidence count in one of the detection time difference bins $0T$ and $\pm 1T$. The colours emphasize which detector clicked first, green means detector 1 clicked first, red means detector 2 clicked first. Note that in the $0T$ detection time difference bin, the distinction is also made between the detection times in both detectors.

Bibliography

[1] D. J. Griffiths. *Introduction to Quantum Mechanics*. 2nd. Cambridge University Press, 2017.

[2] Stephanie Wehner, David Elkouss, and Ronald Hanson. "Quantum internet: A vision for the road ahead". In: *Science* 362.6412 (2018).

[3] Bas Hensen et al. "Loophole-free Bell inequality violation using electron spins separated by 1.3 kilometres". In: *Nature* 526.7575 (2015), pp. 682–686.

[4] Norbert Kalb. *Diamond-based quantum networks with multi-qubit nodes*. PhD thesis, Delft University of Technology. 2018.

[5] Anaïs Dréau et al. "Quantum frequency conversion of single photons from a nitrogen-vacancy center in diamond to telecommunication wavelengths". In: *Physical Review Applied* 9.6 (2018).

[6] Katsuya Nagayama et al. "Ultra-low-loss (0.1484 dB/km) pure silica core fibre and extension of transmission distance". In: *Electronics Letters* 38.20 (2002), pp. 1168–1169.

[7] Steven H Simon. *The Oxford Solid State Basics*. OUP Oxford, 2013.

[8] Linh My Pham et al. "Enhanced metrology using preferential orientation of nitrogen-vacancy centers in diamond". In: *Physical Review B* 86.12 (2012).

[9] Elke Neu et al. "Photonic nano-structures on (111)-oriented diamond". In: *Applied Physics Letters* 104.15 (2014), p. 153108.

[10] Stein Faes. "Preparing quantum interference of two to telecom wavelength converted single photons emitted by NV centres". MA thesis. Delft University of Technology, July 2020.

[11] Hannes Bernien. *Control, measurement and entanglement of remote quantum spin registers in diamond*. PhD thesis, Delft University of Technology. 2014.

[12] Marianne Teng. "Towards entanglement generation between nitrogen vacancy centres in diamond over metropolitan distances through telecom fibres". MA thesis. Delft University of Technology, June 2019.

[13] Bas Hensen. *Quantum nonlocality with spins in diamond*. PhD thesis, Delft University of Technology. 2016.

[14] Hannes Bernien et al. "Two-photon quantum interference from separate nitrogen vacancy centers in diamond". In: *Physical Review Letters* 108.4 (2012).

[15] Michael Gould et al. "Efficient Extraction of Zero-Phonon-Line Photons from Single Nitrogen-Vacancy Centers in an Integrated GaP-on-Diamond Platform". In: *Physical Review Applied* 6.1 (July 2016).

[16] Peter C Humphreys et al. "Deterministic delivery of remote entanglement on a quantum network". In: *Nature* 558.7709 (2018), pp. 268–273.

[17] Anna Tchebotareva et al. "Entanglement between a diamond spin qubit and a photonic time-bin qubit at telecom wavelength". In: *Physical review letters* 123.6 (2019).

[18] Christopher Gerry, Peter Knight, and Peter L Knight. *Introductory Quantum Optics*. Cambridge university press, 2005.

[19] Hannes Bernien et al. "Heralded entanglement between solid-state qubits separated by 3 meters". In: *APS* (2013).

[20] Sean D. Barrett and Pieter Kok. “Efficient high-fidelity quantum computation using matter qubits and linear optics”. In: *Physical Review A* 71.6 (June 2005).

[21] Chong-Ki Hong, Zhe-Yu Ou, and Leonard Mandel. “Measurement of subpicosecond time intervals between two photons by interference”. In: *Physical review letters* 59.18 (1987).

[22] Charles Santori et al. “Indistinguishable photons from a single-photon device”. In: *Nature* 419.6907 (2002), pp. 594–597.

[23] Thomas Legero et al. “Time-resolved two-photon quantum interference”. In: *Applied Physics B* 77.8 (2003), pp. 797–802.

[24] Benjamin Kambs and Christoph Becher. “Limitations on the indistinguishability of photons from remote solid state sources”. In: *New Journal of Physics* 20.11 (2018), p. 115003.

[25] Thomas Legero et al. “Characterization of single photons using two-photon interference”. In: *Advances In Atomic, Molecular, and Optical Physics* 53 (2006), pp. 253–289.

[26] Y Rosenzweig, Y Schlussel, and R Folman. “Probing the origins of inhomogeneous broadening in nitrogen-vacancy centers with Doppler-free-type spectroscopy”. In: *Physical Review B* 98.1 (2018), p. 014112.

[27] Andrei Tokmakoff. *Time-Dependent Quantum Mechanics and Spectroscopy*. `https://tdqms.uchicago.edu/`. 2014.

[28] Jonas H Weber et al. “Two-photon interference in the telecom C-band after frequency conversion of photons from remote quantum emitters”. In: *Nature nanotechnology* 14.1 (2019), pp. 23–26.

[29] JJIM van Kan, A Segal, and Fredericus Johannes Vermolen. *Numerical methods in scientific computing*. VSSD, 2014.

[30] Frederik Michel Dekking et al. *A Modern Introduction to Probability and Statistics: Understanding why and how*. Springer Science & Business Media, 2005.

[31] M Lesik et al. “Perfect preferential orientation of nitrogen-vacancy defects in a synthetic diamond sample”. In: *Applied Physics Letters* 104.11 (2014), p. 113107.